MONITORING MARINE PLASTIC POLLUTION USING RADAR: FROM SOURCE TO SEA

Morgan David Simpson

Submitted for Doctor of Philosophy

The University of Stirling

Biological and Environmental Sciences

March 2024

Abstract

Marine plastic pollution poses a significant threat to ocean ecosystems worldwide, necessitating effective monitoring and management strategies. The use of remote sensing plays a vital role in providing large-scale, frequently-timed data for monitoring this issue. A multi-modal system has been deemed the most appropriate for tackling the monitoring of marine debris and pollution. Synthetic Aperture Radar (SAR) can provide a wealth of data by taking advantage of the systems ability to acquire in near all-weather conditions, night and daytime. However, research in radar and SARs capability in monitoring marine plastic pollution is lacking.

This thesis aims to provide an insight into these capabilities. This is through a series of experiments and investigations into the responses of SAR / Radar to marine plastic litter.

Chapter two presents a real-world scenario of plastic accumulation within a river environment. The use of SAR imagery is employed to identify plastic accumulations in two separate study locations. A hypothesis of SAR backscattering interactions with plastic debris is presented. A suite of detectors are subsequently implemented to understand how to best utilise the SAR signal for marine debris detection in these test cases, with the best detector used to create heatmaps of debris accumulation within our test sites.

The following chapter provides the results of two rigorous measurement campaigns, where C- and X-band radar data are exploited in a lab experiment. Backscatter and statistical analysis are undertaken across multiple tests involving differing plastic items, concentrations, and wave conditions. From this, interactions between plastic size, shape, and wave conditions are explored. A new interaction for backscatter interactions with plastic debris is also presented.

The final data chapter investigates the potential use of a proxy for plastic pollution. Two measurement campaigns are conducted which utilise plastisphere-based surfactants, and their interactions for wave dampening, to understand if this is detectable in radar data.

For the first time, detailed analysis of backscatter values from differing plastic items and concentrations are presented, as well as the utilisation of real-world test cases. The results obtained in this thesis provide novel insights and additions to recent literature that contributes to our understanding of the capabilities of radar for marine plastic pollution monitoring, as well as new information that can be used in the planning for future missions and studies on the remote sensing of marine plastic pollution.

Table of Contents

List of Figures

List of Tables

List of Abbreviations

- ARC: Active Reflection Compensation
- CLT: Central Limit Theorem
- CFAR: Constant False Alarm Rate
- Co-Pol: Co-Polarisation
- CNN: Convolutional Neural Network
- Cross-Pol: Cross-polarisation
- Dif1: Optimisation of Power Difference
- Diff: Difference
- DinSAR: Differential Interferometric Synthetic Aperture Radar
- DotD: Difference of the Differences
- ESA: European Space Agency
- EVA: Ethylene-vinyl Acetate
- GRD: Ground Range Detected
- H: Horizontal
- HDPE: High-density Polyethylene
- HLT: Hotelling-Lawley Trace
- IW: Interferometric Wide Swath
- LDPE: Low-density Polyethylene
- NDiff: Normalised Difference
- PCB: Polychlorinated Biphenyl
- PE: Polyethylene
- PET: Polyethylene Terephthalate
- Pow1: Optimisation of Power Ratio
- PP: Polypropylene
- PS: Polystyrene
- Quad-Pol: Quad Polarisation
- RAR: Real Aperture Radar
- ROC: Receiver Operating Characteristic
- ROI: Region(s) of Interest
- SAR: Synthetic Aperture Radar
- SFCW: Step Frequency Continuous Waveform

- SLC: Single Look Complex
- SNAP: Sentinel Application Platform
- SVR: Support Vector Regression
- TSM: Total Suspended Matter
- UAV: Unmanned Aerial Vehicle
- V: Vertical
- VNA: Vector Network Analyser

Statement of Original Authorship

I certify that the work contained within this thesis, including text, figures and tables, is my own, except where specifically stated. The thesis has been composed by myself and has not previously been accepted for a degree or professional qualification.

Signature: 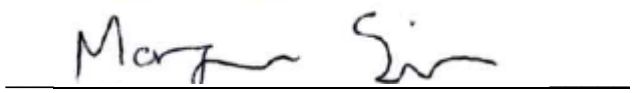

Date: 28/02/2024

Acknowledgements

This work was supported by the Discovery Element on the European Space Agency's Basic Activities (ESA Contract No. 4000132548/20/NL/MH/hm).

Firstly, I would like to thank my PhD supervisor, Armando Marino, for the encouragement all the way from my undergraduate dissertation through to the end of the PhD. Thank you for your patience, support and guidance throughout the past six years. Thank you to my supervisors from ESA, Erio, Peter and Paolo, your guidance has been incredibly valuable and helped enrich the quality of my work. It was a pleasure to be able to meet you all after covid restrictions had ended and to have interesting discussions in person! Many thanks to my co-supervisors: Peter, Vagelis, Andrew and Trevor, not only for the support during the PhD but for supporting me throughout my full studies at Stirling University. I would also like to thank the whole of the EPOS group at Stirling for being such a friendly community to work with and for the wealth of knowledge you all share. Thank you, James and Ronnie, for helping me countless times with experiment setup, planning and organising travel. Thank you to everyone who participated in the Deltares campaigns, it was a pleasure getting to know you all, having interesting discussions, and being able to see you in future conferences!

Thank you to my friends and colleagues who have gone through the PhD with me. The radar lab group: Armando, Vahid, Cristian, Sonny, Pedro, Javier, Felix, Georgina, Wangfei, and Dalin, it's been a pleasure seeing the group grow and always gain new members, I look forward to seeing what opportunities are ahead of us all, and to have more excuses for a pint together in future! Eleri, Emily, Neil, David, Maud, Bridget, Armando, Ian, Andre and the many more who were always happy to have a chat and relax at the pub, thank you for all the fun times. Special thanks to those in my year who made covid lockdown a lot easier, starting a PhD during a pandemic was hard but you all made it that bit easier.

Thank you to my friends outside of university that have been there for me. Nathan, Matthew Gil, Matthew Little, Jess, Matthew Reed, Ewen, Adam, Liam, Neil and Sam, thanks for dealing with all my chat about plastic, experiments and seaweed! My friends in America who've always supported me: The Gilbert family and friends.

I want to thank my family for always being there. My mum, dad and grandparents who have supported me at all times. And finally, Lauren, thank you for supporting me in every way, for bringing love, encouragement, and joy across the whole journey. I couldn’t have done it without you.

Chapter 1: General Introduction

1.1 MOTIVATION - PLASTICS AND MARINE PLASTIC POLLUTION

1.1.1 Plastics and Sources / Pathways

The use of plastic-based materials offers large societal benefits. Plastics offer an alternative lightweight building material for cars, planes and other vehicles (Almroth & Eggert, 2019). Plastics can also perform as an insulator to help reduce energy consumption (Grabowska & Kasperski, 2020), provide food safety through packaging (Mauriello, et al., 2005; Vermeiren, et al., 1999), and emerging 3D-printing processes using plastics are beginning to be applied in socio-cultural, medical and manufacturing sectors (Siraj & Bharti, 2020).

Plastic production has seen a stark increase in the last decades, with an estimated 8300 million metric tons (Mt) of virgin plastics being produced to date (Geyer, et al., 2017). However, with this comes an increase in plastic waste. Research has estimated that in 2015, an estimated 60 – 99 million metric tons of plastic waste was mismanaged (Lebreton & Andrady, 2019) and an approximate 40% of plastic waste is not accounted for in recycling facilities or managed landfills (Worm, et al., 2017).

There are uncertainties throughout scientific literature about the major sources of marine plastic pollution. Schmidt, et al., (2017) used two models to estimate global plastic distribution via rivers. One model indicates that a majority of marine plastic pollution enters the environment through littering, wind dispersal and storm / flooding water runoff. The other model has suggested that riverways are a major source of land-based plastic entering the marine environment. The former model is supported by literature which suggests that the primary pathway for waste entering oceans is through human movement and littering behaviour (Hardesty, et al., 2016; Jambeck, et al., 2018)

The latter model is supported by literature which also states that most plastic enters the ocean from land-based sources, i.e. wastewaters, riverways or wind (Worm, et al., 2017; Miglioranza, et al., 2004). Jambeck et al (2015) provides support to both models by suggesting that riverways are the major source of land to sea plastic pollution, but also suggesting that more than 50% of marine plastics are derived from

mismanaged plastic wastes and that land-based coastal pollution contributed an estimated 4.8 to 12.7 million MT of plastic into the ocean in 2010.

1.1.2 Plastics Influences on Marine Environments and Human Health

Due to the prevalence of plastic in the marine environment, a significant amount of research has been conducted on the effects of plastic pollution on marine and human health. Research has shown that marine debris and pollution affects at least 690 species worldwide (Gall & Thompson, 2015), which includes 43% of all marine mammals, 44% of all seabird species and 86% of all sea turtle species (Laist, 1997). At least 17% of impacted species are also listed on the IUCN Red List as near threatened or above and 92% of all encounters between marine debris and individuals was related to plastics (Gall & Thompson, 2015).

There are two means in which plastic pollution affects wildlife: entanglement and ingestion (Derraik, 2002). Research on the entanglement of marine biota in plastic is extensive, with literature showing that accumulating debris poses a significant threat to fish, marine mammals, crustaceans, turtles and seabirds. These animals can become entangled in loops or openings of floating or submerged plastics (Laist, 1987). Entanglement can cause a multitude of issues for marine biota, including: impairment of ability to catch food, impairment of ability to avoid predators, cuts and abrasions caused by plastic debris, and drowning (Gall & Thompson, 2015; Gregory, 2009; Wilcox, et al., 2015). Schrey & Vauk (1987), state that 13-29% of gannets at Helgoland, German Bight, were killed by entanglement. During their study on Antarctic fur seals, Waluda & Staniland (2013), also estimated that 87% of entangled animals eventually die from complications with entanglement.

Markic, et al., (2020) conducted research on plastic ingestion by marine fish, where it was found that plastic ingestion was detected in 65% of the 494 examined fish species and 67% of the 391 examined commercial fish species. Basto, et al., (2019) found that out of 288 seabirds processed in Portugal, 12.9% had ingested plastics. Plastics have also been found in marine species from various locations across the globe: in the North Sea (Foekama, et al., 2013), Coastal zones (Naidoo, et al., 2015; Neves, et al., 2015), the Atlantic Ocean (Gago, et al., 2020), the Pacific Ocean (Fernandez & Anastasopoulou, 2019) and the Indian Ocean (Cartraud, et al., 2019). Microplastic ingestion has been found to cause health issues within marine species, such as: reductions in energy budgets and growth rates (Watts, et al., 2015) and

reproduction (Rochman, et al., 2014). Ingestion also poses threats through three means: the particles themselves inside the body, the leaching of additives within the plastic, the release of persistent organic pollutants adsorbed to the plastic (Bouwmeester, et al., 2015).

Plastic, specifically microplastic and nanoplastic, pollution can also be exposed and transferred to humans through the consumption of seafood. Rochman, et al., (2015) took samples of seafood from Makassar, Indonesia and California, USA. Anthropogenic debris was found in 21 out of 76 (28%) fish sampled in Indonesia, with plastic as the primary debris. 16 out of the 64 fish sampled in the USA had anthropogenic debris present within the gut content of the fish. Qian, et al., 2024, used hyperspectral simulated Raman scattering (SRS) to detect nanoplastics from bottled water as a model system. Here, they estimated that there are around $2.4 \pm 1.3 \times 10^5$ particles of plastic per litre of bottled water. The implications of nanoplastic and microplastic contact and ingestion with human health are poorly studied (Smith, et al., 2018; Bouwmeester, et al., 2015; Barboza, et al., 2018) however, there is concern surrounding the physical and chemical toxicity to humans. These concerns particularly surround the particles abilities to absorb Persistent Organic Pollutants (POPs) (Bakir, et al., 2014), heavy metals (Brennecke, et al., 2016), and toxic microorganisms (Stenger, et al., 2021).

As seen above, an uncertainty can be found in the literature concerning the quantities of land-based to marine plastic pollution, the distributions of plastic pollution and its full implications on marine and human health. With an uncertainty found in how much plastic is entering the ocean each year, it becomes increasingly difficult to quantify how much plastic is within the marine environment. This uncertainty has caused a growth in research within the past one to two decades for sampling and modelling marine plastics in an attempt to fully quantify the extent of the issue.

1.2 QUANTIFYING THE EXTENT OF PLASTIC POLLUTION

1.2.1 The Problem

Eriksen, et al., (2014), estimated that there is over 270,000 tons of plastic afloat at sea. This study was the first of its kind to compare, and account for, microplastic, mesoplastic and 2 microplastic sizes of floating plastics pollution. The methodology

used within the study was helpful in beginning to the quantification of plastic pollution throughout the marine environment, specifically the ocean. Using net tows and visual surveys, initial readings of plastic pollution were taken by the researchers throughout the study sites. However, there was not enough time or resources to cover vast amounts of water. A model was created in an attempt to estimate global marine plastic pollution but the results were deemed 'highly conservative.' This was determined to be due to the limited inventory of ocean observations available to the researchers. This is shown in other estimates from similar studies, which have global and regional weights of marine plastic varying by two orders of magnitude (Eriksen, et al., 2014; Van Sebille, et al., 2015; Law, et al., 2014; Jambeck, et al., 2015). Eriksen determined that removal processes at play within the sea surface were the cause of the 'minimum estimates' of microplastic. This included processes such as ingestion by organisms (Goldstein, et al., 2013; Jantz, et al., 2013) or biodegradation, beaching and UV degradation (Barnes, et al., 2009).

However, Jambeck, et al., (2015) estimated that in 2010 alone, 4.8 to 12.7 million tons of plastic waste entered the oceans, with a prediction that cumulative quantities of plastic entering the oceans from land would increase by an order of magnitude by 2025. Following this, Borelle, et al., (2020) estimated that 19 – 23 million metric tons entered aquatic ecosystems in 2016 and predict that by 2030, annual emissions of plastic waste may increase to 53 million metric tons per year. Wilcox et al., (2020) also expands on the 'highly conservative' estimates of Eriksen et al (2014) by estimating an increase of 506,000 tons of floating plastic in the ocean in 2010 alone. Eriksen, et al., (2023) further estimated one decade later from their initial study, that there are over 170 trillion plastic particles in the worlds ocean, weighing between 1.1 – 4.9 million tonnes.

This increase in plastic pollution can also be seen in research conducted by Pabortsava & Lampitt, (2020), which estimates that the combined mass of polyethylene, polypropylene and polystyrene of 32 - 651 μm in the top 200m of the Atlantic Ocean is in the range of 11.6 – 21.1. million tons. This estimate can also be deemed conservative of total plastic wastes in the oceans as the range of plastic sizes and polymer types are limited, including potential increases in plastic waste found deeper in the water column or on the seafloor. However, it coincides with the high estimations from Jambeck et al (2015) surrounding plastic wastes entering the ocean.

We can see from the research above that quantifying the total amount of plastic in the ocean is highly variable and there are multiple factors that influence this total. Predictions of total ocean plastic can be improved from a better understanding on plastic waste and its dispersal and from a wider range of techniques in monitoring plastic waste that is already within the ocean. This study and literature review will focus on the range of sampling techniques used in predicting plastic marine debris and the implementation of new and upcoming techniques.

1.2.2 Sampling Techniques

A multitude of techniques for the monitoring and sampling of plastic debris have been developed. Marine trawls (Moore, 2008; Lozano & Mouat, 2009), sediment sampling (Andrady, 2011) marine observational surveys (Ryan, et al., 2009), biological sampling (Goldstein, et al., 2013; Cole, et al., 2013), and beach combing (OSPAR, 2007), while new for plastic, are all well documented sampling techniques.

Sediment sampling collects and assesses material located within the benthic zone of estuaries, the seafloor and beaches for plastic pollution. To assist in the identification of micro and nanoplastics, microscopy techniques can be implemented for further analysis with the sample (Andrady, 2011). Coastal ocean sediments from the Santa Barbara Basin, California, sampled by Brandon, et al., (2019) showed an exponential increase in plastic deposition from 1945 to 2009 with a doubling of 15 years. Juan et al., (2014) found that even on highly protected beaches, plastic pollution levels could reach concentrations greater than 100g of plastic in 1 litre of sediment from three islands in the Canary Current: Lanzarote, La Graciosa and Fuerteventura. Cauwenberghe, et al., (2015) has stated that there is a lack in standardisation in the size definition of ‘microplastics,’ causing comparisons between literature to be difficult to compare. There is also mention of a sampling depths and areas lacking standardisation. While this technique can assess both pollution from micro and macroplastics, the ability to sample deep ocean benthic zone material is extremely costly and difficult. Nevertheless, an advantage of sediment analysis is that lower particle sizes can be detected easier through microscopy and therefore a more accurate estimation can be prepared.

Plastic debris can be classed into multiple sizes: nano-, micro-, meso- and macroplastics. These plastic sizes are commonly found within literature of debris analysis. However, there are some variations in the literature for how these sizes are classified. García-Regalado et al., (2024) classify mesoplastics as debris that falls between 5 – 25mm, and microplastics between 1μm–5mm. Whereas Cozar et al., (2014) state that plastics smaller than 1cm in diameter are referred to as microplastics. Lee et al., (2013) class microplastics as 1-5mm, meso as 5-25mm and macro as >25mm. However, they state that the class of microplastics between 1-5mm are actually 'large microplastics.' A lack of synthesis between the literature can cause confusion within the classifications of these sizes within the field. However, the general classification of sizes from most literature suggests that nanoplastics are <1mm in diameter, micro: 1 – 5mm, meso: 5 – 25mm, and macro: > 25mm.

Throughout the literature, marine trawls have proven to be effective at collecting plastic pollution from mid-water levels within the ocean up to the sea surface. There is some literature that studies marine trawls from benthic zones (Neves, et al., 2015; Selvam, et al., 2021). However, these depths are from shallow benthic zones along coastlines. This can be seen in Neves, et al., (2015) where the average depth ranged from 90 – 349m along the Portuguese Coast, and Selvam, et al., (2021) with an average depth of 6 – 21m along the north-east Arabian Coast. Plastic in marine environments has been shown to settle at different levels inside the water column. This can be seen in Kaladharan et al., (2020) where the depth of trawling grounds influenced the quantity of marine plastic litter that was collected throughout the trawl. Kaladharan et al., (2020) also found that the overall mean of marine plastic litter found in trawls at 10m, 20m, and 40m were significantly different from each other. Not only is the depth of sampling important, but the mesh size on the sampling nets is also crucial as some micro and nanoplastics can pass through the aperture of the mesh, skewing the concentrations of contaminants measured within the marine environment. Gundogdu, et al., (2017) used a 20mm mesh size that was towed for 20 minutes through 4 different locations in Mersin Bay, Turkey, and found a total of 3.88kg of plastic. While this helps quantify amounts of microplastic debris, any micro or nanoplastics will simply slip through the larger aperture net. Similar mesh sizes are also required to be able to make meaningful comparisons among studies and it has been recommended that a 0.33m mesh net is used for net-based surveying of floating or suspended debris in the

ocean (Ryan, et al., 2009). In Moore, (2008), data from a surface trawl of the North Pacific Central Gyre found 27,448 plastic particles within the mesh used. Of which, 9470 particles were near 1mm in size, 4646 near 0.5mm and 2626 near 0.3mm. A study conducted by KIMO Sweden found microplastics at 100,000 times higher concentrations by utilising 80μm than when using 450 μm mesh nets (Lozano & Mouat, 2009). This suggests that even finer mesh apertures could be used to determine the quantity of very fine plastics in the ocean. Overall, literature in this area shows that the results of marine trawls can be extremely variable and possibly unreliable.

There has been quite an extensive amount of research conducted on the biological sampling of marine fauna for plastics. This research analyses marine fauna and the plastic fragments found within their gut contents (Goldstein, et al., 2013; Cole, et al., 2013). Biological sampling of Fulmar (*Fulmarus glacialis*) has been used routinely throughout the literature as an indicator of plastic abundance and is now used in the OSPAR Ecological Quality Objective (EcoQO) for marine litter to assess the extent of plastic pollution (van Franeker, et al., 2011). Though this technique is useful in understanding the effects of plastic pollution on marine animals, it is difficult to quantify total amounts of plastic pollution within the environment from the samples taken within this technique. Biological sampling also relies on marine organisms ingesting the contaminants and small organisms are also incapable of ingesting macroplastics and therefore measurements of larger plastics cannot be quantified.

Marine observational surveys use observers and / or divers on boats to record findings of visible plastic debris. During the survey, records of size, type and location of plastic are recorded. This technique has proven to be most useful when detecting macroplastics over large areas; however, the technique cannot be used to identify nano and microplastics as these are not visible to the naked eye. Debris located during marine observational surveys is also not collected and therefore no further investigations can be undertaken into the type and specific size of plastic within the pollution. This lack of collection can be a hindrance as plastic degrades over time in the ocean and can create smaller particles, further adding to the total number of items within the marine environment. Observational work is also subjective to the observer and can be open to bias (Ryan, et al., 2009).

'Beach combing' involves the process of identifying and collecting debris along a coast front. This method uses the same systematic approach to marine observational

surveys for recording plastic. However, as noted above, micro and nanoplastics are too small to be visible to the naked eye. Terrestrial debris (windswept from inland) can also have an influence on the density of plastic on beach fronts. Therefore, beach combing purely for marine plastic debris does not provide a truly accurate indicator of marine pollution (OSPAR, 2007).

1.2.3 The Issues with Quantifying Plastic Pollution

Due to a lack of standardisation among plastic monitoring techniques there is an uncertainty in the ability to quantify plastic pollution. As well as there being a lack of a technique which can provide global synoptic coverage. All of the literature agrees that there is an abundance of plastic, both macro- and micro-, widespread within the marine environment.

However, there is debate on the concentration trends of plastic pollution within the marine environment over the past decade. In a study of the Northwest Atlantic Ocean, Law et al., (2010) found that over a 22-year study period, there was no trend in plastic concentrations found in the region of highest accumulation, despite a rapid increase in plastic production and disposal during this time period. That is to say, that while plastic production increased over the two decades, there was no increase in plastic concentration found within the region of highest accumulation. Yet, other literature contrasts this, Claessens et al., (2011) found through analysis of sediment cores from Belgian coasts that there are signs that concentration of microplastic debris have risen within the past two decades. This analysis showed that between 1993 – 2008, a tripling of microplastic pollution could be seen. This tripling also coincides with global production rates of plastic. It should be noted however, that concerns can be raised about increased plastic pollution from tourism on beaches where the sediment cores were sampled.

1.3 REMOTE SENSING

All things on Earth reflect, transmit or absorb electromagnetic energy, however, the amount varies depending on material shape and wavelength. The field of remote sensing uses mostly reflected or emitted electromagnetic energy to observe the Earth's land and water features (Campbell & Wynne, 2011). This can be through multiple platforms, be it land, air or spaceborne. For the purpose of this section, the focus will

be on spaceborne radar systems, however, the terms used are transferrable to other remote sensing systems, such as ground radars.

1.3.1 Passive Systems

The most commonly used wavelengths in remote sensing cover microwaves, thermal infrared (TIR), shortwave infrared (SWIR), near infrared (NIR), and visible light (VIS). Systems that use these wavelengths can be split into two distinct groups, passive systems and active systems. Passive systems utilise solar radiation that illuminates the Earth's surface and detect reflection or emissions from those surfaces. These systems typically record microwaves, VIS, NIR, SWIR, and TIR bands. Except for radiometers, passive systems cannot penetrate dense cloud cover, and can only measure during daylight hours, thus limitations are present in locations with dense cloud cover. TIR remote sensing is the exception in being able to be used during nighttime hours.

1.3.2 Active Systems and SAR

Active systems, such as Synthetic Aperture Radar (SAR), provide their own illumination through sending pulses of electromagnetic radiation to the earth surface, allowing it to measure both day and night. Light Detection and Ranging (LiDAR) uses light in the form of a pulsed laser to measure ranges to the Earth. LiDAR can consist of topographic or bathymetric types. Topographic typically uses NIR lasers to map land, while green light lasers are used to penetrate water and measure the seafloor / riverbeds.

SAR systems operate in the microwave region of the electromagnetic spectrum, and due to this, are capable of penetrating cloud cover and are capable of measuring in nearly all-weather conditions (Campbell and Wynne, 2011). There are some key factors to consider when utilising SAR data, including: wavelength / band, imaging modes and swath width, resolution (spatial, temporal, range, azimuth), polarisation, and viewing angle. These factors all influence the energy that is scattered from the ground, of which, the backscattered energy is received by the SAR platform and measured (Richards, 2009).

1.3.3 Wavelength / Bands of SAR

The microwave spectrum can be split into different frequency bands. These bands encompass a frequency range (or wavelength range), which plays a crucial role

in providing each band unique capabilities for remote sensing applications. Typically, the most common SAR bands are L- (1 – 2 GHz / 15 – 30 cm λ), C- (4 – 8 GHz / 3.75 – 7.5 cm λ), and X-band (8 – 12 GHz / 2.5 – 3.75 cm λ). Longer wavelengths have higher penetration capabilities through various mediums, this is related to the dependence of the dielectric constant ε, on the incident wavelength, allowing for greater penetration at L-band than at C- or higher (Meyer, 2019). Due to different wavelengths interacting differently with the Earth's surface, they can be utilised for different applications. Utilising an X-band radar over forestry would typically provide backscatter from the top of the canopy, C-band from within the canopy, and L- and P-band from the forest floor or trunk of the trees. Therefore, one could utilise L-band radar to monitor soil moisture beneath a vegetative canopy, something that an X-band radar would in general not be able to provide.

1.3.4 Imaging Modes and Swath Width

SAR satellites typically have multiple acquisition modes, which can differ in revisit time, spatial resolution, and swath width. Swath width refers to the width of the area covered perpendicular to the flight direction of the SAR as it acquires. Differing imaging modes of a SAR can provide different swath widths. Using the European Space Agency (ESA) satellite Sentinel-1 as an example, there are four acquisition modes available. Stripmap mode acquires data with an 80 km swath at an approximate spatial resolution of 5 x 5 m. Interferometric Wide Swath acquires a 250 km swath at 5 x 20 m spatial resolution. Extra Wide swath mode has a swath of 400 km at 20 x 40 m spatial resolution. Finally, Wave mode acquires vignettes of 20 x 20 km segments at 5 x 5 m spatial resolution.

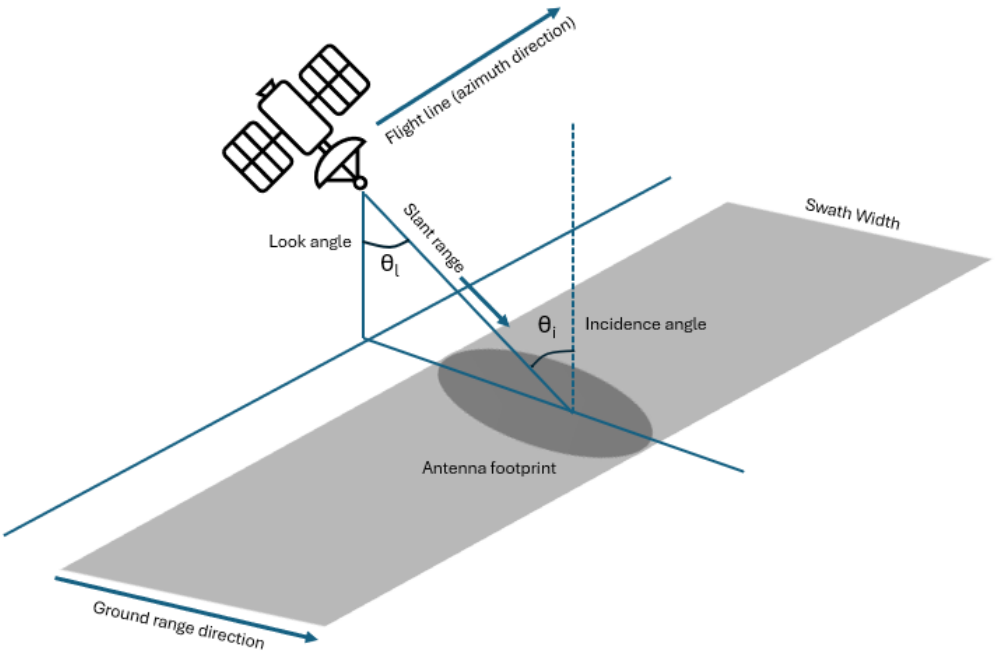

Figure 1.1 SAR System Geometry

1.3.5 Resolution

The image resolution in SAR systems depends on different factors for the range and azimuth directions, and is therefore different in each dimension. Range resolution is determined by the characteristics of the emitted unmodulated pulse. The resolution in the range direction refers to the ability of the radar system to distinguish between two targets that are located on the ground at different distances. In a basic radar system, these targets can only be distinguished if the distance between them is larger than half of the pulse duration of the radar signal. Therefore, a way to achieve fine range resolution in SAR would be to transmit very short pulses. However, short pulses are harder to detect on return due to the low energy that they carry. Providing higher power in a SAR system is expensive and complex, and is therefore not truly feasible. SAR systems are capable of achieving very high range resolutions by utilising a frequency modulation technique called ‘chirp.’ A transmitted chirp sweeps across the frequency of the signal linearly over time through chosen bandwidth (Richards, 2009). A key influence on range resolution is the bandwidth of the transmitted pulse. Once the chirped signal is received back at the antenna, a matched filter is used to remove the modulations on the frequency.

Azimuth resolution is the ability to distinguish between neighbouring objects in the direction of the SAR platform’s motion. Azimuth resolution is dependent on

antenna beamwidth, and synthetic aperture length. The length of the synthetic aperture, or antenna, is dependent on the wavelength, the distance to the ground target, and the real antenna size (Richards et al, 2009). Wider beams produced by smaller antennas mean longer apertures and better azimuth resolution, which directly contrasts with Real Aperture Radars (RAR) where narrow beamwidths are used to obtain good resolutions. However, the differences between RAR and SAR, as well as the full theory behind antenna and aperture synthesis is beyond the scope of this thesis.

1.3.6 Polarisation

Due to SAR systems providing their own illumination, they are able to control, and exploit, the polarisation of their signal in both transmit and receive antennas. Polarisation refers to the orientation of the electric field in the plane perpendicular to the direction of propagation.. When referring to a polarisation channel, the first letter represents the polarisation of the transmitted signal and the second letter represents the polarisation of the received signal. For example, VV means vertically transmitted and received, while VH means vertically transmitted and horizontally received. Polarisation is an important property in SAR imagery, as signals at different polarisations will interact differently with varying objects on the ground. While fully describing polarimetric scattering details is beyond the scope of this thesis, we will mention three types of scatterers which can be abundantly found within natural scenes.

- Surface scatterers – Surface scattering can be either result in specular or diffused reflection. Flat surfaces, such as calm water, smooth soils, urban roads, appear dark in radar imagery as most of the radar pulse is reflected away from the antenna. Rougher surfaces, appear brighter as the pulse can be reflected in all directions, with part of the energy being scattered back to the sensor.
- Volume scattering – Volume scattering primarily occurs within vegetative structures, where the signal comes from scatterers distributed over a vertical direction and it may also bounce multiple times as it propagates through the medium.
- Double Bounce scattering –. This occurs when the signal bounces between two neighbouring surfaces that form an angle between them,

causing the signal to reflect back to the radar examples of double bounce scatterers include buildings and tree trunks. Double bounce scattering can occur from a horizontal surface onto a vertical surface, or vice-versa.

Polarisation is a key implementation with SAR analysis, as different scatterers favour certain polarimetric channels, the relative scattering strength can be found in Table 1.1 Scattering Strength by Polarisation below.

Table 1.1 Scattering Strength by Polarisation

Scattering type	Polarisation channel scattering weight
Rough Surface	VV > HH > HV =VH
Volume	VH = HV
Double Bounce	HH > VV > HV = VH

1.3.7 Incidence and Look Angle

The incidence angle, often denoted by θ, is the angle between the direction of the radar signal propagation and the normal vector to the surface of the Earth at the point of reflection.

Incidence angle plays a crucial role in SAR imaging and can impact the quality and interpretability of the imagery, as well as the scattering characteristics. Considering a surface with diffuse reflection, increasing incidence angles lead to decreasing backscatter intensity. Changes in incidence angle can also have an effect on SAR imagery that cause geometric distortions.

Incidence angle can have effects on SAR imagery that can cause distortion, such as layover, foreshortening, and shadowing. Layover occurs when the top of an objects are imaged ahead of their base, i.e. in imaging the top of a mountain ahead of its base can cause the backscatter from the mountain slope to overlay with other image areas. Foreshortening occurs when these steep slopes are facing the radar and appear compressed in the range direction. Shadowing occurs when the radar signal is obstructed by a tall object, creating an area behind the object that is not illuminated and therefore shadowed.

The look angle is defined as the angle between the vertical direction and the radar beam at the radar platform (van Zyl & Kim, 2010). When surface curvature is neglected, the look angle is equal to the incidence angle at the surface, when the surface is flat. The look angle determines how steeply the radar beam illuminates the terrain, whereas the incidence angle represents the angle at which the radar energy impinges upon the ground surface.

1.3.8 Remote Sensing as a Means of Quantifying Plastic Pollution

The monitoring of plastic pollution has traditionally been field-based, as seen in the techniques listed above. However, this presents two challenges:

• Accessibility issues – Plastic pollution encompasses a global-scale with evidence of plastic pollution found in all marine environments (Van Sebille, et al., 2015). Field-based monitoring of every surface is unfeasible.

• Budget issues – Due to the nature of field sampling, budgeting issues can arise from the high spatial coverage required to monitor the extent of plastic pollution. This can be seen in the literature where multiple models are used to try and predict the extent of the issue worldwide.

Remote sensing has the capabilities to provide long-term, global monitoring of marine plastic pollution. However, the process is still in early stages and research / literature into detecting plastic pollution using imaging data has only grown in popularity in the recent one or two decades. Previous studies on beach litter have used in-situ surveys on a monthly basis to try and detect and quantify plastic pollution (Ryan, et al., 2009; Ribic, et al., 2010). This has pushed for new techniques in remote sensing of coastal and surface water pollutants.

The use of Unmanned Aerial Vehicles (UAVs) has been utilised as a flexible platform for the remote sensing of marine litter. UAVs are able to carry compact digital cameras that can acquire very high-resolution imagery of the environments they fly over. The use of UAVs grants the advantage of a low-cost system that provides both very high-resolution data and a high temporal scale of usage from the ability to revisit multiple times a day (Taddia, et al., 2021; Escobar-Sanchez, et al., 2021).

UAVs have mostly been utilised to monitor coastlines, in particular beach litter. Fallati, et al., (2019) used UAVs to analyse remote shore areas and monitor plastic pollution. It was found that the high-resolution drone images allowed visual detection

of objects on the shoreline. This data was fed into a deep-learning software (PlasticFinder) which reached a sensitivity of 67% and positive predictive value of 94% for identifying plastic debris on the shore. A limitation was found within the process where PlasticFinder struggled to identify plastic debris under certain environmental circumstances, especially under differing sunlight conditions, which lowered the positive predictive value of plastic identification to 54%.

Bao, et al., (2018) used UAV data in the coastal city of Fuzhou, China, to identify and monitor beach litter. An interpretation algorithm was used to extract beach litter data and a confusion matrix was generated to evaluate the classification accuracy. The overall accuracy of the classification was 98.6% in identifying beach pixels and marine litter pixels. The kappa coefficient was 0.819, which can be interpreted as very good following (Landis & Koch, 1977) criteria.

Many other studies have utilised the use of drones for detecting marine plastic pollution, whether it be coastal (Bao, et al., 2018; Fallati, et al., 2019; Goncalves, et al., 2022; Veettil, et al., 2022; Papakonstantinou, et al., 2021) or riverine (Maharjan, et al., 2022; Andriolo, et al., 2023). While the use of drones certainly has the advantages of being a low-cost system, with high temporal and spatial resolution capabilities, and the ability to be used under conditions where optical satellites would be of limited use, there are limitations within the technology. The first is the comparative coverage of UAVs with satellite coverage. While the use of UAVs can provide plentiful coverage for a beachfront, they are limited when it comes to ocean monitoring outside of coastal zones. This is due to the limited battery power of most UAVs and potentially harsher weather conditions stopping the flight of the drone. Safety requirement and legislation also limit the coverage of drone surveying (Cracknell, 2017). UAVs can also not be flown in high wind speeds or heavy rain (Wang, et al., 2019) and have low autonomy (Li, et al., 2022), and therefore they have lower spatial survey coverage when compared with other remote sensing means. A final note for UAV data is that the image processing time can be far greater than satellite processing time, this is due to the larger data size from the higher resolution drone imagery. This increase in processing time has been seen to be ten times greater than that of satellite imagery (Ruwaimana, et al., 2018).

The use of UAV data can however, be used in tandem with satellite data, allowing the user to conduct data comparison, multiscale explanations, model

calibrations and data fusion (Alvarez-Vanhard, et al., 2021). Topouzelis, et al., (2019) used three 100m² targets made of plastic-based materials (PET-1 1.5L water bottles, LDPE plastic bags and nylon fishing ghost nets) in the waters close to Tasmakia beach, Lesvos Island, Greece, to investigate the capabilities of remote detection for plastic. Satellite data and UAV data were used to try and remotely sense the targets. The UAV data was capable of distinguishing the floating targets in a false colour composite. A thermal image from the drone was investigated, where it was found that there were no significant variations between the water surface and the three plastic targets when compared, and that only the plastic bags and plastic bottles could be detected with some degree of uncertainty. The optical satellite data was acquired from Copernicus' Sentinel-2. All three targets were detected in Sentinel-2 true colour composites and greyscale images suggested that the brighter floating targets could be detected from space. However, it should be noted that the blue plastic bags used for one of the targets were indistinguishable in the green and red waveband imagery. Each 100m² target covered 4 adjacent pixels in Sentinel-2 imagery and correlation tests were ran on pixel percentage coverage and spectral reflectance. The results suggested that spectral unmixing algorithms could be implemented in future to begin to detect floating plastics and quantify the amounts seen. Sentinel-1 SAR Single Look Complex (SLC) imagery was also collected of the targets where an analysis of the derived backscatter showed variations between the plastic target and the surrounding water. However, the only target identifiable was the plastic bottle target in VV polarised imagery. It was deemed that further investigations would be needed to look at the effects of different wind speeds and a wider range of floating targets to investigate the effects on backscatter values.

Optical satellite imagery of marine plastic pollution has been a primary focus within the field, with extensive studies conducted on the capabilities of the technique (Topouzelis, et al., 2021; Martinez-Vicente, et al., 2019). Satellite imagery has the advantage of providing large spatial coverage, with spatial and temporal resolution dependent on the sensor used.

Kremezi, et al., (2022) used Sentinel-2, WorldView-2 and WorldView-3 images on the same targets used within Topouzelis et al, 2019. Due to the limited spatial resolution provided within Sentinel-2, a data fusion approach was developed to fuse the lower resolution Sentinel-2 data with the very high-resolution data of WorldView.

Results showed that the plastic targets were visible in the WorldView imagery, but the SWIR region of the Sentinel-2 spectrum were key in order for plastics to be able to be distinguished from other materials. The smallest plastic target observed within the fused imagery was 0.6x0.6m^2. It was also found that the Visible-Near Infrared (VNIR) combination was most efficient for image fusion.

Matthews, et al., (2017) used the optical satellite constellation RapidEye to image marine debris generated by the March 11, 2001 tsunami in Japan. This imagery was of very high resolution, at around 5m, and allowed flotsam to be monitored and tracked. PALSAR Synthetic Aperture Radar images were capable of providing an overview of the Fukushima coastal zone. In these images, well-differentiated debris showed up as a relatively dark feature in the radar signature due to changes in surface roughness. Large dark regions were also demonstrated within the SAR images of surfactant rich regions that were discharged as the tsunami retreated.

Garaba, et al., (2018) also used a short-wave infrared imager to capture red, green and blue (RGB) and SWIR imagery of the Great Pacific Garbage Patch. Using the RGB imagery to identify and record positions, size, colour and type of plastic within the ocean, they then investigated the SWIR spectral information relating to each identified object. Interestingly, the 118 items analysed had a similar magnitude and shape in the SWIR spectra, specifically within ~1215 and ~1732nm. However, spectral variability was seen to be influenced by atmospheric interactions, plastic submersion in water and differences in the optical properties of each object.

Freitas, et al., (2021) used a laboratory setup with two pushbroom hyperspectral cameras to characterise the spectral responses of marine litter samples under direct sunlight. They placed orange polypropylene plastic, blue polypropylene ropes and white polyethylene plastic inside a tank with Atlantic Ocean seawater and monitored the spectral responses. Larger targets (10m x 10m) were then placed into the Atlantic Ocean and were comprised of the same three materials. A manned aircraft carrying a hyperspectral imaging system and an unmanned aerial vehicle (UAV) were then flown over the targets a few moments before or after a pass-over from the Sentinel-2 satellite. The researchers then used the data from the laboratory setup and the manned aircraft to develop and train two machine learning algorithms to detect and classify marine litter samples, these were: Random Forest and Support Vector Machines. This training data was taken from a flight on 18 September 2020 and was used to create models that

would evaluate the data collected on the 20 September 2020 flight. The results were unable to be compared with Sentinel-2 data due to atmospheric conditions during the test campaign. Detection capabilities for the tested machine learning algorithms showed a 70 – 80% precision rate of detection in all three targets, compared to ground-truth pixels, as well as recall rates over 50%.

The use of fluorescence and Raman spectroscopy are considered as potential approaches to observe plastic pollution. Literature shows that the characterisation and discrimination of plastic materials is possible using fluorescence (Htun, 2012). Spizzichino, et al., (2016) used fluorescence intensity ratio threshold values to obtain an automatic recognition of plastics. Lenz, et al., (2015) visually counted and classified 1279 microplastic particles that had been filtered from below the sea surface in the North Atlantic. Raman spectroscopy was then compared to the visual microscopy analysis. This comparison found that particles less than 100μm were identified less using visual microscopy compared to Raman spectroscopy. The conclusion showed that within the Lenz et al (2015) study, 32% of particles and 25% of fibres were misidentified using visual identification. The researchers suggested that Raman spectroscopy can provide mapping of whole sample areas in the future research. However, Raman spectroscopy is challenging for current satellite missions to undertake due to low signal from the process (Maximenko, et al., 2019).

Kikaki, et al., (2020) used high-resolution multispectral satellite data from Planet, Sentinel-2 and Landsat-8 to remotely sense plastic debris in the Bay Islands of Honduras. Approximately 500 satellite images were collected over a 5-year timeframe, June 2014 – September 2019, however, those with > 25% cloud cover were rejected. Only 40 images were processed and analysed for mapping observed plastic debris within the study area. The satellite observations were compared with in-situ expedition data, which were recorded and used as reference data for the multitemporal acquisitions. From this, spectral characteristics of floating plastic litter were recorded, and plastic debris trajectories and sources were also identified. The researchers found that most plastic debris originated from rivers, ending up in the Caribbean Sea, mainly during the prominent rainfall season (August – March).

Kremezi, et al., (2021) pansharpened hyperspectral PRISMA images to attempt to detect marine plastic litter targets off the coast of Tsmakia beach, Greece. Multiple targets were created, they consisted of 3 sizes (selected according to the spatial

resolution of PRISMA and pansharpening techniques): 5.1m x 5.1m, 2.4m x 2.4m and 0.6 x 0.6m, equivalent to full, half and 1/8 of the resolution of PRISMA fused data. The targets were made of High-Density Polyethylene (HDPE), Polyethylene Terephthalate (PET) and Polystyrene (PS). The analysis was conducted on two clear sky PRISMA images collected in September and October 2020.

An algorithm was developed to attempt the detection of these targets in the pansharpened imagery, using this the authors were able to easily detect plastic targets of 5.1m x 5.1m and 2.4m x 2.4m. However, targets of 0.6m x 0.6m could not be detected. The size of the observed pieces is equivalent to the 8%-pixel coverage of the original hyperspectral image.

The authors also found that transparent and green PET polymers were the most difficult to be detected, including at the largest sizes of 5.1 x 5.1m targets. HDPE and PS polymers as well as mixed compositions of all three materials were easily detected. Future work was proposed to try different target sizes to find a threshold value for detection, as well as using the algorithms on separate natural phenomena such as vegetation and foam, to understand if PRISMA can successfully distinguish between anthropogenic and non-anthropogenic materials.

Moshtagi, et al., (2021) explored the spectral reflectance of marine macroplastics in the Very Near Infrared (VNIR) and Shortwave Infrared (SWIR), using virgin and naturally weathered plastics submerged in water. The researchers found that absorption features around 1192 – 1215nm, 1660nm and 1730nm seemed most suitable for polymer discrimination. It was also found that absorption features at 1729nm could help discriminate plastic from wood in the marine environment. The researchers highlighted that the degree of weathering and bio-fouling impacts on spectral reflectance should be investigated further in the future.

Topouzelis, et al., (2021) discussed the capabilities of detecting marine litter through optical remote sensing techniques. They discuss the fundamentals of an optical detection system that uses satellite data to successfully distinguish between non-water pixels and pixels containing floating debris, then successfully discriminating between anthropogenic marine debris and natural phenomena such as algae, wood, white caps, foam, sea snot, etc). The authors found in their review of literature that the processing chain, specifically the pre-processing of satellite images directly done by the sensor, could significantly affect the future accuracy of plastic detection from space, through

atmospheric correction, sunglint, cloud effects and land masking. The authors commented on how improvements of spatial, radiometric, and spectral resolutions would further advance the ability to discriminate between floating marine litter and lookalikes, specifically in the NIR and SWIR and visible range in optical sensors. Improvements in signal-to-noise ratios are also needed as an improvement in sensors as the responses of floating materials can easily resemble noise in low signal-to noise ratio bands and sensors. The authors conclusions presented essential steps in achieving accurate monitoring of floating marine litter through optical satellite data. However, they state that the inclusion of non-optical approaches, such as SAR or LIDAR are most likely needed to overcome the physical and technical obstacles that the remote sensing of marine litter brings.

Hu, (2021) reviewed studies of optical satellite monitoring of plastic pollution. They conclude that the remote detection of marine microplastics from all existing and planned optical sensors appears impossible. This is due to the maximum density of microplastics reported in literature contributing a signal back to the sensor that is at least 60 times lower than the required signal (~0.2% subpixel coverage) and 20 times lower than the sensor noise for a sensor with a signal-to-noise (SNR) of 200. However, they do mention that the detection of macroplastics and other debris is possible when they form large patches, especially along ocean fronts or windrows.

Salgado-Hernanz, et al., (2021) also came to the conclusion that these improvements in optical instruments would also be needed and that there is a need to include marine plastic detection and monitoring into future scientific programs and policies. Their review suggests a multi-modal approach in the detection of marine plastics via different platforms (drones, satellites, aircraft), sensors (passive and active) and multiple other methodologies. They suggest the use of satellites carrying SAR sensors to detect sea-slicks associated to surfactants that could potentially contain high concentrations of plastic. They identify gaps of knowledge in platforms that contain both optical and SAR sensors.

The extent of research into optical techniques has provided a large baseline for their capabilities, specifically with a focus on which bands are best to target for marine litter detection. Limitations within optical satellite remote sensing can come from cloud cover (Prudente, et al., 2020), with global mean cloud cover approximating 66% (Mao, et al., 2019) and an increase in cloud cover being seen (Mao, et al., 2019;

Eastman, et al., 2011; Norris, 1999) over recent decades, this could become a more pertinent issue for optical satellites over the ocean. Another issue with using passive technologies such as optical satellites, is that you require sunlight for imaging. This creates data gaps where you could potentially miss the transport of marine debris over the hours where you are unable to image. There are, however, ways in which these data gaps can be filled, which is via the usage of active technologies such as Radar and LiDAR.

Light Detection and Ranging (LiDAR) can be used to quantify marine debris abundance based on its shape. Ge et al., (2016) used LiDAR as an attempt to monitor and recognise different types of marine debris. The researchers used LiDAR on Nanhui and Beihai beach, China. In a designed experiment on Nanhui beach, 87 objects were set to test detection. The method managed to detect and reconstruct 72 objects, showing an 82.8% accuracy rate. Another three experiments were conducted on Beihai beach to try and detect marine litters that were not placed for the experiment. The mean accuracy of LiDAR during the experiments was 75.4%. LiDAR was capable of detecting plastic, paper, cloth and metal; however, it was incapable of detecting glass debris.

LiDAR has previously been used to detect schools of fish and phytoplankton near the surface of the ocean, as well as marine debris such as logs (Veenstra & Churnside, 2012). The use of LiDAR data can provide depth-resolved information through the water column, which can be used to aid detection of submerged litter in less turbid waters (Martinez-Vicente, et al., 2019), something which optical and especially microwave / radar techniques struggle to, or simply cannot, accomplish.

The key limitation of LiDAR data at the moment is primarily the very high cost of the sensor. Also, while there have been studies undertaken on use of LiDAR for marine debris identification on beaches, the use of LiDAR for detecting floating or submerged plastics is less extensive. Palombi & Raimondi (2022) have began to study the use of LiDAR for detecting plastic submerged in still water in lab conditions. Their results show that the hyperspectral fluorescence of LiDAR is capable of detecting fluorescence features of several types of plastic, while also being able to decouple it from the fluorescence associated with dissolved organic matter. The LiDAR used in this experiment is also the same class of laser that is already deployed from some spaceborne missions, which could provide insights into what is capable for future

missions. While this study shows the potential of LiDAR for marine litter detection, future studies are needed on to extend the database for more plastics, especially those under different weathered conditions or UV degradation, and to understand how LiDAR will perform in real-world sea states rather than in lab conditions.

Other active systems include Global Navigation Satellite System Reflectometry (GNSS-R). Gonga, et al., (2023) conducted an experiment to investigate the feasibility of using GNSS-R for detecting marine litter plastic in a wave tank. Their results showed that detecting plastic litter purely based on the change in reflected power is challenging, however, it may be possible to detect larger accumulations of macro-plastics using a statistical analysis of the GNSS-R estimated reflectivity. Evans & Ruf, (2022) used CYGNSS GNSS-R measurements of ocean surface roughness, in tandem with annual mean microplastic distributions to monitor where changes in surface roughness occurred globally throughout the oceans. They found that the annual mean predictions of microplastic distribution was generally consistent with locations with lower surface roughness, with hypotheses involving dampening from microplastics themselves or from surfactants associated with these materials. A further study used to investigate these dampening effects was then published by Sun, et al., (2023), where it was found that the dampening effects from surfactants on both mechanically- and wind-generated waves are much more significant than the effect of microplastics themselves.

GNSS-R has the potential to monitor plastic pollution similar to that of Synthetic Aperture Radar (SAR). Interestingly, it has been found that the behaviour of the backscattering coefficient of GNSS-R and SAR were found to be strongly correlated (Stilla, et al., 2020). Clarizia, et al., (2009) analysed GNSS-R maps from the UK-DMC satellite to observe the ocean surface. The use of GNSS-R scatterometric applications allows for wind speed and direction to be determined, as well as Significant Wave Height (SWH) and Mean Sea Level (MSL) from altimetric applications. Sea surface roughness can also be determined using GNSS-R scatterometric applications. This involves the use of L-Band GPS signals transmitted from satellites that bounce off the ocean and are subsequently received by the UK-DMC satellite. Contributions to sea surface roughness determination come from the Specular Point (SP) and the Glistening Zone (GZ), of which, the latter widens with increasing surface roughness (Clarizia, et al., 2009; Yan, et al., 2017). The GNSS-R measurements were compared with in-situ

measurements from buoys within the ocean where it was found that the retrieved values were generally consistent with the buoy measurements. Yan, et al., (2017) have also noted that the size of the GZ from GNSS-R systems can cover areas up to hundreds of kilometres, which can cause limitations particularly in the presence of heterogenous surface conditions. In the case of surfactant-rich waters, the surface conditions could be quite homogenous, so a relationship here can possibly be researched.

The use of Synthetic Aperture Radar (SAR) is a promising active technique which has seen increased research in recent years. Savastano, et al., (2021) used a novel Floating Debris Index (FDI) on optical data obtained from Sentinel-2 to overcome lack of consistent ground-truth data from in-situ surveys for the study. Sentinel-2 data was therefore used as possible ground truth sources to localise suspected targets in Sentinel-1 images that were also acquired at similar timings, all images used between Sentinel-1 and Sentinel-2 were acquired within a range of 4 hours of each other.

SLC IW Sentinel-1 images underwent feature extraction, for the features extracted from SAR, the intensity of the signal backscatter and the parameters derived by the Gray Level Co-occurrence Matrix (GLCM) were considered. GLCM is one of the most widely used methods to computer second-order texture measures and it is useful to improve images classification accuracy.

The authors focused on a pixel-based binary classification: supervised binary classifiers are applied to each pixel of the image in order to decide if that pixel contains plastic or not. They used three algorithms: Random Forest, Support Vector Machines and Gaussian Naïve Bayes. The results showed a balanced accuracy (mean of true positive and true negative rates) obtained in the binary classification of 0.68 for Gaussian Naïve Bayes, 0.86 for Random Forest and 0.86 for Support Vector Machines.

The use of Sentinel-2 images as a pseudo-ground truth is useful for when ground-truthing is not available. However, the availability of Sentinel-2 data is weather and daytime dependent and may not always be available. The authors proposed that future work should focus on the use of in-situ validated ground truth data and to investigate a wider range of scenarios and locations as they had only tested one location.

As previously mentioned, Topouzelis et al (2019), used Sentinel-1 and -2 images to try and monitor large floating plastic targets. It was found that their 100m^2 target of plastic bottles was the only visible target within their SAR images. It was deemed that further investigations would be needed to look at the effects of different wind speeds and a wider range of floating targets to investigate the effects on backscatter values.

1.3.9 Microbes on Plastic / Biofouling

Many studies have reported the colonization of plastic debris by bacterial phyla which would normally not be common in those waters. According to Osborn & Stojkovic, (2014), the microbes residing on plastic debris found in Atlantic Ocean are mostly composed of Alphaproteobacteria, Roseobacteria and Gammaproteobacteria groups. The study by Lobelle & Cunliffe, (2011) also found specific groups of bacteria on plastic debris floating in the North Atlantic Ocean which are not normally associated with those waters. A difference in chemical and bacterial composition of the surfactants and surrounding seawater is also observed by Debroas et al., (2017), who found Rhodobacterales, Rhizobiales, Streptomycetales, Cyanobacteria, Alphaproteobacteria, Gammaproteobacteria, Actinobacteria and Betaproteobacteria. The studies by Lyons, et al., (2010) and Keswani, et al., (2016) that analysed plastic fragments in the North Atlantic Garbage Patch found an abundance of bacterial colonies, including *Escherichia coli*. According to Rochman, et al., (2015), the contaminants associated with plastic in marine environment are extremely complex and were termed as a chemical cocktail of contaminants. Finally, Masó, et al., (2003) found that micro-plastic could transport benthic diatoms and small flagellates, including potential harmful dinoflagellates (*Ostreopsis* sp. and *Coolia* sp.), resting cysts of unidentified dinoflagellates and both temporary cysts and vegetative cells of *Alexandrium taylori*.

1.3.10 Surfactants and Synthetic Aperture Radar

Oil spill detection through the use of SAR is one of the most prominently studied fields of the technology (Topouzelis, 2008). Mineral oil itself, is a kind of surfactant. A surfactant is a substance which tends to reduce the surface tension of a liquid in which it is dissolved, with surfactants having been shown to alter the surface tension of the near-surface layer of the ocean (Hühnerfuss, et al., 1981). Surfactants-based slicks are capable of dampening short gravity-capillary waves on the sea surface (Huhnerfuss, et al., 1981; Gade, et al., 2006). Synthetic Aperture Radar (SAR) is

sensitive to surface roughness (Van der Wal, et al., 2005; Mattia, et al., 1997; Shi, et al., 1997). Inland water bodies within SAR images tend to be relatively smooth, with the energy from the radar moving in a specular direction away from the sensor and a slight backscatter returning towards the radar (Mason, et al., 2012). However, water bodies can have increased surface roughness from wind-stress or water currents. This increase in surface roughness provokes a high backscattering, known as Bragg scattering. When wind blows over the sea surface, a distribution of ocean waves are generated. These generated waves can be visualised as small slopes. As the electromagnetic waves hits the periodic ocean waves, these weak individual reflections bounce from the wave surfaces and back to the radar line-of-sight, causing an increase in backscattering.

Surface waves are influenced by the capillarity of the water and differences in these waves will affect Bragg scattering (Phillips, 1988). Since surfactants have been shown to dampen the capillary waves on the sea surface, radar is therefore sensitive to this dampening. This characterisation in radar imaging has been seen in Hühnerfuss et al (1981) with a monomolecular alcohol film in Ku and X bands. It can also be seen in (Latini, et al., 2016) where SAR images of the Deepwater Horizon oil spill were measured in L-, C- and X- bands. It was found that the damping ratio increase with Bragg wavenumber and that the damping ratio also decreases at high wind speed. All measurements of the sea slicks were taken during wind speeds in the range of 4 – 9 ms^{-1}.

Ermakov et al., (2015) simulated oil spills using different surfactants, which included: Oleic Acid (OLE), Dodecyl Alcohol (DA) and Vegetable (Sunflower) Oil (VO) poured onto the water surface of the Gorky Water Reservoir. The geometry of the slick and the evolution of it were then studied using photography and satellite radar images from Envisat ASAR and TerraSAR-X. For each slick created, around 200ml of surfactant was used on the surface of the water. Wind speeds of 2-3m/s were recorded on site during the experiment and the weather conditions are described as ‘calm’ by the authors. The slicks were seen to be visible within the SAR imaging and are stretched by the effects of surface drift currents. The researchers also used a parametric wave method in a laboratory to measure the physical parameters of the surfactant films, including surface tension coefficient and the elasticity.

Open ocean surfactants are primarily biologically derived (Sabbaghzadeh, et al., 2017). These surfactants can be produced from bacteria (Kurata, et al., 2016), phytoplankton and zooplankton grazing (Zutic, et al., 1981; Kujawinski, et al., 2002). Sabbaghzadeh et al (2017) showed that the Atlantic Ocean has a large presence of surfactants produced within the sea surface microlayer. This has also been seen in samples collected from the north east coast of the UK, where Pereira et al., (2016) found surfactant activity highest in the summer within the sea surface microlayer. Pereira, et al (2016) also found that chlorophyll-a indicated spatial and temporal signals in the quantity and composition of the surfactants within the sea surface microlayer and sub-surface water. Wurl, et al., (2011) found surfactants in subtropical, temperate and polar regions of the ocean suggesting that surfactants are capable of being produced on the ocean's surface to a significant extent. The researchers also found that surfactant enrichments persisted in waters up to $10ms^{-1}$ and there were no observed depletions of surfactants in wind speeds above $5ms^{-1}$. They did find, however, that wind speeds exceeding 12ms-1, can prevent extensive sea-surface microlayer formation.

Howe, et al., (2018) studied the relative abundance of Bacillus spp., a surfactant-associated bacterium, within a natural sea slick in the Gulf of Mexico. The researchers collected 100 samples of the surface water and conducted DNA extraction on each to identify any bacterium present in the samples. TerraSAR-X was also used to identify areas of sea slicks within the sample sites, it should be noted that wind speeds were between 2-8m/s on all days of sampling from February 6th – February 12th 2016. The researchers concluded from the study that in sea-slick areas, *Bacillus* spp. could reside in subsurface waters and produce surfactants that moved toward the surface, changing the surface microlayer of the waters. The researchers also wrote that new similar studies are needed in different areas to advance the science surrounding the transport and aggregation of surfactants in low and moderate wind speeds.

Ermakov, et al., (2019) observed surfactants in the Volka-Oga tributary mixing zone, Russia, using MSI Sentinel-2 and SAR Sentinel-1 imaging. A confluence area could be seen within the Sentinel-2 optical imagery, which was clear from the colour differences between the flows of water. The SAR imagery showed a mixing zone between both rivers in the form of a slick on the water surface that dampened the short wind waves.

Davaasuren, et al., (2018) investigated Sentinel-1 and COSMO-SkyMed SAR images of the North Atlantic and North Pacific Oceans, where they observed dark areas, whose shapes were stripey and 'ring-like.' The areas with the dark signatures fall in areas with high concentrations of microplastics over the North Atlantic and North Pacific. They found low wind speeds (0.12 – 4.44 ms^{-1}) in all of their scenes, making them hypothesise that these dark features were related to surfactants and not due to a biogenic chlorophyll-*a* means.

Simpson, et al., (2021) observed surfactants within the Atlantic, Indian and Pacific Ocean gyres. Using Sentinel-1 and TerraSAR-X images, dampening streaks were seen throughout the SAR acquisitions. Using wind speed data, the streaks only appeared in conditions that allow for surfactant viewing (~10ms^{-1} wind speeds). Chlorophyll-a values were also obtained and a biogenic origin from chlorophyll-a / algal blooms was ruled out due to low values observed. Utilising this information, that these dampening streaks could indeed be related to surfactants, with wind speeds showing good viewing conditions, and since there was a lack of algal blooms within viewing locations at the time of surfactants being present, a hypothesis was derived that they could be produced from plastic concentrations and plastisphere-based surfactants within the gyres of the ocean. This dampening from plastisphere-based surfactants has been explored, which will be shown in Chapter 5.

1.4 THESIS AIMS AND CONTRIBUTIONS

As concern over marine plastic pollution continues to increase, a synoptic and holistic solution is needed to monitor and quantify the presence of plastic debris within the ocean. Remote sensing constitutes a key technology that is capable of providing large-scale spatial coverage on a high-resolution temporal scale. Crucially, much of the key literature suggests that a multi-modal approach will be necessary for monitoring marine plastic pollution. However, the science of the remote sensing of marine litter, is still in early phases. SAR systems in particular could acquire vital information in the monitoring of marine debris, but few research has been conducted to fully understand the capabilities of the technology for this application.

Thus, the overall aim of this thesis is to contribute to the current knowledge about the use of radar and SAR systems for the monitoring of marine plastic pollution. This is approached in this thesis by processing large multitemporal and polarimetric SAR

Sentinel-1 Single Look Complex (SLC) datasets, interpreting SAR and ground-radar systems responses from marine plastics, applying the use of change detection for plastic pollution built on state-of-the-art detectors, and finding ways to monitor plastic pollution through the use of surfactants as a proxy.

The primary objective of the thesis is to understand radar and SARs capabilities in monitoring marine debris, specifically macro-debris. This is achieved in chapters 2 and 3, with chapter 2 using real-world test cases of monitoring plastic islands in SAR images and undertaking backscatter analysis with change detection. Chapter 3 utilises lab experiments with a ground radar to understand threshold concentrations capable of detection with a high-resolution radar instrument from the ground.

A second objective is to understand if a proxy could be utilised to monitor plastic pollution. This is achieved in chapter 4, with the inclusion of plastisphere-based surfactant experiment data.

1.5 THESIS OUTLINE

In the following, the content of the chapters is illustrated:

1) The second chapter presents the use of Synthetic Aperture Radar (SAR) for monitoring plastic islands that are accumulated by dams in river environments. Two study locations are considered, with detectors implemented and assessed for their effectiveness in detecting marine debris within these locations.

2) The third chapter examines the use of radar measurements for monitoring and detecting marine plastic debris in free-flowing marine environments. Here, a rigorous measurement campaign is conducted in a lab setting, where a thorough statistical analysis is conducted on ground-radar backscatter results. In particular, plastic items and concentrations that are detectable, and theory of detection are provided.

3) The fourth chapter concerns the use of a proxy to derive marine plastic pollution. Here, the use of ground-radar measurements are utilised to understand the effects of plastisphere-based surfactant dampening.

1.6 PUBLICATIONS

1.6.1 Peer-reviewed publications:

- Simpson, M.D., Akbari, V., Marino, A., Prabhu, G.N., Bhowmik, D. et al. (2022). 'Detecting Water Hyacinth Infestation in Kuttanad, India, Using Dual-Pol Sentinel-1 SAR Imagery,' Remote Sensing, Vol 14 (12), 2845.

- Simpson, M.D., Marino, A., de Maagt, P., Gandini, E., Hunter, P. et al. (2022). 'Monitoring of Plastic Islands in River Environment Using Sentinel-1 SAR Data,' Remote Sensing, Vol 14 (18), 4473.

- Simpson, M.D., Marino, A., de Maagt, P., Gandini, E., de Fockert, A. et al. (2023). 'Investigating the Backscatter of Marine Plastic Litter Using a C- and X-Band Ground Radar, during a Measurement Campaign in Deltares,' Remote Sensing, Vol 15 (6), 1654.

- Lanz, P., Marino, A., Simpson, M.D., Brinkhoff, T., Koster, F., Moller, M. (2023). 'The InflateSAR Campaign: Developing Refugee Vessel Detection Capabilities with Polarimetric SAR,' Remote Sensing, Vol 15 (8), 2008.

1.6.2 Conference Proceedings

Simpson, M.D., Marino, A., Prabhu, G.N., Bhowmik, D., Rupavatharam, S., Datta, A., Kleczkowski, A., Alice, J., Maharaj, S. 2020. *Monitoring Water Hyacinth in Kutannad, India, Using Sentinel-1 SAR Data*. Ahmedabad, Gujarat, India, IEEE InGARSS.

Akbari, V., Simpson, M.D., Maharaj, S., Marino, A., Bhowmik, D., Prabhu, G., N., Datta, A., Kleczkowski, A., Sujeetha, A.R.P. 2021. *Monitoring Aquatic Weeds in Indian Wetlands Using Multitemporal Remote Sensing Data with Machine Learning Techniques.* Brussels, Belgium, IEEE IGARSS.

Simpson, M.D., Marino, A., de Maagt, P., Gandini, E., Hunter, P., Spyrakos, E., Tyler, A., Ackermann, N., Hajnsek, I., Nunziata, F., Telfer, T. 2021. *Monitoring Surfactants Pollution Potentially Related to Plastics in the World Gyres Using Radar Remote Sensing.* Brussels, Belgium, IEEE IGARSS.

Simpson, M.D., Marino, A., de Maagt, P., Gandini, E., Hunter, P., Spyrakos, E., Tyler, A., Telfer, T. 2022. *Monitoring of Large Plastic Accumulations Near Dams Using Sentinel-1 Polarimetric Sar Data.* Kuala Lumpur, Malaysia, IEEE IGARSS.

Simpson, M.D., Marino, A., de Maagt, P., Gandini, E., de Fockert, A., Hunter, P., Spyrakos, E., Tyler, A., Telfer, T. 2023. *Investigating the Backscatter of Marine Plastic Litter Using a C- and X-band Ground Radar.* Florence, Italy, EUCaP.

Kasiti, F., Simpson, M.D., Marino, A. 2023. *Detecting and Mapping of Water Hyacinth in Lake Victoria Using Radar Polarimetric Data.* Pasadena, USA, IEEE IGARSS.

Simpson, M.D., Marino, A., de Maagt, P., Gandini, E., de Fockert, A., Hunter, P., Spyrakos, E., Tyler, A., Telfer, T. 2023. *Backscatter Analysis of Marine Plastic Litter Using A C- and X-Band Ground Radar.* Pasadena, USA, IEEE, IGARSS.

Chapter 2: Monitoring of Plastic Islands in River Environments Using Sentinel-1 SAR Data

This chapter provides a real-world test case of utilising SAR for monitoring marine debris within river environments in the Balkan Countries. To perform the analysis, the freely available dual-polarisation GRD and SLC data provided by the Sentinel-1 SAR satellite were used in tandem with pseudo- ground truth data from news articles within the regions.

Backscatter analysis is undertaken on the study sites and change detectors are implemented. This analysis shows that particularly detectors that can utilise the coherent data from SLC acquisitions perform better when compared with those that only utilise incoherent data from GRD acquisitions, with true positive detection ratings of ~95% with 0.1% false alarm rates seen in the best performing detector. We also found that the cross-pol VH channel provides better detection than those based on single-pol VV polarisation.

This work has been published in Remote Sensing MDPI, in the following: Simpson, M.D., Marino, A., de Maagt, P., Gandini, E., Hunter, P. et al. (2022). 'Monitoring of Plastic Islands in River Environment Using Sentinel-1 SAR Data,' Remote Sensing, Vol 14 (18), 4473.

2.1 INTRODUCTION

Marine plastic pollution is of major concern due to its persistence in the marine environment and its impacts on human and marine health. The presence of plastic in marine environments has been shown to negatively affect at least 690 species worldwide (Gall & Thompson, 2015), and this can be through entanglement and/or ingestion (Derraik, 2002). The implications of the human consumption of marine plastic debris are poorly studied; however, concerns have been raised regarding chemical toxicity and the threats posed by the particles themselves inside the body (Bouwmeester, et al., 2015; Barboza, et al., 2018; Smith, et al., 2018).

A large amount of marine plastic pollution can be derived from land-based sources, such as street litter, poorly controlled waste sites, plastic packaging (industrial or commercial), and illegal dumping (Isensee & Valdes, 2015). (Jambeck, et al., 2015) estimate that of the 275 million metric tons of plastic waste generated in 192 coastal countries, 4.8–12.7 million metric tons entered the ocean in 2010. It was also predicted that cumulative quantities of plastic entering the oceans from land-based sources would increase by an order of magnitude by 2025. Following this, Borelle, et al., 2020 estimated that 19–23 million metric tons of plastic waste entered aquatic ecosystems in 2016 and predicted that by 2030 annual emissions of plastic waste may increase to 53 million metric tons per years.

Plastics in the river environment are of particular interest due to their potential pathways into the ocean. Lebreton, et al., (2017) estimate that between 1.15 and 2.41 million metric tons of plastic waste enters the ocean every year from rivers, with over 74% of emissions occurring between May and October. Previous studies have shown that the observed plastic concentrations within sampled river systems can differ by several orders of magnitude (Dris, et al., 2015). This change in plastic concentration can be influenced by the population density within the catchment (Van der Wal, et al., 2015); the presence of dams, weirs, or other artificial barriers (Mani, et al., 2015); and rainfall rates, where plastic can be moved through surface runoff (Yonkos, et al., 2014). Moore, et al., (2011) studied the Coyote Creek tributary, the Los Angeles River, and the San Gabriel River, where they reported that plastic debris levels varied by up to three orders of magnitude when measured at different time periods. The significant changes in the plastic concentrations were explained by rainfall events throughout the study, where runoff transported plastic into the riverine system.

Plastics in water are traditionally measured using in situ methods, such as marine trawls (Lozano & Mouat, 2009), biological sampling (Cole, et al., 2013), sediment sampling (Andrady, 2011), marine observational surveys (Ryan, et al., 2009), and beach combing (OSPAR, 2007). More recently, research into the use of remote sensing for plastic monitoring has been implemented. This has primarily been focussed on the use of optical data (Biermann, et al., 2020; Topouzelis, et al., 2019), but challenges can arise from cloud cover and resolution issues; thus, other methods to detect plastic debris from remote sensors have started to be explored.

Biermann, et al., (2020) used optical satellite data from Sentinel-2 to classify floating debris material consisting of seaweed, sea foam, and macroplastics. Using a Naïve Bayes algorithm to classify mixed materials, the materials were classified as plastics with an accuracy of 86%. Garcia-Garin, et al., (2021) used 3700 optical images from drones and aircrafts to train a convolutional neural network (CNN) for detecting floating marine litter. The highest model accuracy achieved was 0.81 during the cross-validation, but the authors suggested that the monitoring of marine litter in the open sea still proposes a technological challenge.

Gomez, et al., (2022) found that debris was visible in the River Drina near Visegrad in Sentinel-2 imagery. Using a learning-based approach, the authors found that debris accumulation within the River Drina at Visegrad was highest at the beginning of the year and quickly decreases as the net that intercepts floating garbage within the river is cleared. Their approach could correctly identify floating debris in images that were not from regions used in the training datasets. The authors report that the difficulty of using Sentinel-2 is related to the coarse resolution and its unavailability during cloud cover. This makes analysis after storms and during winter or rainy seasons difficult or impossible.

Synthetic Aperture Radar (SAR) is an active microwave fine-spatial resolution imaging sensor that can monitor in all light conditions and in almost all-weather conditions (Toth & Jozkow, 2016). SAR is sensitive to surface roughness (Van der Wal, et al., 2005; Mattia, et al., 1997), making it particularly valuable in monitoring rivers, oceans, and other surface waters (Van der Wal, et al., 2015; Mattia, et al., 1997; Lyzenga, et al., 2004; Mitidieri, et al., 2016; Vickers, et al., 2019). Inland water bodies within SAR images tend to appear relatively smooth, with the energy from the radar reflecting in a specular direction away from the sensor and a small backscatter returning towards the radar (Ferrentino, et al., 2020). However, water bodies can also have an increased surface roughness created by water currents or wind-stress. This increased surface roughness provokes a higher backscattering, known as Bragg scattering (Phillips, 1988).

Dams are known to trap sediments as well as pollutants, such as plastics, metals, and Polychlorinated Biphenyls (PCBs) (Kondolf, et al., 2014; Watkins, et al., 2019). Optical data and SAR have both been utilised in the monitoring of chlorophyll-*a*, Total Suspended Matter (TSM), landslide monitoring, and water volumes in dam and

reservoir contexts (Molkov, et al., 2019; Reyes-Carmona, et al., 2020). Molkov, et al., 2019 used LiDAR and Sentinel-2 data to develop regional algorithms of chlorophyll-*a* and TSM from the Gorky Reservoir, Russia. The proposed algorithms were capable of being used for the regular environmental monitoring of the Gorky reservoir, and could potentially be adapted for seven other reservoirs in the Volga River system. Reyes-Carmona, et al., (2020) used Differential Interferometric Synthetic Aperture Radar (DInSAR) to study the Rules dam, Spain, where ground instabilities for landslides and water level were monitored. Using DInSAR, the group could evaluate potential hazards related to different landslide typologies and could also observe how water level changes within the reservoir influence landslide behaviour (Reyes-Carmona, et al., 2020). Recently, reports of plastic islands accumulating by dams following heavy rainfall have been reported in Balkan countries (Emric, 2021). This study is focused on the ability to detect and monitor these accumulated plastic islands using dual-polarimetric SAR.

Direct measurements of marine debris from satellite platforms are deemed critical for the comprehensive monitoring of the issue (Maximenko, et al., 2019). Recently, the use of SAR for detecting marine plastics has started being investigated (Salgado-Hernanz, et al., 2021; Martinez-Vicente, et al., 2019). However, particularities in the composition and size of marine debris and their interactions with the ocean background can make the direct detection of plastics using SAR data very challenging (Salgado-Hernanz, et al., 2021). A lack of test cases of SAR imagery for detecting marine debris of various forms (plastic and non-plastic) means that the capabilities of the platform are still largely unknown (Qi, et al., 2022).

In this study, we test—for the first time—the use of coherence detectors with Single Look Complex (SLC) SAR data for the detection of plastic. We present the accuracies and false alarm rates for our new method. We produce heatmaps of multiple sections of the chosen river system in Serbia and Bosnia & Herzegovina showing the plastic accumulation presence/coverage over a 2-year timeframe, and we discuss how these can be used to support management practices within the area.

2.2 MATERIALS AND METHODS

2.2.1 Study Area

The Balkans constitutes a geographic area in south-eastern Europe, usually characterised as comprising Albania, Bosnia and Herzegovina, Bulgaria, Croatia, Kosovo, Montenegro, North Macedonia, Romania, Serbia, and Slovenia. Waste management assessment of Balkan countries has found key issues within the regions (Hogg & Vergunst, 2017). Regions of Balkans, specifically Bosnia and Herzegovina and Serbia, experienced heavy rainfall in early January 2021 and consequently plastic waste and debris was washed into the river systems.

This study focuses on Potpecko Lake, Serbia and the River Drina, Bosnia and Herzegovina. These regions were selected for monitoring after reports of plastic accumulation near prominent dams in these locations on 5 and 6 January 2021. Pictures taken of the dam during this event provided validation data (Figure 2.3.). A third location, Bajina Basta hydroelectric dam, in Perućac, Serbia, was also located as it is part of the same Drina River system. While there were no reports of plastic accumulations at this third location, we undertook some analyses to understand the river system more comprehensively and to cross-check an area that was reported as clear. A map highlighting the study area and inland hydrology is shown below in Figure 2.1.

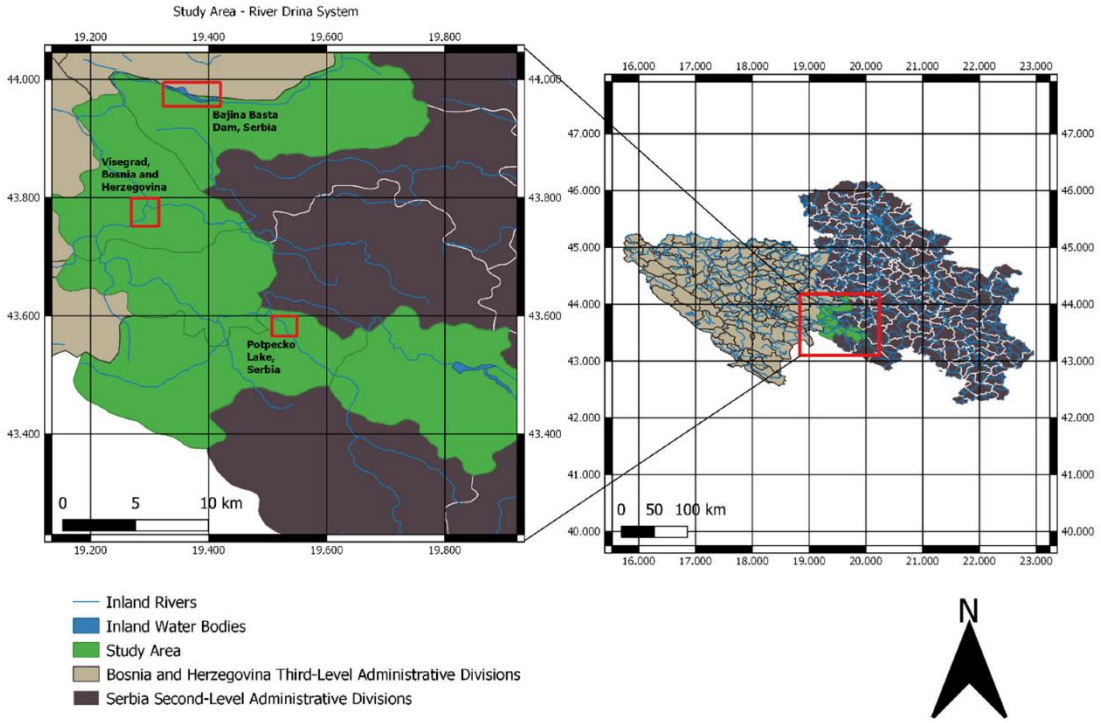

Figure 2.1 (Right) Map of Bosnia and Herzegovina and Serbia with overall study area highlighted. (Left) Focussed map of study area with three locations of interest highlighted. Data of land borders from Hijmans, J and University of California, Berkeley Museum of Vertebrate Zoology (https://geodata.lib.utexas.edu/catalog/stanford-xt594tq5034) (accessed on 12 August 2022) (Hijmans, 2015). Data of inland rivers and water bodies from Hijmans, J, DIVA-GIS. (Download data by country|DIVA-GIS) (accessed on 12 August 2022) (Hijmans, N/A).

2.2.2 Satellite Data

In this study, we used dual-polarimetric Sentinel-1 SAR data (5.405 GHz), provided by the European Space Agency (ESA) through the Copernicus Programme (https://scihub.copernicus.eu/dhus/#/home) (accessed on 5 January 2022). The mode of acquisition was Interferometric Wide Swath (IW) SLC. The spatial resolution of the SAR images was approximately 20 × 5 m with a temporal resolution of up to 6 days (12 days using a single orbit). A total of 142 SLC images were downloaded from 5 January 2019 to 26 December 2021, which were used for single image analysis and change detection analysis.

High resolution optical images from Sentinel-2 were acquired; however, cloud cover was 90+% in all images near the date of plastic build-up, so they were inadequate for use for comparison.

2.2.3 SAR Pre-Processing

In this research, we used Ground Range-Detected (GRD) products to quickly identify locations with marine debris accumulation near the dams. GRD products are SAR data that are calibrated (sigma naught), multi-looked, and projected to ground range using an Earth ellipsoid model; this results in the SAR product having reduced speckle. However, beside these preliminary analyses in this research, we wanted to gain a deeper understanding of the best detection methodologies to evaluate plastic accumulations. Therefore, we also used SLC products to consider information on both amplitude and phase of the received electromagnetic wave. Therefore, we could capitalise on polarimetric information, where we evaluated elements of the polarimetric covariance matrix that consisted of co-polarisation intensity (VV), cross-polarisation intensity (VH), and their cross-correlation (VV * VH), where V stands for vertical linear, and H stands for horizontal linear. Sentinel-1 SLC images were processed in the Sentinel Application Platform (SNAP). These images were calibrated and debursted; then, subsets were created of the regions and polarimetric matrices were established with a 1 × 4 multilook to reduce noise before undergoing ellipsoid correction.

To undertake temporal analysis on SAR imaging, pixel-to-pixel matching between features is required within stacked SAR images. Co-registration can align SAR images within a fraction of a pixel (Li & Bethel, 2008) and was therefore used to process the datasets of each region in such a way that the same pixels correspond to the same location over the entire temporal stack (Constantini, et al., 2018). The pre-processing and data analysis procedures can be seen in Figure 2.2. The analysis process is fully explained below.

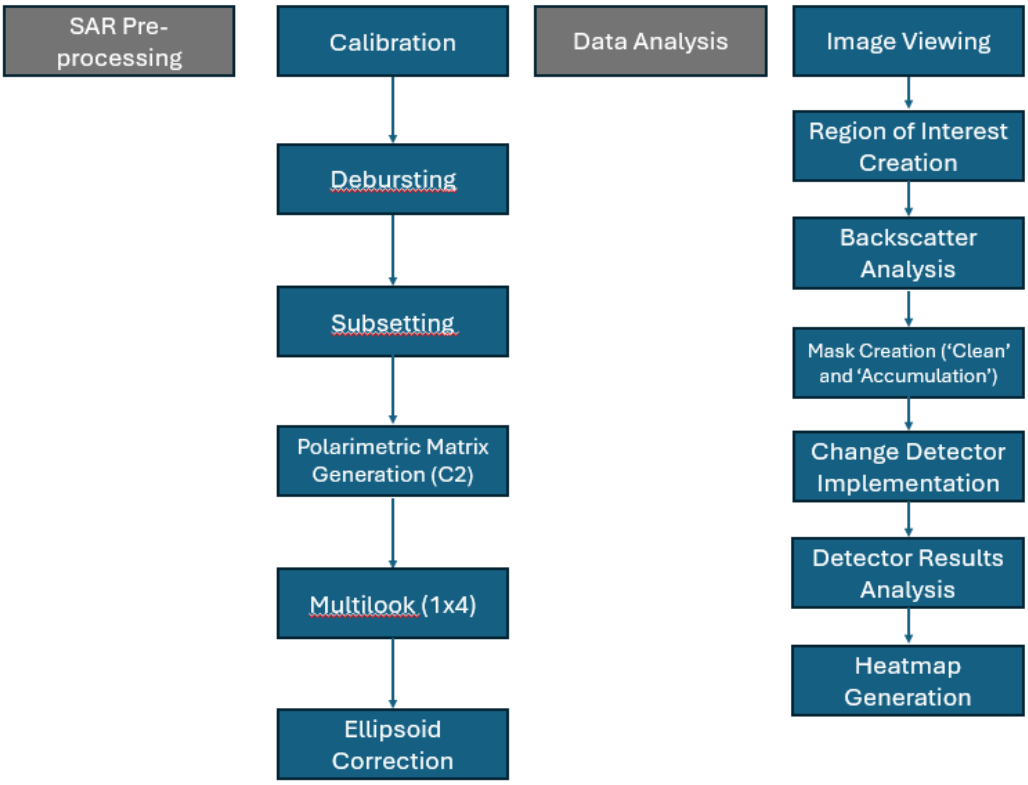

Figure 2.2. Flow diagram showing steps of SAR pre-processing and data analysis undertaken on processed Sentinel-1 SLC data.

2.2.4 Image Analysis

The dual-polarimetric Sentinel-1 GRD measurements were processed using SNAP. Inspecting the GRD images of Potpecko Lake and River Drina over multiple dates of acquisition showed that there was a clear backscatter difference near the dams before and after 5 January 2021, the date of plastic accumulation, as discussed in Section 3.

Photographs from news reports were used to identify regions of interest (ROIs) where plastic accumulation was present. The ROIs were created as shapefiles (polygons) of Clean (No Plastic) and Accumulated (Plastic Accumulation) regions.

Analysis of the images was then undertaken for the dates where ground evidence was available. The VV, VH intensity, and the Ratio of all pixels were extracted from within the ROI to provide quantitative comparisons. Histograms were then created using the values from the Clean and Accumulated pixel values from within the polygons, further illustrating the differences in backscatter values between the dates of acquisition.

2.2.5 Classifying Plastic Accumulation

We set the detection task of separating a pixel into two classes. The first class was denoted ‘clean’, which represents pixels of water within the river systems that do not have plastic accumulations. These masks were taken from days where no plastic accumulations were reported in the rivers. The second class is defined as ‘accumulated’; this includes the presence of plastic accumulations.

2.2.6 Change Detection Methods

The change detectors were used to compare references images with the rest of the stack. These images were selected from dates where no plastic accumulation was reported within the river systems (we also visually inspected them to ensure that no debris was present).

Traditional incoherent (not using the phase) detectors were used on each of the test images, including Difference, Normalised Difference, and Ratio Detectors in VV and VH polarisation channels. Newer coherent detectors (using the phase information) were also used and compared to the benchmark traditional detectors, including Optimisation of Power Difference, Optimisation of Power Ratio (Novak, et al., 1989; Marino & Nannini, 2022; Marino & Hajnsek, 2013), and the Hotelling–Lawley trace (Akbari, et al., 2016) detectors.

In the following, the main equations and references are provided for each detector.

Difference: This detector considers a reference image, and it subtracts this by the stack of images (pixel by pixel). It is referred to as Diff_XX, where XX represents the polarisation channel (e.g., Diff_VH).

The equation is:

Equation 1 $$\Delta I = |\langle |img_1|^2 \rangle - \langle |img_2|^2 \rangle| > T_1$$

Normalised Difference is referred to as NDiff_XX:

The equation is:

Equation 2 $$\Delta I_n = \frac{|\langle |img_1|^2 \rangle - \langle |img_2|^2 \rangle|}{\langle |img_1|^2 \rangle - \langle |img_2|^2 \rangle} > T_2$$

Ratio Detector: This detector divides the intensity values (pixel by pixel) between the acquisition of interest and the reference acquisition. It is referred to as Ratio_XX.

The equation is:

Equation 3 $$p_1 = \frac{\langle |img_1|^2 \rangle}{\langle |img_2|^2 \rangle} > T_3$$

Optimisation of Power Ratio: This detector performs an optimisation using polarimetric data in the format of covariance matrices. It looks for the best linear combination of polarimetric channels that optimises the contrast between a reference and an image of interest. The detector finds the optimal scattering mechanism by diagonalizing an appropriate matrix operator, and the eigenvalues are the distances used here in the following statistical test. We refer to it as Pow1 for the maximum eigenvalue and Pow2 for the other eigenvalue.

The equation is:

Equation 4 $$p_c = \frac{\underline{\underline{\omega}}^{*T} [T_{11}] \underline{\underline{\omega}}}{\underline{\underline{\omega}}^{*T} [T_{22}] \underline{\underline{\omega}}} = \frac{P_1}{P_2}$$

Equation 5 $$[T_{22}]^{-1} [T_{11}] \underline{\omega} = \lambda \underline{\omega}$$

Optimisation of Power Difference: This algorithm also uses the PolSAR data in a covariance matrix format. It optimises the differences between two covariance matrices by finding the linear combination of polarimetric channels that provides the highest (or smallest) difference between the two polarimetric partial targets (Novak, et al., 1989). Again, this is performed using a diagonalisation and the distance is represented by the eigenvalues. In the following, we refer to dif1 for the maximum eigenvalue and dif2 for the other one.

The equation is:

Equation 6 $$\Delta = \underline{\omega}^{*T} [T_{22}] \underline{\omega} - \underline{\omega}^{*T} [T_{11}] \underline{\omega}$$

$$\Delta = \underline{\omega}^{*T} ([T_{22}] - [T_{11}]) \underline{\omega} = \underline{\omega}^{*T} [T_c] \underline{\omega}$$

$$[T_c] \underline{\omega} = \lambda \underline{\omega}$$

Hotelling–Lawley Trace (HLT): This detector evaluates the dissimilarity of two covariance matrices using the following equation (Akbari, et al., 2016).

Equation 7 $$int_N = Trace\{T_{22}^{-1}T_{11}\}$$

Interestingly, when noting the matrix that is used in by the algorithms $T_{22}^{-1}T_{11}$, it is possible to see that HLT is related to the Optimal Ratio, where a trace of a matrix looks at the means of all the possible combinations of projection vectors for that quadratic form (Marino, 2017).

2.2.7 Quantitative Comparison and Statistical Test for Setting Threshold

For producing quantitative comparisons, the pixels used as classes of Clean and Accumulated were obtained in the following way. Clean images were used as reference images to create ROIs that encompass areas of clean water (Clean). Accumulated images were used as test images to create ROIs that encompass areas of plastic accumulation (Accumulated). These images were selected from dates that were acquired closest to reported events of plastic accumulation.

Receiver Operator Characteristic (ROC) curves were used to evaluate the performance of each of the implemented detectors (Akobeng, 2007). In making the ROC, the set of thresholds were varied, and the probability of detection (Pd) was obtained by counting the detected pixels in the Accumulated ROI while the probability of false alarms (Pf) was determined by counting the detected pixels in the Clean ROI.

ROC curves are very useful for evaluating the best-performing detectors, but when it comes to creating an operational algorithm with the best of the detectors selected, we need to set the threshold. For this, we employed a statistical approach. Using the ROI developed for the Clean area, we performed statistical modelling while fitting different distributions. The one with the best fit was the generalised gamma (results provided in following section). Once the parameters for the gΓ were extracted, we performed a Constant False Alarm Rate (CFAR), setting a sorted value for the probability of false alarms. The algorithm is adaptive since it extracts the gΓ on each image in the clean area of the reservoir and provides robustness against wind effects.

2.2.8 Heatmap Creation

Once we acquired all the detection maps, the images were summed in time and divided by the number of acquisitions (n = 142). From this, a percentage of the times

the plastic was detected within the river system was obtained, which is illustrated as a heatmap of each region of interest within the river system.

2.2.9 Scattering Model for Plastic Accumulation

The scattering from objects is strongly dictated by the dielectric constant (together with other factors including shape and size). Dielectric constant, or relative permittivity, is a property of materials that indicates how much electric potential energy is stored in the material when it is subjected to an electric field, compared to the amount of energy when stored in a vacuum. The dielectric constant affects how deeply the radar signal can penetrate through the material. Materials with high dielectric constant (i.e. water and metals) will attenuate the radar signal more than materials with a low dielectric constant (i.e. plastics, dry soil or sand). The real part of the dielectric constant dictates the amount of scattering—for plastic, this is relatively small (proximal to 1). Therefore, we do not expect plastic to scatter directly. However, we hypothesise two mechanisms that can provide an increased backscattering compared to clean water as seen in Figure 2.33.

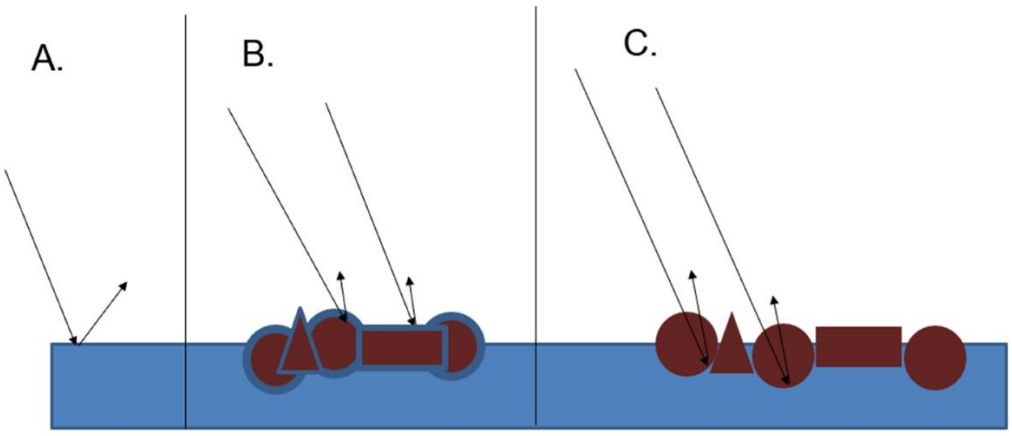

Figure 2.3 Radar backscatter interacting in different scenes. (A) Specular reflection of signal from calm water with no material inside water, (B). A change in backscatter from ‘wet’ plastics that are partially submerged with a thin layer on water on top, (C). A change in backscatter from ‘dry’ plastics that are partially submerged with no water on top.

Water with no plastic will have a smooth surface calling for the specular reflection of signal. This produces dark areas in SAR images.

The phenomenon determining whether or not radar waves penetrate any medium is controlled by the imaginary part of the dielectric constant of the particular medium. A medium with high imaginary part of the dielectric constant, such as water, will be

mostly impenetrable (mm or cm penetration depth, depending on several factors including frequency and salinity). Therefore, when a thin layer of liquid water (1 mm would be sufficient) is on top of the plastic, the dielectric constant seen by the radar will be increased and the plastic may be able to start scattering.

On the other hand, when the imaginary part of the dielectric constant is low, the medium can be penetrated easily without loss, as is the case for plastic. Therefore, the plastic is penetrated; however, it still produces an effect on the water underneath by producing indentations and extra roughness. This extra roughness will induce a scattering from the surface (as if wind was present).

2.3 RESULTS

2.3.1 Initial Observations of Plastic Accumulations by Dams

The results of this work were validated by photographs of the accumulations in Potpecko Lake and River Drina. These validations were taken from news articles reporting on the accumulations from the 5 January 2021, as seen in Figure 2.4.

(**A**) (**B**)

Figure 2.4 (A). Accumulation of litter debris, primarily plastic, near Potpecko Lake hydroelectric dam, Serbia, 5 January 2021. (Credits: REUTERS/Branko Filipovic). (B). Accumulation of litter debris, primarily plastic, near River Drina hydroelectric dam, 5 January 2021 (Credits: Euronews).

2.3.2 Preliminary Analysis of Backscattering: Potpecko Lake, Serbia

The preliminary inspection of the Sentinel-1 data from 6 January 2021 (the closest acquisition after reports of accumulation) showed higher backscattering from the water bodies in the area before the dam (i.e., just upstream of the concrete), which was visually similar to the ground inspection images. The dates of the ‘clean’ images (dates where no plastic accumulations were reported) were inspected and these patches of brighter backscattering were not visible.

The initial sighting of possible accumulations was promising as it showed that changes in the surface roughness were visible from dates with and without the plastic accumulations reported.

In Figure 2.55, we can see an image from 6 January 2021 showing the VV channel intensity (Figure 2.5 A). Please note the ground validation was carried out on 5 January 2021 (one day before the S1 acquisition). A polygon was established to cover the area of plastic accumulation near the dam, as seen in Figure 2.55 (B). This location was selected as it showed clear changes in the backscatter, which were associated with the debris accumulation near the dam. The histogram of the highlighted area is shown in Figure 2.55 (C), where we can see that the intensity values of the pixels are slightly left skewed, with the peak at the higher range of intensity values in the histogram. The mode is around −7 dB.

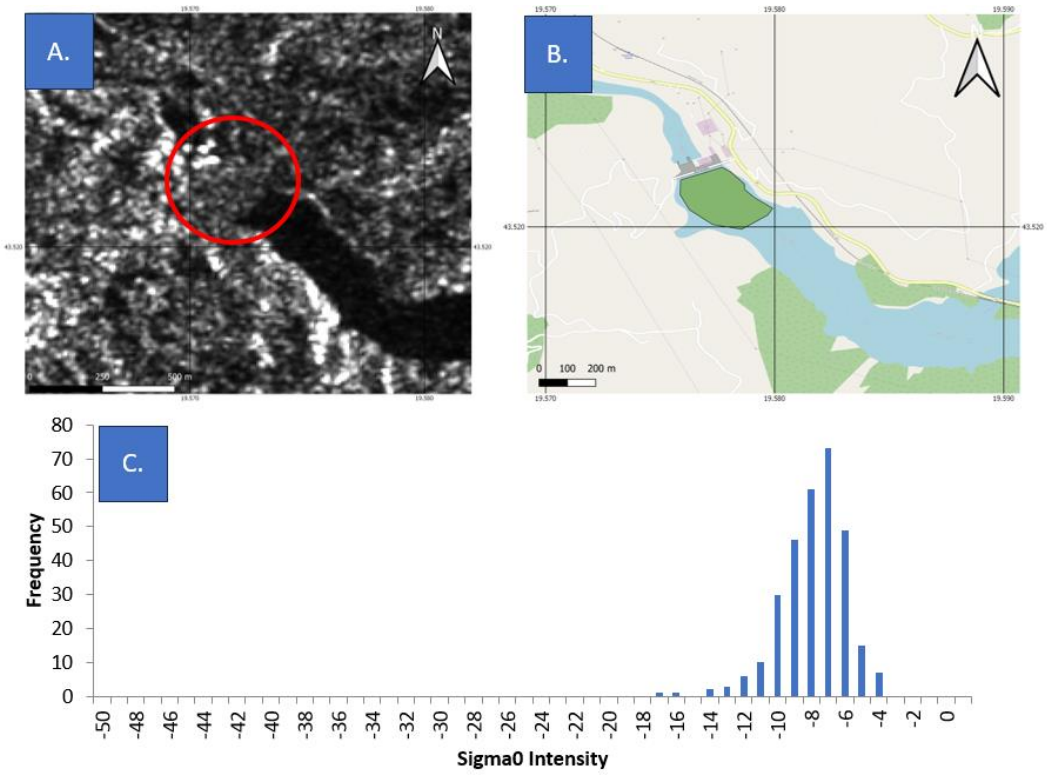

Figure 2.5 Image from 6 January 2021, in Sentinel-1 VV channel showing plastic accumulation near Potpecko Lake hydroelectric dam, Serbia. (A) VV Intensity with red marker highlighting dam and accumulation, (B) Polygon used for histogram, and (C) Histogram of pixels in polygon (Sentinel-1, Credits: ESA).

Figure 2.6 was used as a comparison, showing the VV intensity channel from 5 May 2020, a date in which no plastic accumulation was reported by the dam. The same shapefile from Figure 2.55 (B) was used in Figure 2.6 (B) so that a similar number of

pixels were collected from the same coordinates near the dam. In Figure 2.6.C, we can see that the distribution of pixels looks more similar to a normal distribution as the peak is more central and it is more symmetrical. The mode is around −22 dB. A comparison between Figure 2.55 (C) and Figure 2.6 (C) clearly shows that there is a difference in the distribution of VV intensities from these dates with a difference between the modes of around 14 dB.

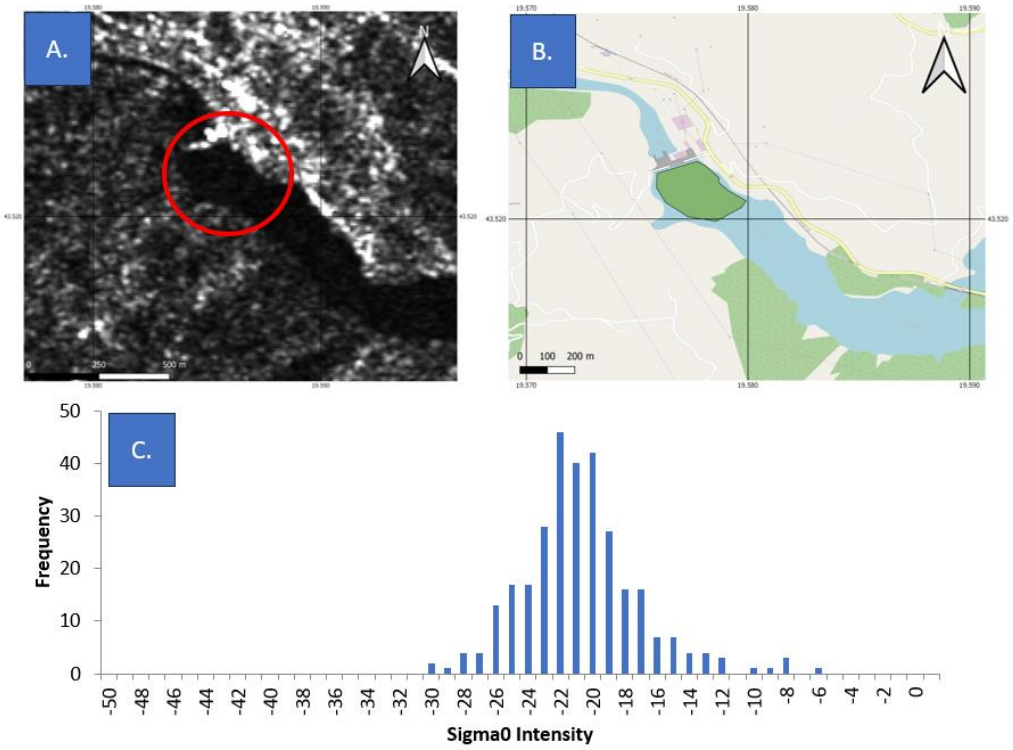

Figure 2.6 Image from 5 May 2020 in Sentinel-1 VV channel showing Potpecko Lake hydroelectric dam, Serbia. (A) VV Intensity with red marker highlighting dam, (B) Polygon used for histogram, and (C) Histogram of pixels in polygon (Sentinel-1, Credits: ESA).

2.3.3 River Drina, Bosnia and Herzegovina

In Figure 2.77, we can see an image from 6 January 2021 showing the VV channel intensity (Figure 2.7 A). The ground validation was carried out on 5 January 2021. A polygon was established to cover the area of plastic accumulation near the dam, as seen in Figure 2.7 (B). This location was selected as it showed clear changes in backscatter, associated with the debris accumulation near the dam. The histogram of the highlighted area is shown in Figure 2.7 (C), where we can see that the intensity values of the pixels are more normally distributed, with the peak at the higher range of intensity values in the histogram.

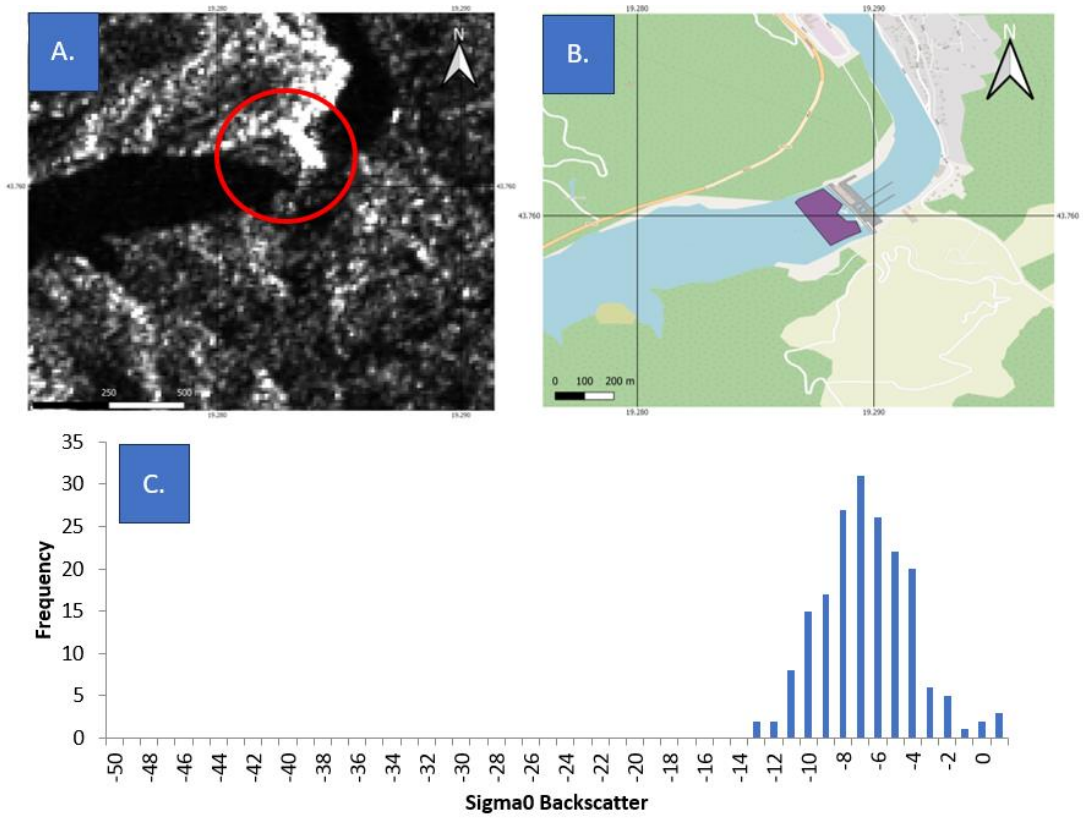

Figure 2.7 Image from 6 January 2021 in Sentinel-1 VV Channel showing plastic accumulation near River Drina hydroelectric dam, Bosnia & Herzegovina. (A) VV intensity with red marker highlighting dam and accumulation, (B) Polygon used for histogram, and (C) Histogram of pixels in polygon (Sentinel-1, Credits: ESA).

Figure 2.8 was used as a comparison, showing the VV intensity channel from 5 May 2020, a date in which no plastic accumulation was reported by the dam. The same shapefile from Figure 2.77 (B) was used in Figure 2.8 (B) so that a similar number of pixels could be collected from the same coordinates near the dam. A comparison between Figure 2.7 (C) and Figure 2.8 (C) shows that there is a difference in the distribution of intensity of around 10 dB.

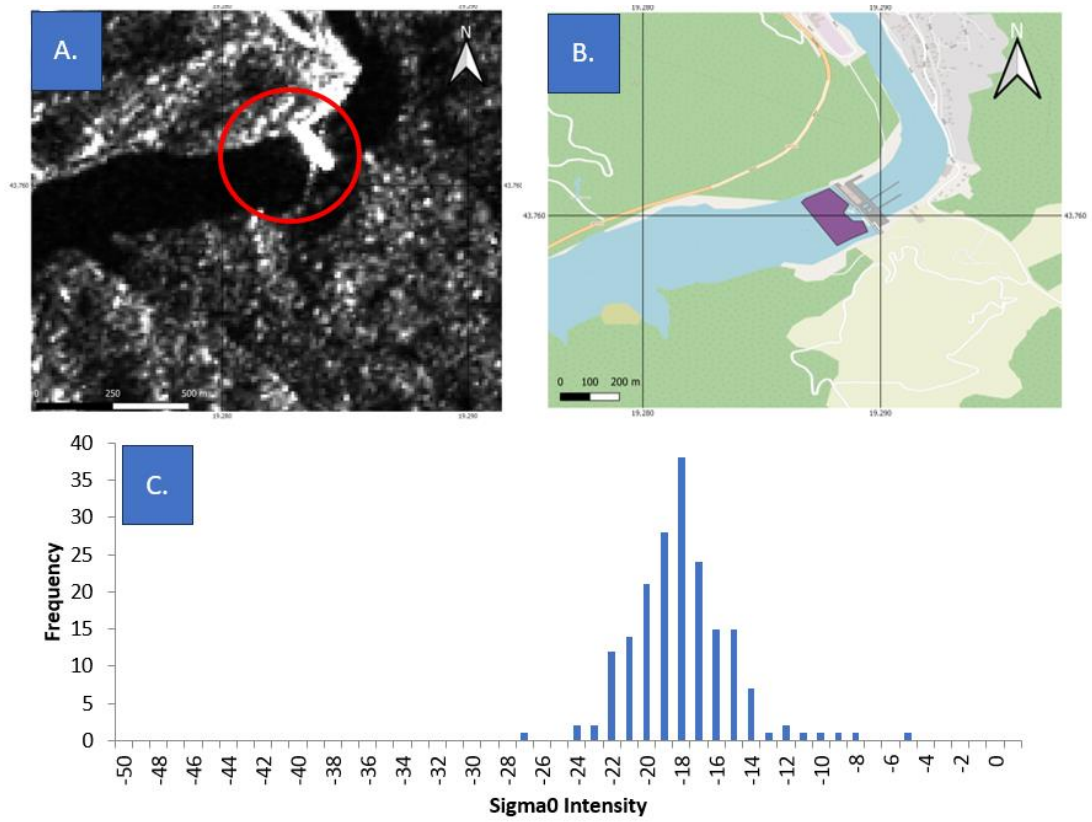

Figure 2.8 Image from 4 June 2020 in Sentinel-1 VV Channel showing River Drina hydroelectric dam, Bosnia & Herzegovina. (A) VV intensity with red marker highlighting dam and accumulation, (B) Polygon used for histogram, and (C) Histogram of pixels in polygon (Sentinel-1, Credits: ESA).

2.3.4 Mask Creation and Detector Analysis

The ROC curves were obtained by using masks of Clean and Accumulated regions of the Potpecko Lake and River Drina. Two separate, non-overlapping regions were selected for the clean and accumulated masks as in Figure 2.5 (B) and Figure 2.7 (B). The accumulated mask was used to evaluate the probability of detection and the Clean mask was used to evaluate the probability of a false alarm.

For the Clean mask of Potpecko Lake, we used pixels from 5 May 2020 since these show clean water (Figure 2.9).

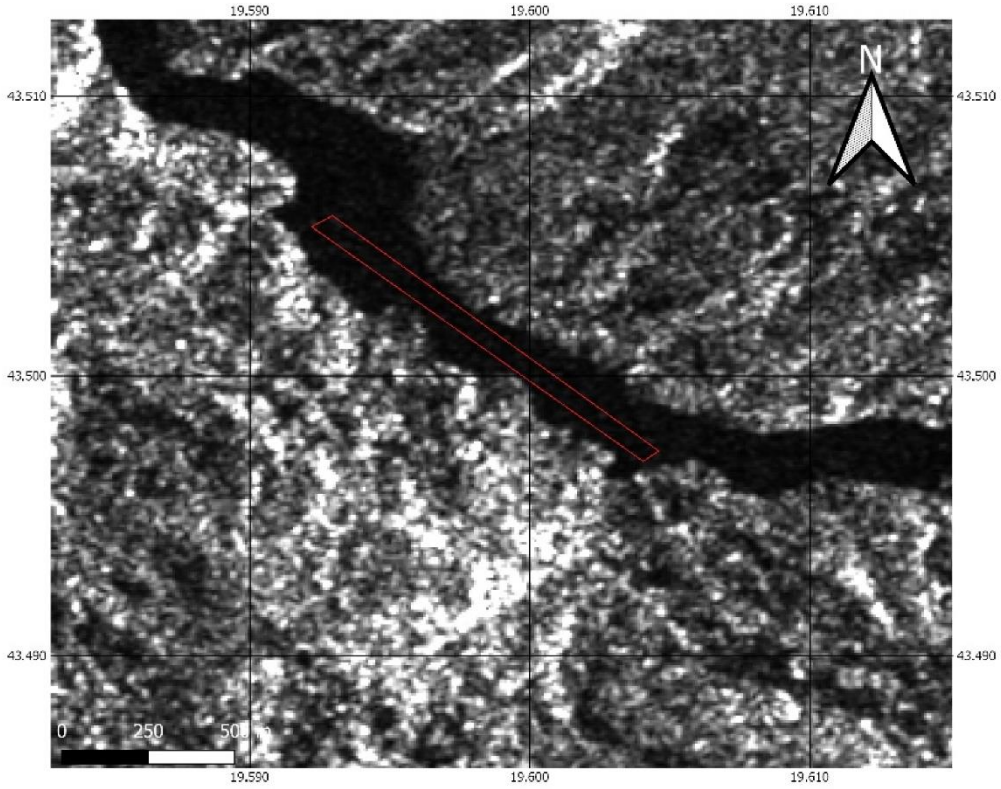

Figure 2.9 Mask of Clean region within Potpecko Lake, Serbia, 5 May 2020. The red polygon highlights the region used for the clean mask (Sentinel-1, Credits: ESA).

For the Clean mask of the River Drina, we used pixels from 4 June 2020 as shown in Figure 2.10.

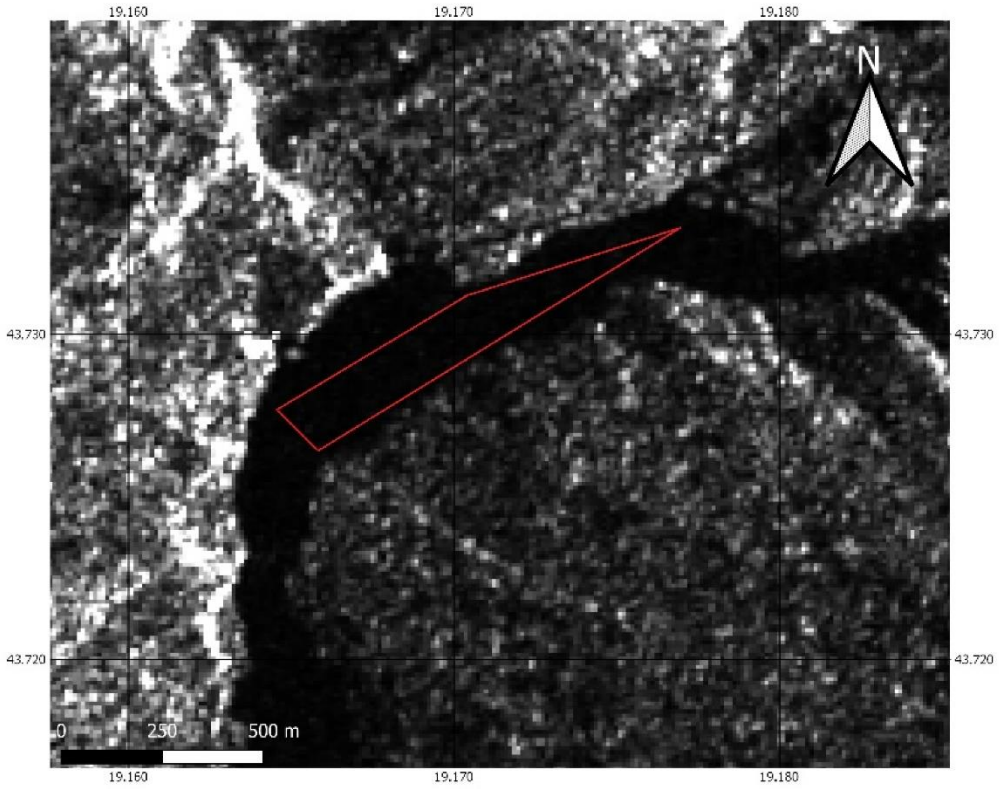

Figure 2.10 Mask of Clean region within River Drina, Bosnia & Herzegovina, 4 June 2020. The red polygon highlights the region used for the clean mask (Sentinel-1, Credits: ESA).

The Difference, the Normalised Difference, the Ratio Detectors in VV and VH polarisation channels, and the Power Difference, Power Ratio, and Trace Detectors were implemented across the Clean and Accumulation dates, using the masks selected within each image.

A ROC curve was then created to assess the accuracy of these detectors showing the probability of detection against the probability of a false alarm.

Figure 2.11 shows the ROC curve assessing the ability of the change detectors to classify the Potpecko Lake's plastic accumulation from 6 January 2021. On the Y-axis, we see the probability of detection (Pd), or true positive; on the X-axis, we can see the probability of false alarm (Pf), or false positive. The Pd indicates how many correct positive detections of plastic accumulation occurred within the sample masks. The Pf indicates how many incorrect positive detections occurred within the sample masks.

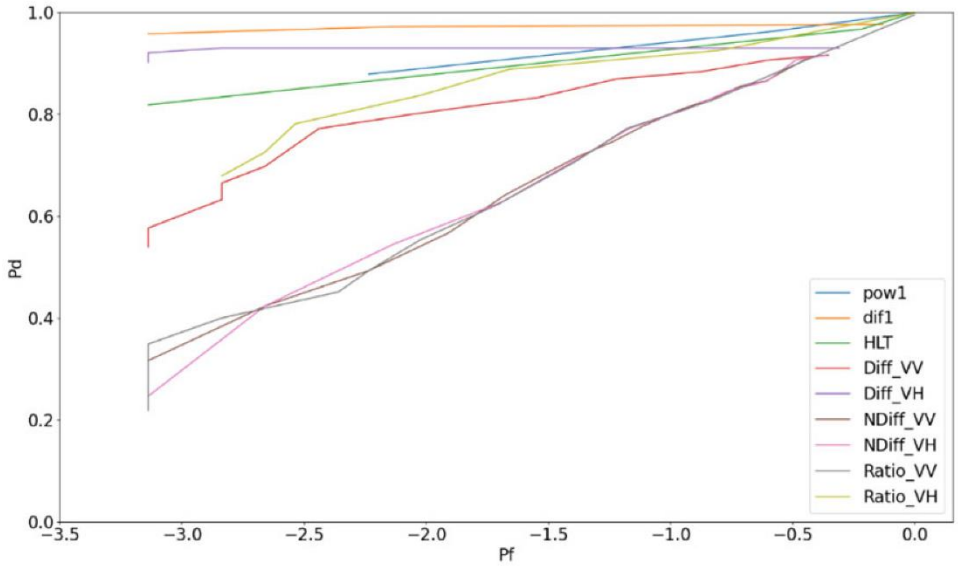

Figure 2.11 ROC Curve in a Log10 format showing Potpecko Lake Data change detectors: Difference VV & VH (Diff_), Ratio VV & VH (Ratio_), Normalised Difference (NDiff_), Power Difference (Dif1), Power Ratio (Pow1), and Trace (HLT). X-axis signifies 10^{-X}.

Figure 2.11, with Log10 for the false alarms, allows us to more clearly see the smaller values of probability of false alarms, which are also the most interesting operationally. Knowing this, we can see that Figure 2.11 shows the power difference (dif1) and difference in VH detectors as the most accurate detectors out of the algorithms tested, with a true positive detection rating of 95% and 90%, respectively, with 0.1% false alarms. We can also see that the Ratio_VV, NDiff_VV, and NDiff_VH detectors perform poorly, with average detection ratings of 20% with a 0.1% false alarm rate. We can also see the single polarisation VV channel performs poorer than the cross-polarisation VH channel when used in the Diff_X detectors, with an increase of >30% accuracy in the cross-pol detector. We did not show the second eigenvalues, dif2 and pow2, since these had worse performance of the first eigenvalues.

A ROC curve was also generated for the River Drina masks, as seen in Figure 2.122.

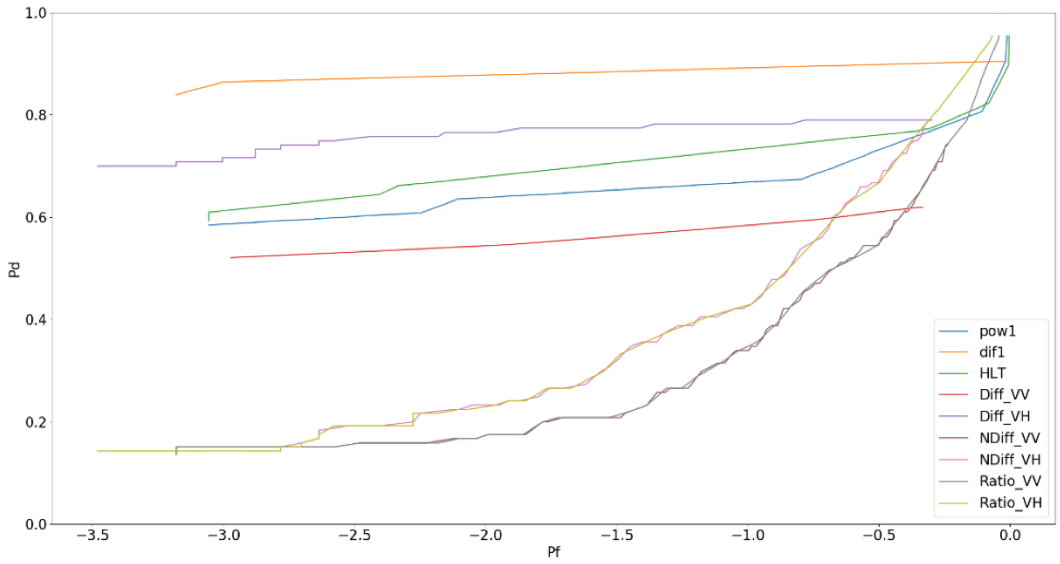

Figure 2.12 ROC Curve in a Log10 format showing River Drina Data change detectors: Difference VV & VH (Diff_), Ratio VV & VH (Ratio_), Normalised Difference (NDiff_), Power Difference (Dif1), Power Ratio (Pow1), and Trace (HLT).

Figure 2.12 shows the ROC curve assessing the ability of the change detectors to classify the River Drina's plastic accumulation from 6 January 2021. We can see that Figure 2.12 shows the power difference (dif1) and difference in VH detectors as the most accurate detectors out of the algorithms tested, with a true positive detection rating of 70–85% with a 0.1% false alarm rate. We can also see once more that the NDiff_VV, NDiff_VH, and Ratio_VH detectors perform poorly. Once again, we can see that the cross-pol VH channel performs with a higher accuracy when compared with the single-pol VV channel in the Diff_X detectors, with a 20% increase in accuracy.

2.3.5 Testing the Statistical Modelling

Using the ROIs developed for the clean masks, we performed statistical modelling while fitting different distributions. The best statistical fit was the generalised gamma, which is shown for the clutter of each of the regions of interest in Figure 2.13, Figure 2.14 and Figure 2.15. These were used to test that the modelling was correct so we could set a threshold using a constant false alarm rate. A third location, the Bajina Basta hydroelectric dam, Perućac, Serbia, was also used as it is part of the same Drina River system. While there were no reports of plastic accumulations at this third location, we undertook some analyses to better understand the river system and to cross-check an area that was reported as clear.

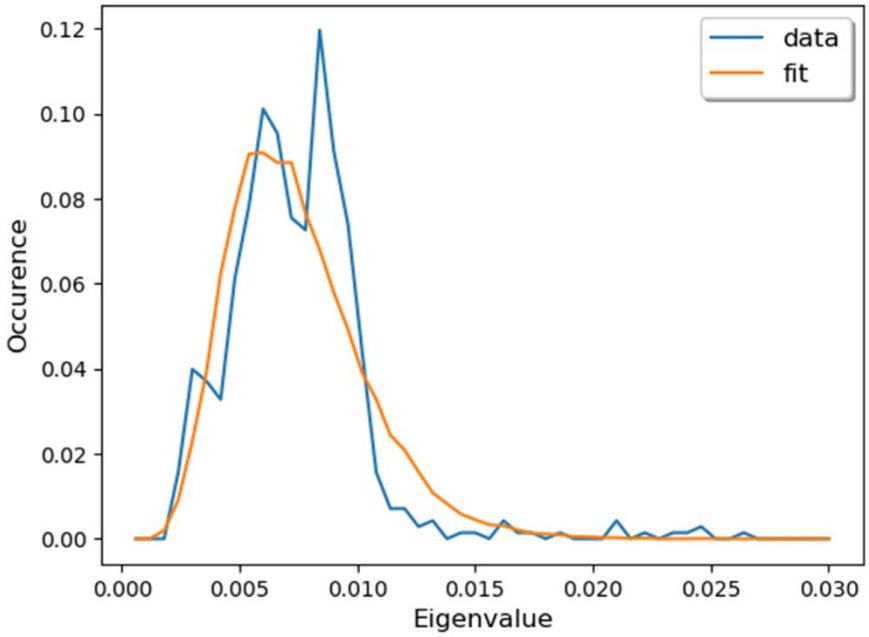

Figure 2.13 Statistical-model-fitting-generalised gamma distribution over clean pixels used in Potpecko Lake clean mask.

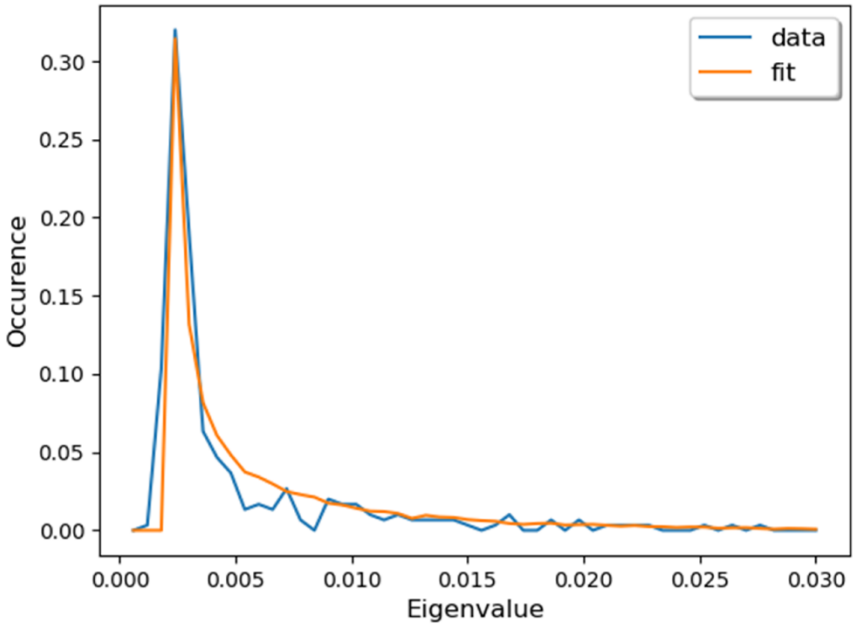

Figure 2.14 Statistical-model-fitting-generalised gamma distribution over clean pixels used in Visegrad clean mask.

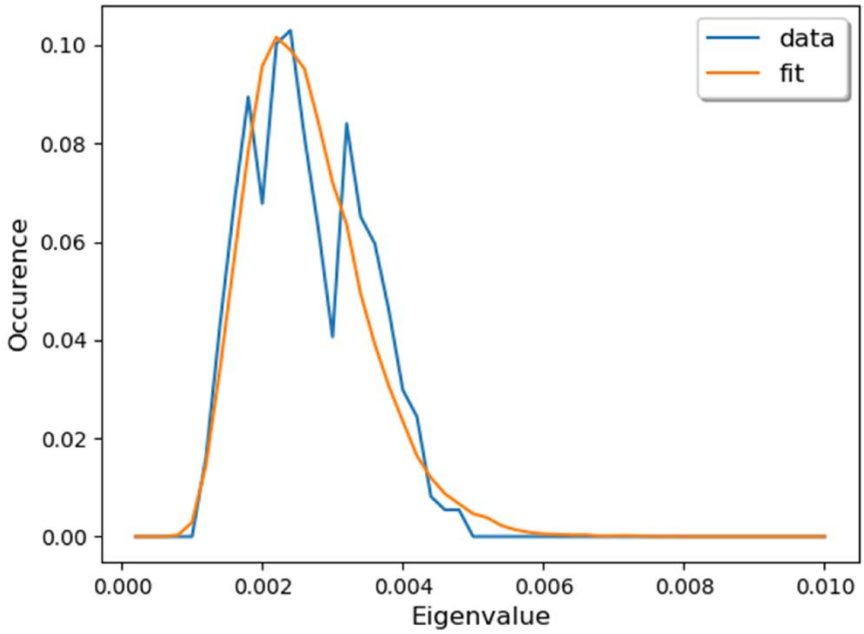

Figure 2.15 Statistical-model-fitting-generalised gamma distribution over clean pixels from Bajina Basta clean mask.

From Figure 2.133, Figure 2.14 and Figure 2.15, it is possible to see that the model (orange line) overall follows the histogram of the data (blue line). Please note that some of the divergences may be due to the limited number of samples in the cluster area. Additionally, the fit is best when following the right tails of the distributions, which are the places where the CFAR threshold is set. A further study will be carried out with respect to trying to derive an ad hoc analytical distribution for the clutter; however, we believe this is outside the purpose of this initial work.

2.3.6 Heatmap Creation on Different Regions of Study

From Figure 2.13, Figure 2.14 and Figure 2.15 it is possible to see that the model (orange line) overall follows the histogram of the data (blue line). Please note that some of the divergences may be due to the limited number of samples in the cluster area. Additionally, the fit is best when following the right tails of the distributions, which are the places where the CFAR threshold is set. A further study will be carried out to try to derive an ad hoc analytical distribution for the clutter; however, we believe this is outside the purpose of this initial work.

To understand the patterns of the plastic accumulations within each river system, heatmaps were created. The Optimisation of Power Difference detector was used for the detection of the accumulations as it was the best-performing detector from those

tested. On the following heatmaps, areas of darker yellows/reds signify locations that were prominent in the detection of accumulations within the river systems.

Figure 2.16 shows that there is a significant build-up of material near the hydroelectric dam over the timeframe, but also shows a build-up further upstream within the system, which could be an inflow of accumulation into the river system or another location where material becomes stuck within the river system. Reports of the accumulation in the River Drina near Visegrad showed that plastics were reported in January and February of 2021 (Emric, 2021) and that the plastic accumulations re-occur at the beginning of every year (Gomez, et al., 2022).

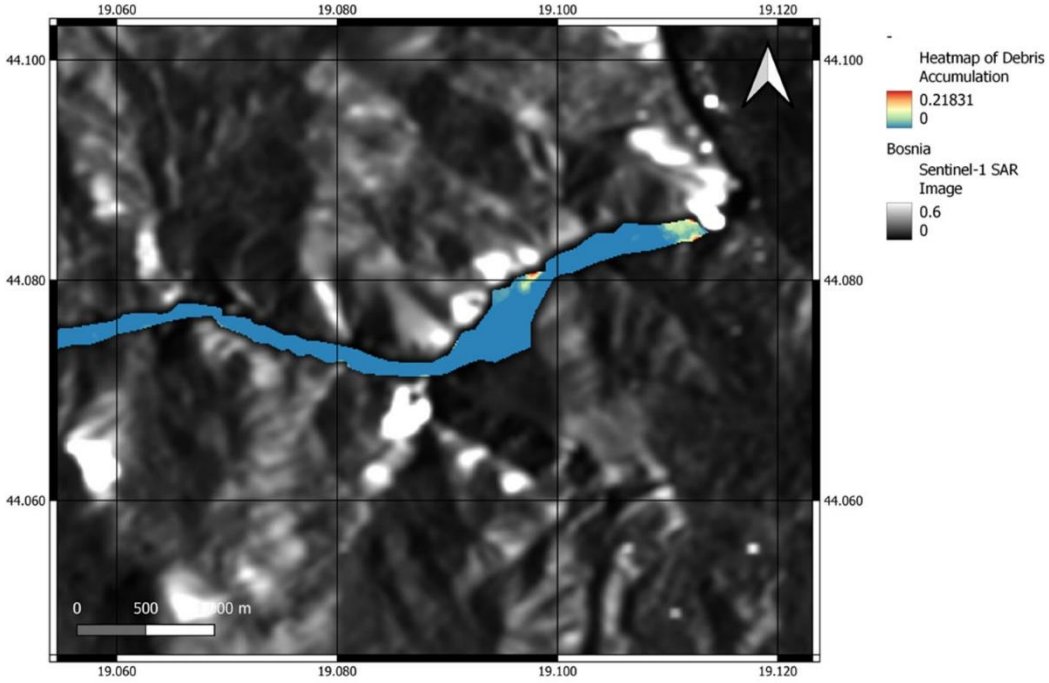

Figure 2.16 Heatmap of Drina River system and hydroelectric dam near Visegrad from 5 January 2019 to 26 December 2021 (total 142 acquisitions) (Sentinel-1, Credits: ESA).

Figure 2.17 once again shows a significant build-up of material near the dam, but we also see this phenomenon slightly upstream where there is some accumulation on the bends of the river, and this once again could be another location where material can become stuck within the system.

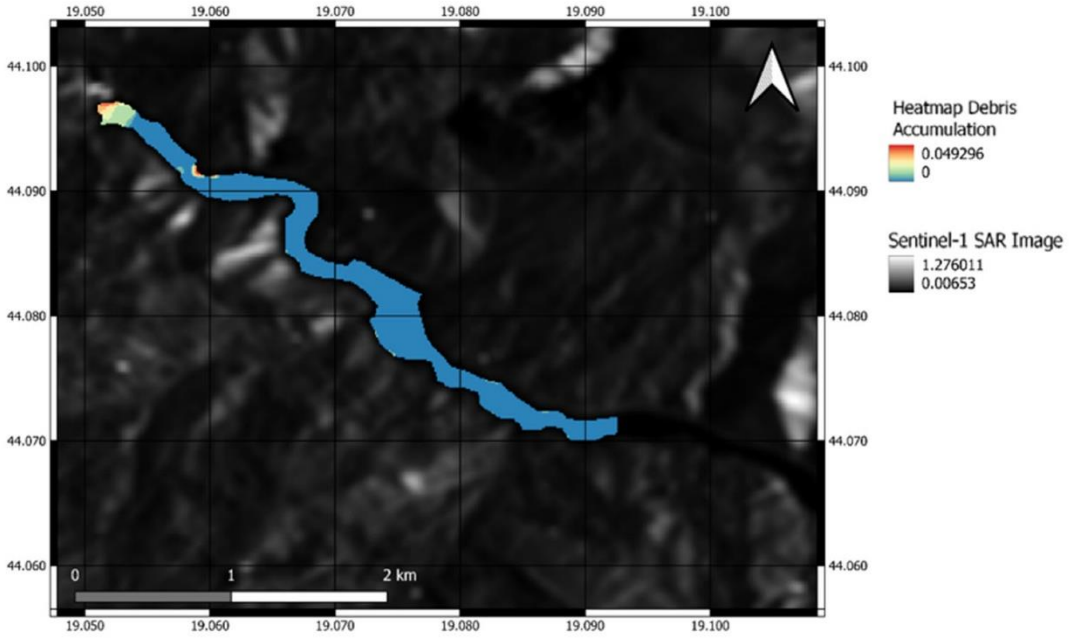

Figure 2.17 Heatmap of Potpecko Lake system and hydroelectric dam from 5 January 2019 to 26 December 2021 (total 142 acquisitions). Basemap: multitemporal average of Sentinel-1 VV images. Colour: heatmap (Sentinel-1, Credits: ESA).

Figure 2.18 and Figure 2.19 show the heatmaps of a third dam in which there were no reports of plastic accumulations from any dates used within this study. We assume that no major accident occurred in this part of the river system, but we have no certainty that a small accumulation still might have occurred but was unreported. Figure 2.18 shows the larger river system leading up to the dam and we can see a lack of accumulations on the heatmap. The minor colour changes on the heatmap can be attributed to a boating dock and floating houses within the river system that have minor activity near them throughout the year, and these can be seen in the Google Earth image below (Figure 2.20). Figure 2.19 shows the small channel that flows after the hydroelectric dam, where we can see some locations highlighted through the heatmap. The minor colour changes (the red represents a detection of four times in 3 years) on the heatmap in this location can be attributed to white waters that will cause disturbance at different times of the year and also embankments that can change throughout the year as this is a narrow channel. These can also be seen in the Google Earth image below (Figure 2.21).

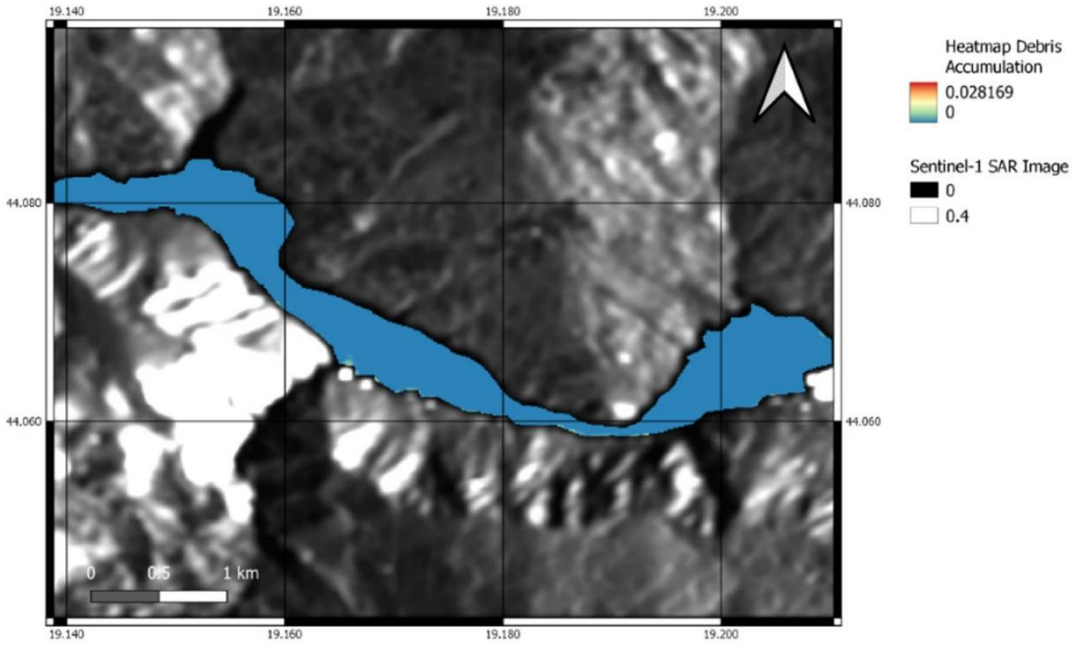

Figure 2.18 Heatmap of Drina River system and Bajina Basta hydroelectric dam near Perućac, Serbia, from 5 January 2019 to 26 December 2021 (total 142 acquisitions). Basemap: multitemporal average of Sentinel-1 VV images. Colour: heatmap. (Sentinel-1, Credits: ESA).

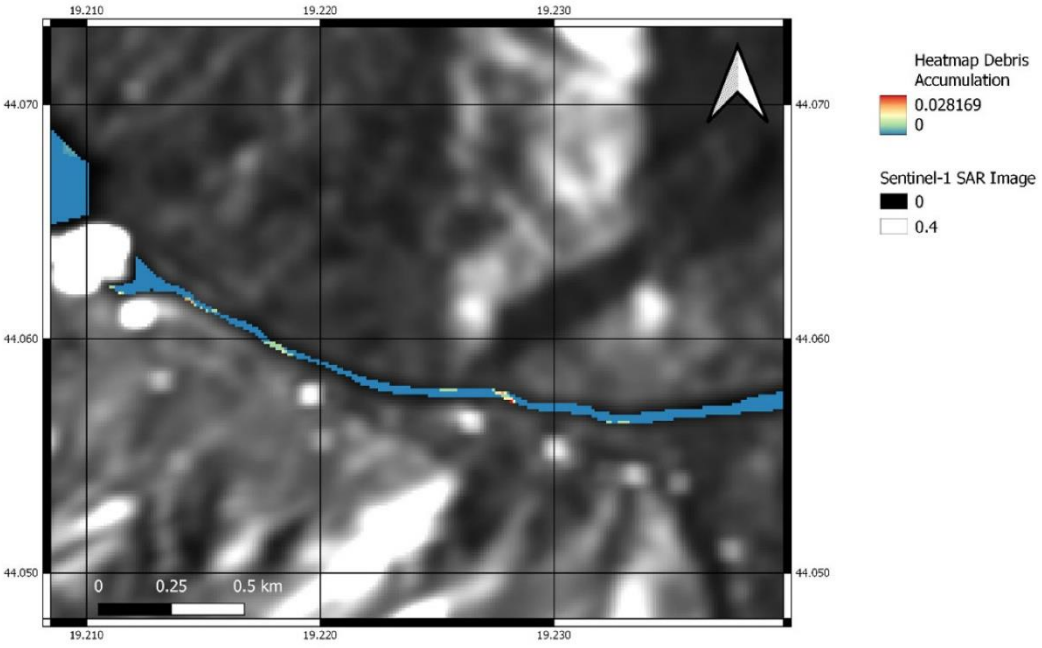

Figure 2.19 Heatmap of Drina River system after Bajina Basta hydroelectric dam near Perućac, Serbia, from 5 January 2019 to 26 December 2021 (total 142 acquisitions). Basemap: multitemporal average of Sentinel-1 VV images. Colour: heatmap. (Sentinel-1, Credits: ESA).

Figure 2.20 RGB image of Drina River system near Bajina Basta hydroelectric dam, Serbia, acquired 28th August 2020. Floating houses and docks can be seen on the southern side of the river system. (Credits: Google/CNES Airbus).

Figure 2.21 RGB image of Drina River system after Bajina Basta hydroelectric dam, Serbia, acquired 28th August 2020. Areas of white water and embankments seen throughout the system. (Credits: Google/CNES Airbus).

2.4 DISCUSSION

2.4.1 Visibility of Plastic Accumulation

The first goal of this work was to validate that plastic accumulations near the analysed dams were visible using SAR imagery. Through the processing of Sentinel-

1 SAR data taken from Potpecko Lake and River Drina, the plastic accumulations appear visible in the intensity images. The validation provided by news reports helped locate where plastic accumulations had occurred within the regions. The change in the surface roughness and backscatter caused by the presence of a large accumulation of plastic enabled greater visibility (Figure 2.5, Figure 2.6, Figure 2.7 and Figure 2.8).

2.4.2 Detectors

The ROC curves in Figure 2.11 and Figure 2.12 show that the optimisation of the power difference (dif1) detector performed the best out of the tested detectors. The results from both datasets indicate 85–95% positive detections with a 0.1% false alarm rate. If only GRD data are available, the best detector would be the Difference_VH detector with positive detections ranging from 70–90% with a 0.1% false alarm rate. The Potpecko lake dataset had higher positive detection ratings with respect to all the detectors; we hypothesise that this is due to the more homogenous layer of accumulation in front of the dam. The Hotelling–Lawley Trace and the Optimisation of Power Ratio also performed well when used on both datasets. The increase in accuracy in the power difference/ratio and trace detector compared to the majority of traditional detectors can be attributed to the better capability of the coherent data (i.e., using the polarimetric phase) to discriminate between the backscattering of water from the backscattering of debris. Once we used SLC images, we gained an extra dimension in our search space. This is the complex cross-correlation between HH and HV, which can be derived using the covariance matrix formalism. This extra dimension is important for extracting polarimetric information that would be lost otherwise. Additionally, besides the physical interpretation, the extra dimension allows us to design more powerful techniques based on multi-dimensional signal processing.

As mentioned, in case only GRD data are available and the complex-cross correlation cannot be calculated, the use of the cross-pol channel intensity provides better detection than those based on single-pol VV polarisation. Specifically, we think that the VV channel on its own may be sub-optimal in the C-band due to the stronger return from the water surface.

Previous studies on optical data have shown varying results when detecting plastic materials. Biermann et al, (2020) showed an accuracy of 86% for successfully classifying floating macroplastics in Sentinel-2 optical satellite imagery, using spectral shape and a Naïve Bayes algorithm to classify mixed materials. Garcia-Garin et al.

2021 found an accuracy of 81% in their best-performing model when attempting the detection of floating marine litter debris in aerial images. Basu, et al., 2021 used a supervised Support Vector Regression (SVR), semi-supervised fuzzy C-means, unsupervised K-means, and unsupervised fuzzy C-means clustering classification algorithms to attempt to classify floating marine litter in Sentinel-2 imagery of coastal waterbodies. The highest accuracy obtained was found in the SVR-based supervised classification, which had an accuracy ranging from 96.9–98.4%, whereas the other methods ranged between 35.7–82.2%. Topouzelis, et al., (2020) used matched filtering on Sentinel-2 data in combination with UAV data to try and classify pixels of plastic targets in coastal waters. However, they found that when matched filtering is applied to a larger coastal area, many false positives can be found around the coastline, due to bottom reflectance, vessels, cloud shadows, and other factors. With regard to monitoring marine plastics with radar, Topouzelis, et al., (2019) also attempted to use Sentinel-1 (5.405 GHz) SAR imagery to monitor and detect plastic litter targets off the coast of Lesvos, Greece. A backscattering difference was found between a 10 × 10 m target made from plastic bottles and the surrounding water. However, no differences were found between two other targets of the same size, made from plastic bags and from fishing nets; these observations were all made in VV polarized Sentinel-1 imagery. The detectors used in this study show similar, and greater, accuracies (85–95%) when used on these plastic accumulations, and we have also shown that the use of the cross-polarization VH channel provides better accuracies when compared with the single polarisation VV channel.

2.4.3 Heatmaps

The heatmaps of the known accumulations show that debris is a common occurrence within this river system. This was seen not only near the dams themselves but also further up the river system, where areas could potentially trap material. The usage of this heatmap can aid future work within the river system, either to locate inflows of material into the system or locating where material becomes trapped on its course to the dam. This can be used to target control measures within the system, such as utilising debris immobilisers seen in the Visegrad section of the River Drina, and can help slow the debris and remove it before it reaches the dams.

2.5 FUTURE WORK

In theory, wind effects could trigger detection if the meteorological conditions are largely different from the ones experienced in the reference images. The wind may produce a large backscattering (mostly in the VV polarisation channel) that may trigger the detector. Throughout our analysis, we never saw any heatmaps where large portions of the river were flagged, which would be a clear indication of wind effects. However, we cannot exclude that in some river systems high winds could produce this effect. In those cases, to remove these false alarms, we plan to use a morphological filter with a threshold on the number of connected pixels flagged inside a shapefile covering the river section. For instance, an area larger than a few hectares is likely to not be related to plastic accumulation. This maximum size for the patch depends on the river system. We have not used it in this data as it was no necessary, but before operationalising the system we would consider this step.

Another source of false alarms can be riverbanks, as shown in the Figure 2.19 heatmap. In principle, stable banks are not a source of false alarms as long as the reference image is taken in the summer, when the water level is expected to be lowest. This is one of the reasons why we decided to use a change detector approach. The banks will produce bright pixels in the reference; therefore, even if they appear again, they will be rejected by the change detector. The issue is when the banks change their location during different years. To solve this issue in our operational system, we plan two strategies: (a) the area affected by the riverbanks can be masked out (removed from the detection area) and (b) using InSAR, we can monitor the short-term stability of the area; if the bank persists over 6 days, it will have a high coherence and can be removed this way. Debris will not show high coherence since it floats and moves over the water.

The validation performed with this study has established that the accumulation of material is primarily composed of plastic waste; however, future work would need to be undertaken to understand the ability to discriminate between plastic waste with respect to other marine debris such as wood, metal, glass, etc.

2.6 CONCLUSIONS

This chapter has shown that plastic materials accumulated near dams appear visible in SAR imaging and can be monitored through radar remote sensing. The

backscattering differences in the accumulations and clean water have provided a basis for change detection algorithms to be implemented. Overall, the results indicate that change detection systems using SAR data can identify plastic accumulations near the River Drina Dam and Potpecko Lake Dam, with the accuracies from the best detector, the Optimisation of Power Difference (dif1), varying from 85–95% depending on rate of false alarms. The results also indicate that detectors that can utilise the coherent data from the SLC data are perform better when compared with those that do not utilise this information. We also find that the cross-pol VH channel also provides better detection than those based on single-pol VV polarisation. From the use of the most powerful detector, we have also created heatmaps that can be used to aid future management practices within the river system, with debris entrapment and/or inflows being particularly highlighted. These can be used to target control measures within the systems.

Chapter 3: Investigating the Backscatter of Marine Plastic Litter Using a C- and X-band Ground Radar, during a Measurement Campaign in Deltares

This chapter provides the results of two rigorous measurement campaigns, where the use of a C- and X-band radar was exploited to understand the capabilities of monitoring marine plastics. Multiple experiments were undertaken within the Atlantic Basin, a large wave tank in the Deltares Facility, Delft, The Netherlands, which can simulate deep ocean waves.

Backscatter and statistical analysis is undertaken on every experiment conducted within our measurement campaigns. The results show that backscattering differences in the C- and X-band between the reference water (called here as "clean") and the test water filled with plastic can be detected in some conditions. Overall, the results indicate that the X-band frequency performs significantly better than the C-band frequency, with X-band detecting significant differences in backscattering in 48/68 test cases compared with C-band detecting differences in 20/67 test cases. We also find that the difference in backscattering is depending on the size and shape of the plastic object, as well as the wave conditions which the plastic is moving on. This study provides new insights on the radar capabilities for detecting marine plastic litter and new information which can be used in the planning of future missions and studies on the remote sensing of marine plastic pollution.

3.1 INTRODUCTION

Accumulations of plastic pollution are not well mapped globally (Martinez-Vicente, et al., 2019). There are an estimated 4.8–12.7 million metric tons of plastic that enter the ocean from land annually (Jambeck, et al., 2015). The presence of plastic in marine environments is of great concern, with at least 690 species worldwide being negatively affected by the presence of marine plastic pollution (Gall & Thompson, 2015). Animal species are both at risk of ingestion and entanglement with plastic

pollution (Derraik, 2002). However, it is not only the marine species that are at risk from marine plastic pollution; there are multiple documented human health issues that are associated with plastics, including food safety and security (Barboza, et al., 2018), and health issues stemming from toxic by-products of plastics, such as cancer, respiratory disease, cardiovascular disease, and more (Yusuf, et al., 2022). Although plastics' transportation within the ocean is beginning to gain some understanding, some models can differ by more than a factor of 100 (Van Sebille, et al., 2015). Measurements of marine plastics have traditionally been performed in situ; however, complications can arise from budget, spatial, and accessibility issues.

There are an estimated 21,000 (Law, et al., 2014)–79,000 (Lebreton, et al., 2018) tonnes of floating plastic inside the Great Pacific Garbage Patch alone, with over three-quarters of the garbage patch carrying debris that is larger than 5 cm (Lebreton, et al., 2018). Due to the known presence of surface plastics, remote sensing has been explored as a means of monitoring plastic pollution due to its effective history of being used for observing other ocean surface processes and phenomena (Goddijn-Murphy & Williamson, 2019). At present, most research on the detection of plastic pollution has been undertaken with the use of spectral imaging. This includes work in visible (Topouzelis, et al., 2019), short-wave infrared (Garaba, et al., 2018), and near-infrared (Hu, 2021) parts of the electromagnetic spectrum. These optical studies have employed in situ, unmanned aerial vehicle (UAV) and satellite imagery (primarily with Sentinel-2). Reviews of the current literature have shown that the remote sensing of marine plastics can be improved through the use of different sensing technologies and methods to complement each other (Maximenko, et al., 2019).

SAR is an active microwave imaging method capable of providing high-resolution monitoring of day-and-night imaging in nearly all weather conditions. SAR datasets have been used to measure physical properties of the Earth's surface, such as glaciers, vegetation properties, topographies, and natural hazards, but are also extensively used in the monitoring of ocean environments (Bamler & Hartl, 1998; Alpers, et al., 1981). The use of SAR has previously been used to detect biogenic films (Chatziantoniou, et al., 2021) and oil slicks (Naz, et al., 2020), as well as targets such as derelict fishing gear and larger items (Martinez-Vicente, et al., 2019). However, the interactions of the marine debris with the background ocean can make exploitation with SAR challenging (Martinez-Vicente, et al., 2019). The use of SAR for monitoring

small marine debris with SAR is largely understudied and not well understood. While there is some very recent research into radar's capabilities for detecting and monitoring marine plastic debris (Martinez-Vicente, et al., 2019; Topouzelis, et al., 2019; Maximenko, et al., 2019; Serafino & Bianco, 2021; Salgado-Hernanz, et al., 2021), the way that backscatter interacts with differing plastic items is largely unknown. The use of satellite bands is also less known. The lack of research is even more evident when we consider the backscattering of small plastic debris in water. Sensor sensitivity, configuration, and optimisation need to be considered in the future to fully understand SAR's capabilities.

This paper describes the theory and capabilities of radars operating on C- and X-band in observing floating plastic pollution in differing conditions through a series of measurement campaigns conducted in a lab setting. In this work, we address the following research questions:

1. Does marine plastic pollution produce a change in backscattering in radar imagery at C- and X-band wavelengths when compared to the same conditions without plastic?
2. What are the conditions that make this change statistically significant and what are the minimum quantities that we can observe?

The novelty of this study resides in the experiments carried out and the findings coming from the statistical analysis of those datasets. We show that radar backscatter differs between the reference and test conditions in multiple lab settings (wave conditions, plastic items, plastic concentrations) and that plastic pollution is potentially detectable in both C-band and X-band wavelengths, provided we have a reliable reference backscattering for the clean conditions. We also show the detection thresholds for specific plastic item concentrations in differing wave conditions.

The overall aim of this research is to find out if Synthetic Aperture Radar satellite data could be used to discriminate areas of large accumulations of floating plastics. There are already evidences of this, such as in Simpson, et al., 2022 (Chapter 1), and these experiments try to shed a light on the understanding of backscattering from plastic in water, using different plastic items, concentrations, and conditions.

3.2 MATERIALS AND METHODS

3.2.1 Deltares Experiment: Lab Conditions and Ocean Wave Spectra

In total, 2 3-week measurement campaigns were undertaken as part of the European Space Agency's Open Space Innovation Platform programme on the remote sensing of plastic marine litter between 4th October 2021 and 4th February 2022 at the Deltares Atlantic Basin test facility in Delft, The Netherlands. The Atlantic Basin is a large flume, 8.7-m wide and 75 m long, that is capable of generating both waves and currents, as seen in Figure 3.1.

Figure 3.1 Atlantic Basin (i.e., Deltares' wide wave-current flume), looking from the wave spending beach towards the test section in the middle of the basin and the wave paddles at the end of the basin.

The difference between the deep water wave conditions and shallow water wave conditions can be represented by the wavenumber (k) times the water depth (d). This value reaches infinity (kd -> ∞) for deep water wave conditions, while it approximates to zero for shallow water waves.

Throughout the measurement campaigns, the gravity wave conditions were varied during multiple tests. To incorporate representative test conditions for the plastics, deep water wave conditions were selected. A wave period (Tp) of 1.2 s and a water depth of 1 m were used, which created a kd factor of 2.8, which is acceptable for simulating deep water wave conditions. As the waves generated in the test facility

are limited by the water depth, wave steepness, and acceleration of the wave paddle, it was not possible to increase the kd factor even further.

Tests were carried out for both regular and irregular wave conditions, where the regular waves have almost identical wave heights. In Table 1, the wave height and wave period of both the regular and irregular wave conditions are shown. The wave height for the irregular wave conditions represents the significant wave height (Hs: the average of the highest 1/3rd of the waves). This means that the individual waves occurring in the wave spectrum can have larger wave heights than the values reported in Table 3.1. Irregular waves are important to test and were the main focus of testing, as the natural seaway on the oceans is irregular, where the sea rarely shows a unidirectional, regular sinusoidal wave pattern. Instead, we observed mixtures of different wave lengths, heights, and directions (Maritime Engineering Reference Book, 2008).

Table 3.1 Wave conditions used in the testing campaign for both regular (reg) and irregular (irreg) conditions. The ARC was switched off for higher irregular wave conditions due to limitations of the test facility.

Wave Conditions	Tp	Reg / Irreg : Hs	ARC		kd
	[s]	[m]	Reg.	Irreg.	[-]
Wave Condition 1	1.2	0.05	On	On	2.81
Wave Condition 2	1.2	0.09	On	On	2.81
Wave Condition 3	1.2	0.17	On	Off	2.81

The plastics were deployed near the wave paddle, and they drifted along the basin due to Stokes drift. The waves generated by the wave paddle were reflected on a permeable wall within the basin and from the end of the basin. The amount of wave reflection was calculated using three wave gauges positioned at fixed intermediate distances. With the measured wave signals at these wave gauges, the mean incoming waves and the mean reflected waves were determined by analysing the timeseries of the three wave gauges. The reflected wave height equalled about 10% of the incoming wave height. This reflected wave was absorbed again at the wave paddle by Active Reflection Compensation (ARC). In this way, the generated wave signal compensated for the reflected waves within the basin.

During the measurement period, the water level, wave height, current velocity, and flow rate were measured by the Deltares facility to ensure that all conditions were strictly met.

A full brief on the test conditions used within the Deltares facility can be found in de Fockert & Baker, (2022).

3.2.2 Plastic Used

In total, 21 different typologies of plastic items were used during the test campaigns, as can be seen in Appendix A (Table A1).

During the tests, different concentrations of plastics were used. These concentrations are presented in Table 3.2. During some tests, the concentrations were manually increased to reach a specific concentration in the area of interest. These cases are represented with multiple concentrations in Table 3.2.

Table 3.2 Applied concentrations in the test campaigns. Cx corresponds to different concentrations, i.e., plastic spheres were tested at 9 different concentrations (C01–C09).

Plastic ID	Concentration (g/m2)								
	C01	C02	C03	C04	C05	C06	C07	C08	C09
Plastic Bottles	40	20	18.4	10	4.6				
Fixed Plastic Nets	11.25								
Plastic Bottles + Fixed Plastic Nets	83.3								
Plastic Straws	10								
Plastic Food Wraps and Bags (Marine Litter)	2.3	4.6	8.3						
Plastic Nets (Marine Litter)	10								
Plastic Nets and Bottles (Marine Litter)	8.3								
Plastic Bottles without Caps / Filled with Water	4.6	18.4							
Plastic Pellets	20								
Styrofoam	10								
Plastic Caps and Lids	10								
Cigarette Filters	10								
Plastic Cutlery	14								
Plastic Spheres	2	4	6.4	10	20	40	80	120	153

EVA Cylindrical Foam	10
Transparent Plastic Lids	10
Transparent Plastic Lids without Edges	10

3.2.3 Test Procedures

Reference measurements were taken to test the capability of floating plastic to change the backscattering of radar. The reference measurements consisted of defined wave conditions within the tank, but with no plastic items in the water. The test measurements consisted of the exact same wave conditions, but with the plastics added into the water.

During the first measurement campaign, reference measurements were taken of all wave cases in a day. These were then used as the references that all test measurements were compared against for their respective wave heights. During the second measurement campaign, a test protocol was established to ensure reference measurements and test measurements could be taken within each experiment at the shortest possible distance in time (i.e., references for each test were taken within 40 min before the test acquisitions began).

The plastic spheres were released into the basin through an automated manner by a sphere dispenser. This dispenser released the spheres at a fixed interval with a specific dispenser seed. In this way, the required concentrations could be controlled more accurately.

Except for the plastic spheres, all other plastics were manually distributed in the test facility. Prior to each test, the total amount of added plastic was carefully weighed, and this amount was constantly fed into the Atlantic Basin from the wave pedal located 16.7 m behind the measurement set-ups. This created a homogenous spread of plastic concentration throughout the different measurement areas.

At the end of each test, the particles were removed from the basin to ensure no contamination of plastics were present between the tests and references.

The first measurement campaign conducted in October 2021 consisted of a variety of tests on different types of plastics and wave conditions to understand the initial capabilities of the radar set-up. From these results, the second measurement

campaign conducted between January and February 2022 had more focussed testing on fewer wave conditions and plastics.

3.2.4 Measurement Equipment Set-Up

The measuring equipment consisted of a ground-radar, where the back end is an Anritsu Site Master S820e Vector Network Analyser. It is connected to C- and X-band antennas. The specifications of the hardware can be seen in Table 3.3. A solid-state switch was used to perform the quad polarimetric acquisitions using the single input and output ports of the VNA. Semi-rigid cables (DC to 18 GHz) were strapped in position to minimise the changes between the acquisition days.

Table 3.3 Measuring equipment specifications for ground radar used to measure Deltares campaign experiments.

Equipment	Frequency Range	Polarisation	3dB Beamwidth	Dynamic Range
Anritsu Site Master S820e VNA	1 MHz - 14 GHz	-	-	110 dB from 20 MHz to 14 GHz
C-Band Antenna	5 - 6 GHz	Quad-pol	25°(H)/15°(E)	-
X-Band Antenna	8.2 - 12.4 GHz	Single VV Pol	16°(H)/14°(E)	-

The radar equipment was located on the bridge that crossed the middle of the Atlantic Basin. The C-band antenna (Figure 3.2 A) was located 4.04 m above the floor of the basin and the X-band antenna (Figure 3.2 B) was located 3.61 m above the floor of the basin. An external sphere used as a target for calibrating the polarimetric behaviour (further details in Image Formation) was located 2.5 m in front of the radar. The radar was looking downstream with an incidence ranging between 30° and 50°. For both frequencies, the 3 dB main lobe formed a footprint in cross-range that was approximately 2 m. The sweeps in frequency considered 1 GHz (for each band), which resulted in a theoretical range resolution of 15 cm.

Figure 3.2 Measurement set-up located inside the Atlantic Basin Wave Facility. (A,C)-band antenna; (B) X-band antenna; (C) external sphere used for calibration. (D) Additional wave gauges that were removed during measurement campaign testing.

3.2.5 Image Formation

The radar architecture is a Step Frequency Continuous Waveform (SFCW), where the transmitting wave was sweeping as a linear frequency modulation in a desired bandwidth. The received signal was then processed including a Hamming window and inverse Fourier transform to focus the range profile. Each VNA sweep, therefore, produced a single range profile. The C-band antennas considered a sweep between 5 GHz and 6 GHz, while the X-band antennas considered a sweep between 9.5 GHz and 10.5 GHz. These frequency ranges were chosen to be inclusive of the bandwidths used by SAR satellites. The radar parameters were set so that the range of ambiguity was 80 m. This was to ensure that returns from the back of the 75 m tank were not overlapping with our test area due to ghosts (please note that the bridge with the radar was around the middle of the tank).

Each experiment consisted of monitoring a type and concentration of plastic (or the reference for this). In each experiment, we acquired several repetitions in time. This means that each acquisition considered multiple sweeps over the course of the experiment. The minimum number of sweeps used was 80 and the maximum was 580, and this duration depended on factors such as the permanency of plastic in the radar beam and the amount of plastic available for the experiment.

The calibration was conducted keeping in mind two main goals: (a) backscattering stability and (b) radiometric accuracy. It is known that VNA signal generators may drift in amplitude and phase during a measurement campaign since they may be dependent on temperature and humidity, as well as other factors (Bystrov, et al., 2022). The fact that references were taken up to forty minutes before the tests should not lead to large drifts in the temperature and humidity, and, therefore, should not lead to drifts in the VNA. However, calibration was still necessary to more easily compare the results between the different acquisition days, and to create reassurance that any potential drift was mitigated. For this reason, we identified a permanent target inside our radar profile and used this as a reference to clip all of the radar profiles (for a given frequency and polarisation) together. The permanent "target" for the C-band experiment was the antenna leak between the transmitter and receiver. The target for the X-band experiments was a reflection from the bridge straight below the antennas. Since the radar geometry was fixed over the entire campaign, these two returns showed a remarkable stability.

In order to calibrate the polarimetric behaviour and to provide a measure that could be exported to other experiments, we wanted to calibrate the profile radiometrically over a canonical target. An external 30 cm metal sphere was used to further convert the clipped images into radar cross sections. The sphere did not have any impact on clipping the same polarisation channel since the radiometric calibration was a range independent factor given a band and a polarisation channel. It, however, affected the weight when comparing the frequencies and polarisations channels.

3.2.6 Scattering Model Hypothesis for Marine Plastics

In this section, we introduce the scattering model that we hypothesise for plastic in water.

We hypothesise three different scattering mechanisms that could contribute to the total scattering coming from plastic in water: Direct, Indentation, and Wave-Generation. We assume that these are all present, but their contribution may be very different when, in some conditions, one can strongly dominate over the others.

Scattering is strongly dictated by the dielectric constant, together with other factors including roughness, shape, and size. The real part of the dielectric constant is related to the amount of power of the induced current on the object and, therefore, the

amount of scattering. For plastic, the relative dielectric constant is relatively small (proximal to one, the one of air). Therefore, we do not expect plastic to scatter directly. However, when water is included in the scene there are different phenomena that can be triggered and we hypothesise three mechanisms that can provide an increased backscattering compared to clean water, as seen in Figure 3.3.

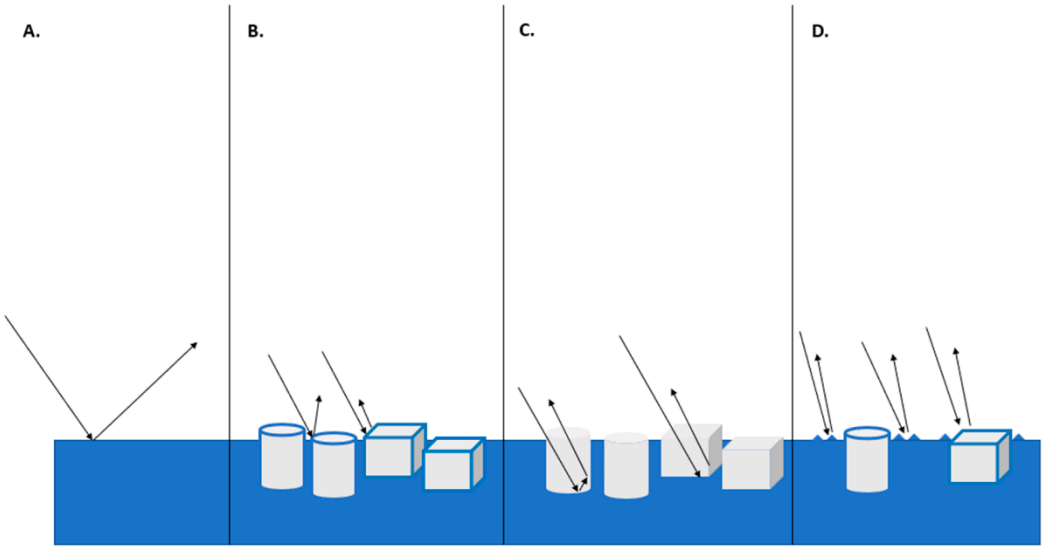

Figure 3.3 Radar backscatter interacting in different scenes. Black arrows: Radar signal and backscattering. (A) Specular reflection of signal from calm water with no material inside water. (B) 'Direct' scattering is a change in backscatter from 'wet' plastics that are partially submerged with a thin layer of water on top. (C) 'Indentation' scattering is a change in backscatter from 'dry' plastics that are partially submerged with no layer of water on top but are producing indentations in the water. (D) 'Wave-Generation' scattering is a change in backscatter from the addition of capillary waves generated from the presence of plastic items interacting with waves.

Water with no plastic has a smooth surface, calling for specular reflection of the signal. This can be easily demonstrated looking at SAR images since those areas appear as dark.

Whether or not the radar waves penetrate any medium is controlled by the imaginary part of the dielectric constant of the particular medium. A medium with a high imaginary part of the dielectric constant, such as water, is mostly impenetrable (mm or cm penetration depth depending on several factors, including frequency and salinity). Therefore, when a thin layer of liquid water is on top of the plastic, it creates a change in the surface roughness due to the raised 'bumps' of liquid water. The backscattering from these "bumps" should be increased due to the fact that water also has a high real part of the dielectric constant. Here, we call this 'direct scattering'. The thickness of the liquid water layer can be very small, with just 1 mm being potentially sufficient, as shown by observations of wet ice, snow, or icebergs (Marino, et al., 2016;

Cumming , 1952; Abe, et al., 1990). On the other hand, when the imaginary part of the dielectric constant is low, the medium can be penetrated easily without loss, as is the case for plastic. The plastic, therefore, is penetrated; however, it is still producing an effect on the water underneath by producing indentations and extra roughness, which we call 'indentation scattering'. This extra roughness induces a scattering from the surface (as if extra capillary waves were present).

While the figure above is an example on still water, the physical mechanisms remain the same in moving water. Finally, another mechanism was also observed during testing, where capillary waves were generated from plastic items interacting with moving water throughout every test. Different items produced differing disturbances on the water surface, but all plastic items generated amounts of capillary waves on the water surface as the waves crashed on them. This is an interesting observation as radar is sensitive to the surface roughness and differences in the capillary wave generation can potentially be detected. Here, we call this 'wave-generation' scattering.

To summarise, these three scattering mechanisms can all be present at the same time, although we expect that one will dominate over the others depending on the frequency used, size of plastic, buoyancy, waves, wind, rain, and other factors.

3.2.7 Radar Data Analysis

The analysis we performed focussed on the signal intensity (or backscattering). The intensity (in dB scale) was taken from all focussed and calibrated acquisitions during the run of each experiment (Reference or Test).

The following information is displayed in two main ways for each experiment. First, the mean of the intensity (dB) was evaluated by averaging all of the repetitions. This trend was plotted against the distance (m), allowing us to average out the signal variation due to speckle. Second, images were created where the two dimensions represent the distance from the radar (no. of pixels) vs. time (no. of acquisitions taken). The image colour represents the intensity on a linear scale. These images are often referred to as radargrams (e.g., when dealing with ground-penetrating radars). Although radargrams are affected by speckle, they contribute to the qualitative understanding of the experiments from each measurement session. They also help to

gain insights into the time dynamics of the backscattering, which helps the interpretation.

The visualisation itself is a good way to qualitatively compare backscattering differences between the test (waves and plastic) and reference (same waves/no plastic) experiments.

To create a quantitative insight into the data, a statistical analysis was undertaken. Each test measurement underwent a statistical analysis. Starting from the radar profile, we identified the ROI representing water in the tank where plastic would drift through. The pixels in that area were averaged over time to obtain a single mean value for the ROI. This mean value was then compared against the same ROI during the reference acquisition, which considered the same wave conditions but with no plastic presence.

We applied our statistical test for:

Null Hypothesis H0: No change in the mean backscattering

Alternative Hypothesis H1: Change in the mean backscattering

Using the Central Limit Theorem (CLT), we assumed the distributions of the differences of the sample means approximated a normal distribution. All sample sizes were greater than 80 (the minimum requirement considered sufficient for the CLT to hold is often stated as 30).

The threshold for H1 (i.e., confidence interval) can, therefore, be set using a Neyman-Pearson-derived constant false alarm rate (CFAR) methodology which only required the knowledge of the mean and standard deviation (Kay, 1998). The threshold was set as: difference of the mean > 3 * standard deviation. This threshold led to a confidence interval of 99.7%, and since this is a one-trail test, the corresponding false alarm rate was around 0.15%. This confidence interval was subject to the assumption of normal differences.

This statistical analysis was applied to all experiment cases that were undertaken over the test campaigns. From this, tables were then created showing if the statistical differences were or were not found in all of the experiments that were undertaken.

When dealing with SAR images, one traditional processing step is speckle filtering. This can be easily conducted using a boxcar filter. When we analyse the data

as described above, this could be compared to using single-look complex (SLC) Synthetic Aperture Radar (SAR) data. However, when applying a boxcar, this could be compared to using Ground Range Detected (GRD) SAR data (as provided by the ESA Sentinel-1 satellite), where multi-looking is present. The boxcar filter was applied to time vs. distance radar imagery to reduce the noise present within the images. The boxcar reduces the overall variation present in an image by setting each pixel's intensity equal to the average of its neighbour. The boxcar filter we used for these acquisitions was 5 × 1 (Time × Space). This allowed us to not lose any range resolution during this process.

Applying the boxcar filter to the test reduces the standard deviation of the difference (test vs. reference) and, therefore, modifies the final threshold. This is equivalent to saying that the boxcar filter reduces the noise level in the image, so we can use a lower threshold to monitor the differences without impacting the false alarm rate.

We did not perform any coherent polarimetric analysis, since the moving of targets (waves and plastic) during the acquisitions resulted in decorrelating the polarimetric channels and, therefore, not allowing coherent polarimetric analysis (the covariance matrices are diagonal over the targets of interest). In the following, in C-band, the different polarimetric channels are compared using intensities only, in the same way that some satellite systems do no acquire polarimetric data coherently (e.g., some modes of COSMO-SkyMed or NOVASAR).

3.3 RESULTS

Multiple plastic items were used as free-floating targets in different experiments. In the first part of this section, we showed the results of plotting the backscatters in different test cases between the reference and experiment. For the sake of brevity, the graphs showed here only cover very limited selected cases, which can be used to demonstrate the trends. The second part of this section includes the statistical analysis that covers every single test we performed.

3.3.1 Free-Floating Targets: X-Band – Intensity Plots

The following line graphs show the X-band frequency results. All measurements were made between 9.5 GHz and 10.5 GHz frequency ranges in VV polarisation. The mean intensity was taken from all acquisitions during the experiment. The distance

was measured considering the VNA as the starting point. In the figure below, we see three experiments comparing test and reference acquisitions. We see a peak of intensity from the lip of the bridge, labelled ‘1.’ and a blue box labelled ‘2.’ which highlights our ROI within the wave tank, and, finally, a dashed line, which is used as an arbitrary reference line to aid visualisation.

In Figure 3.4, we see a comparison of the backscatter from the reference acquisitions with no plastic in the water and the test acquisitions with different plastics inside the water. Please note the stability of the reference point over the peak one. The mean over two bins was used to clip the images to avoid errors due to micromovements and fractional pixels. This is when the same target (the bridge edge) appeared as a fractional pixel over two bins. For A, an increase in intensity by 8.1 dB (around 6 times in linear) can be seen from the test acquisition, where the only change between the test and reference experiments was the addition of plastic bottles into the water. For B, an increase in intensity by 10.9 dB (around 15 times in linear) can be seen from the Test acquisition, where the only change between the test and reference experiments was the addition of cylinder foam into the water. In C, due to the increased height of the waves used in this experiment, in tandem with 17 cm waves having more breaking waves, we see an overall increase in backscattering from our reference when compared with the 9 cm waves references. We can also see an increase in intensity by 7.3 dB (around 4 times in linear) from the test acquisition, where the only change between the test and reference experiments was the addition of plastic lids into the water.

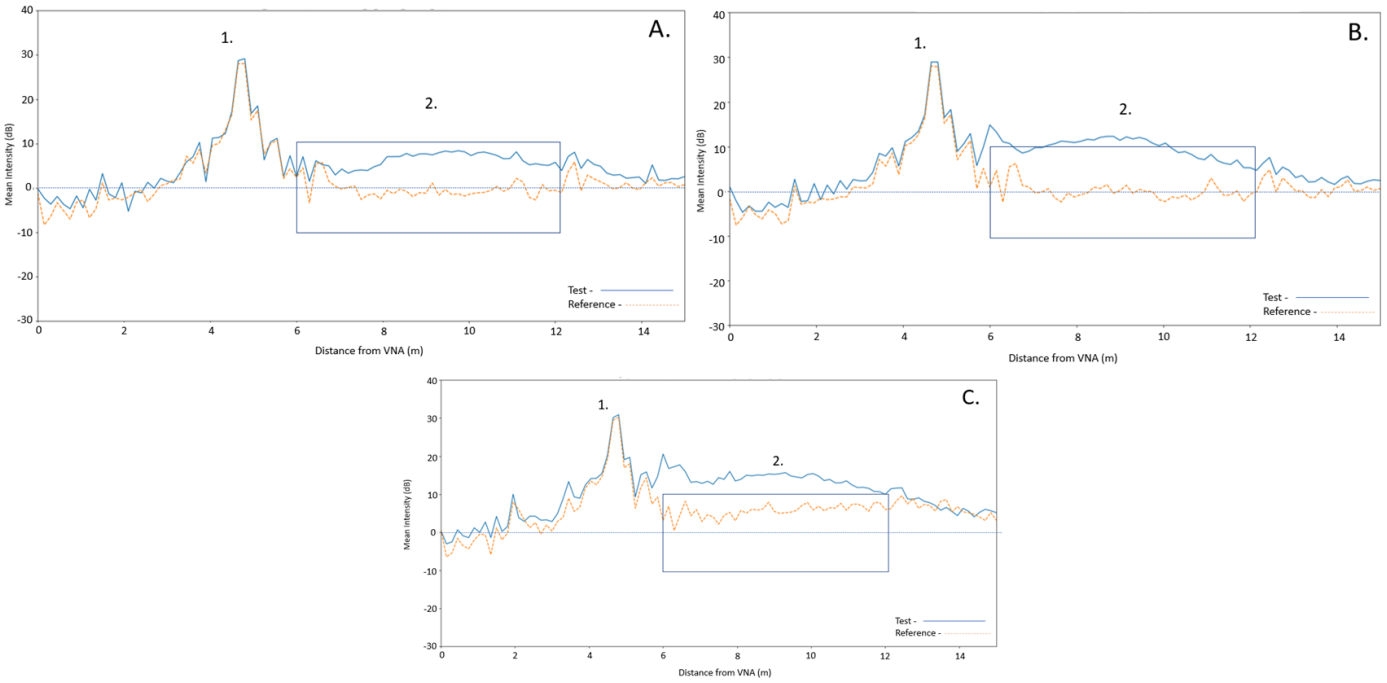

Figure 3.4 X-band intensity plots of irregular wave test and reference acquisitions. 1. Peak of intensity from the lip of the bridge by radar set-up. 2. ROI within wave tank (also highlighted by a blue box). Dashed line: arbitrary reference line to aid visualisation. (A) Nine centimetre irregular wave conditions for test and reference. Test = 40 g/m2 of plastic bottles inside of the tank (2 bottles/m2). (B) Nine centimetre irregular wave conditions for test and reference conditions. Test = 20 g/m2 of plastic foam cylinders (20 cm long) inside tank. (C) Seventeen centimetre irregular wave conditions for test and reference conditions. Test = 10 g/m2 of plastic lids inside tank (1.5 lids/m2).

To create a time series of this intensity data, radargrams were created. Within the figures, we highlighted the colour gradient showing the intensity on a linear scale. The black arrows on the figures highlighted a feature of interest. These figures are shown in the figure below.

In

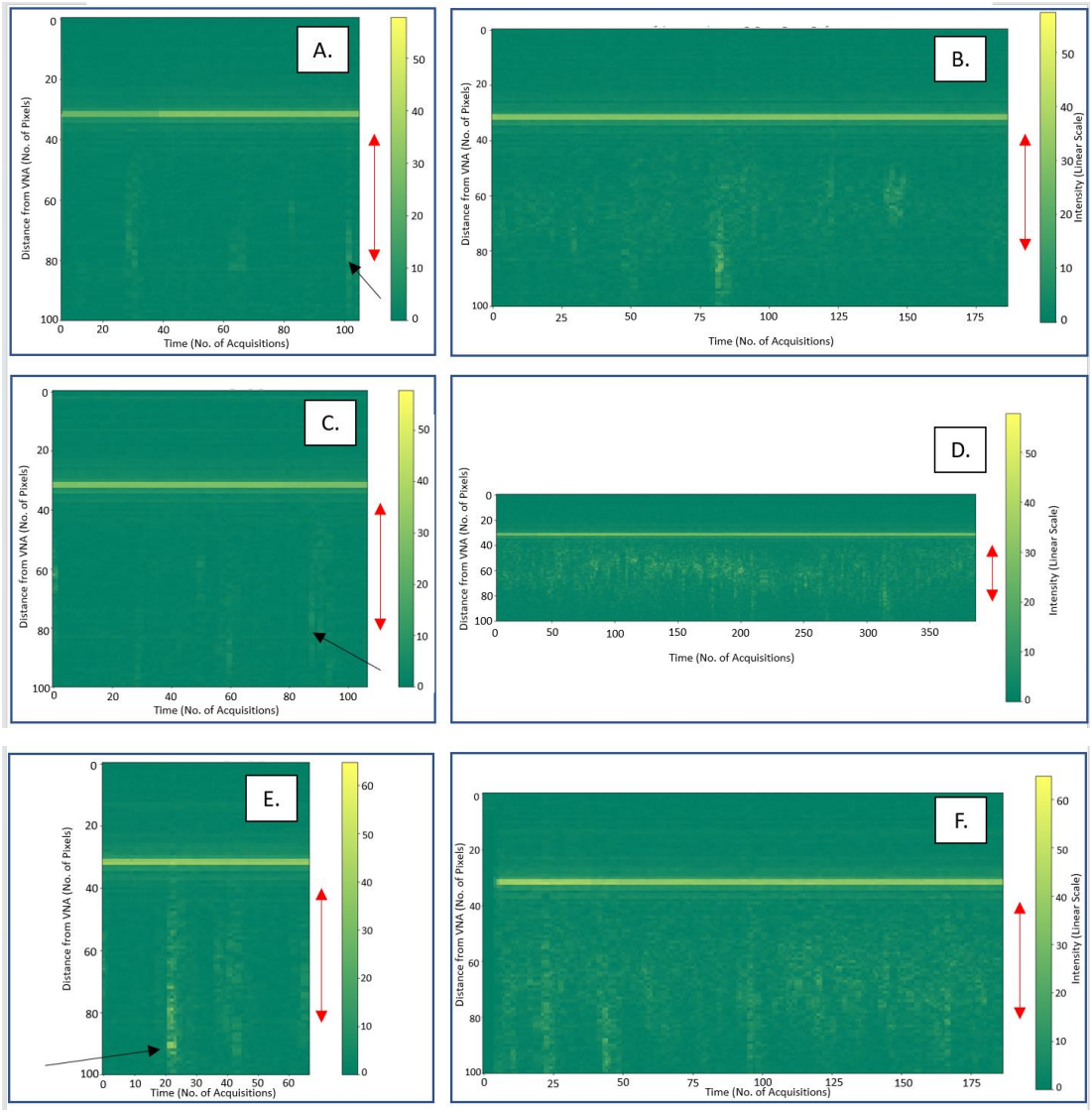

Figure 3.5, we see the radargram comparisons of the backscatter from the reference acquisitions with no plastic in the water and the test acquisitions with different plastic items moving through the water. The region that the radar can see is indicated by the red double arrow. However, we are not including all of this in our analysis since the incidence angle in that region outside the double arrow was very shallow, above 50°, and it is not suggested to use those regions to monitor plastic. Note that most satellites tend to not acquire incidence angles over 50° because these angles are too shallow for almost any Earth observation activity (Kaplan, et al., 2021); the SAR Satellite Sentinel-1 acquires with an incidence angle range of 29.1–46.0° (European Space Agency, N/A). Although we exclude them in the statistical analysis, it is interesting to observe how they can still show a qualitative difference between the presence and absence of plastic.

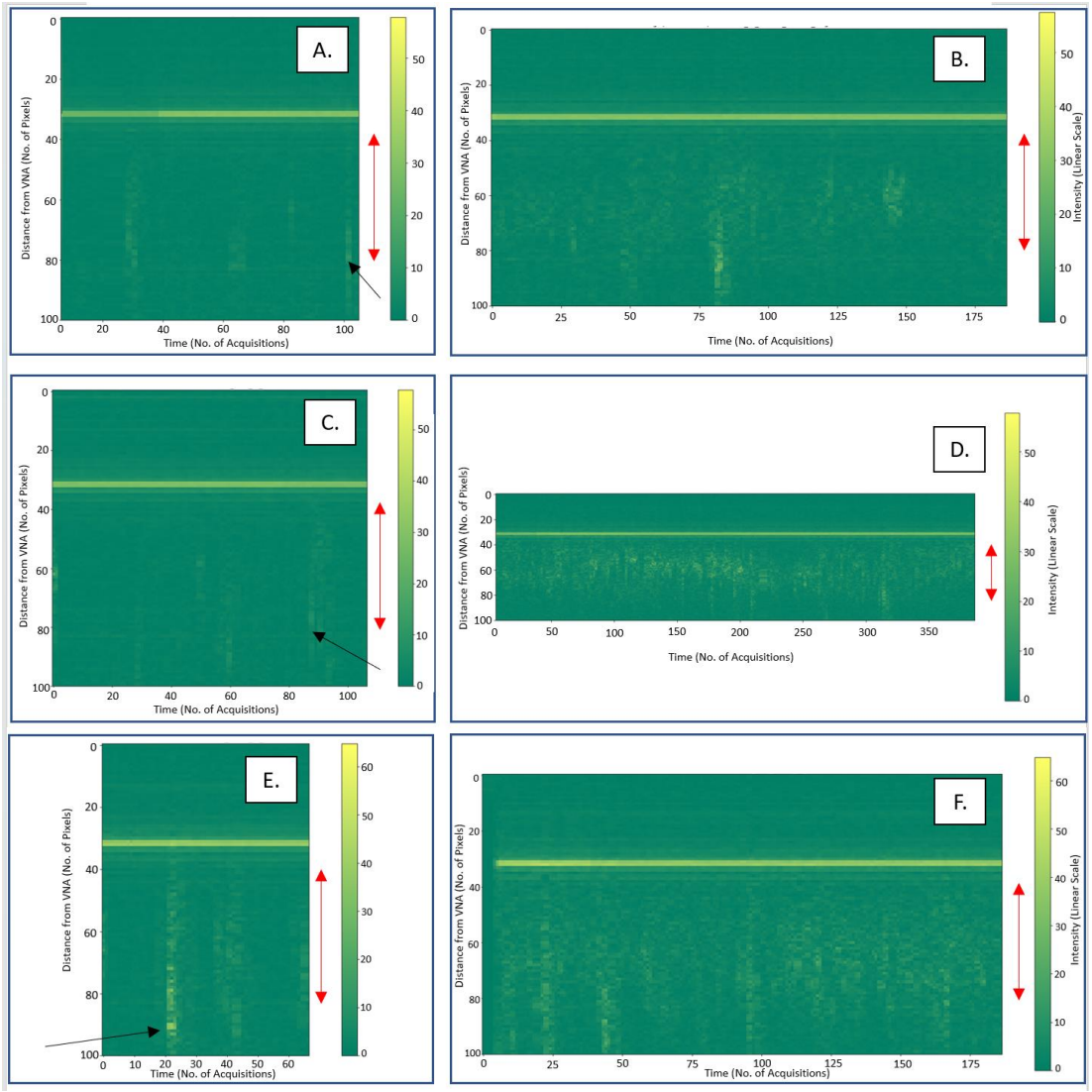

Figure 3.5 X-band intensity plots of irregular wave reference acquisitions (Left) and test acquisitions (Right). Nine centimetre irregular wave conditions for reference (A) and test (B) (Top). Test = 40 g/m2 of plastics bottles inside tank (2 bottles/m2) (Middle). Nine centimetre irregular wave conditions for reference (C) and test (D) conditions. Test = 20 g/m2 of plastic foam cylinders (20 cm long) inside tank (Bottom). Seventeen centimetre irregular wave conditions for reference (E,F) conditions. Test = 10 g/m2 of plastic inside tank (1.5 lids/m2). Peak on intensity from the lip of the bridge by radar set-up can be seen across all figures. Colour—Intensity on a linear scale. Black arrow indicates a feature of interest. Red double arrow indicates the region of interest for the radar.

A change in the intensity with plastic can be seen in the radargrams, with a more uniform layer of increased intensity seen from the test experiments with plastic items moving through the tank. Most of the scattering from plastic comes from the ROI, although we still see some increase even further away with very shallow incidence angles, but the difference is very evident when plastic is introduced.

We would also like to draw attention to the feature identified by the black arrows in

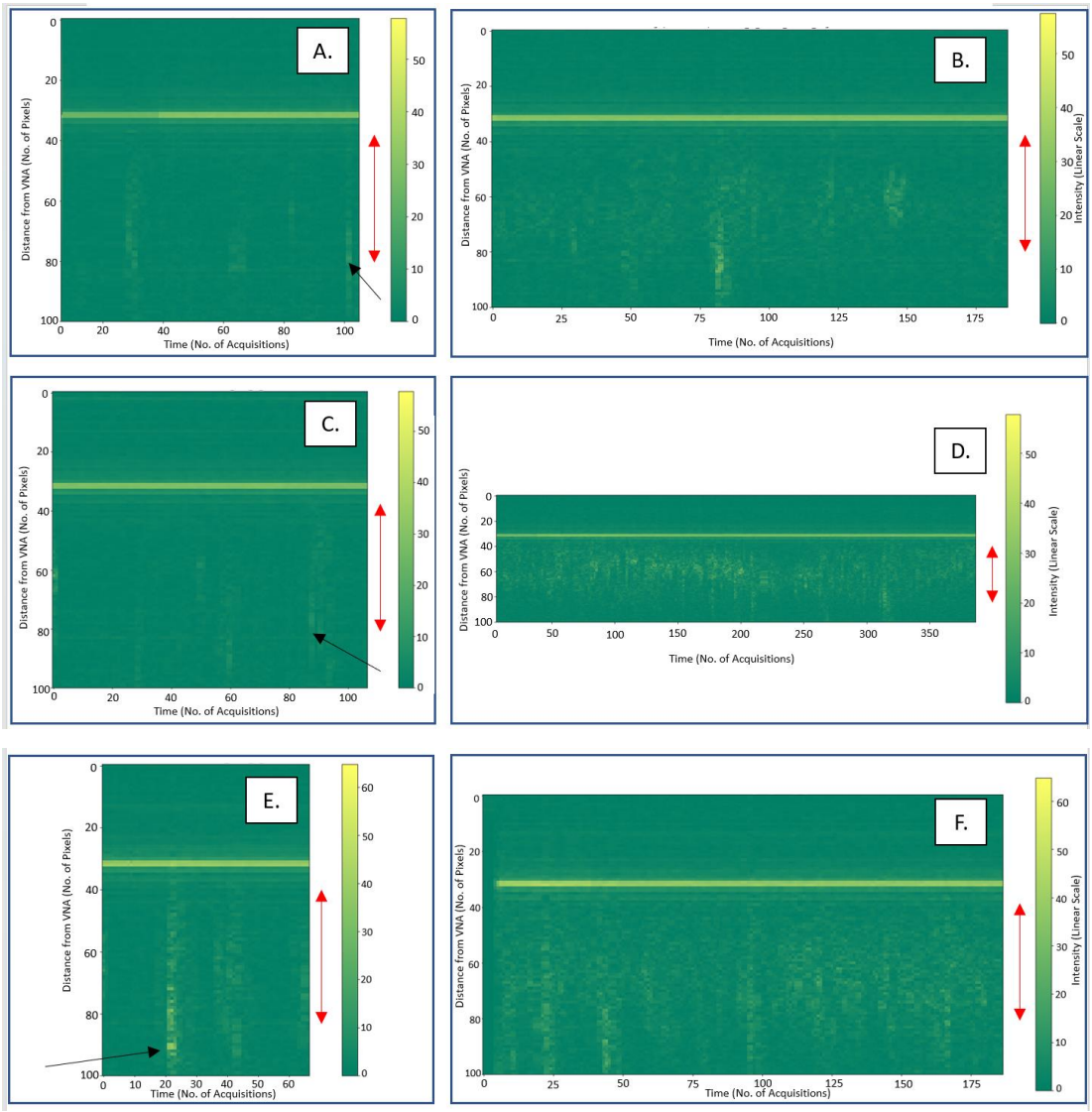

Figure 3.5. We see these features in other tests and comment on these later in the chapter.

3.3.2 Free-Floating Targets: C-Band – Intensity Plots

The following line graphs show the C-band frequency results obtained from the same setting as the X-band results. All measurements were made between the 5 GHz and 6 GHz frequency range in quad-polarisation (VV, VH, HV, HH), where H stands for linear horizontal and V stands for linear vertical. The mean intensity was taken from all acquisitions during the experiment. The distance was measured from the VNA as a starting point. We display the same tests as the X-band cases to serve consistency; however, for clarity we have separate graphs for reference and test acquisitions.

In Figure 3.6, we can see a comparison of the backscatter from the reference acquisitions with no plastic in the water and the test acquisitions with different plastic items moving through the water. An increase in intensity can be seen in all polarisations from the test acquisition. For A, these intensity increases were: 1.03 dB for VV, 1.68 dB for VH, 1.29 dB for HV, and 1.99 dB for HH. For B, the intensity increases were: 1.86 dB for VV, 2.51 dB for VH, 1.96 dB for HV, and 1.61 dB for HH. For C, the intensity increases were: 2.54 dB for VV, 3.69 dB for VH, 2.91 dB for HV, and 2.48 dB for HH. These increases are much smaller when compared with the differences in intensity found within the X-band experiments.

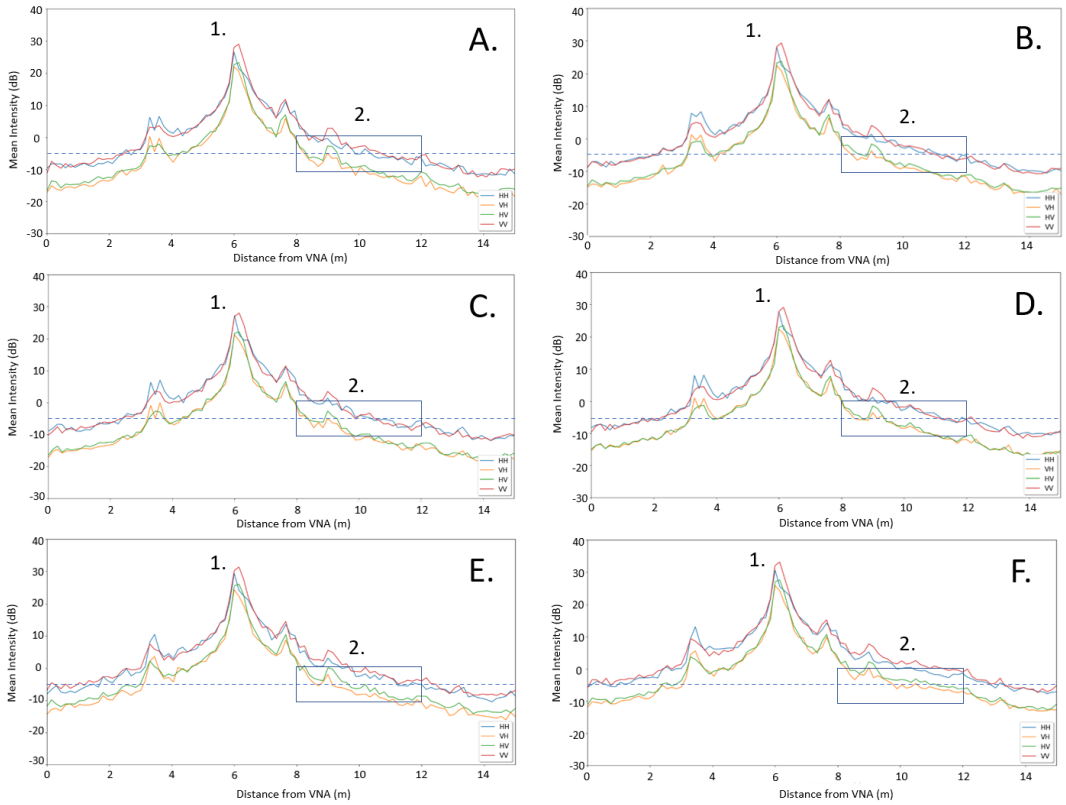

Figure 3.6 C-band intensity plots of irregular wave reference acquisitions (Left) and test acquisitions (Right). 1. Peak of intensity from the lip of the bridge by radar set-up. 2. ROI within wave tank (also highlighted by a blue box). Dashed: arbitrary reference line to aid visualisation (Top). Nine centimetre irregular wave conditions for reference (A) and test (B). Test = 40 g/m2 of plastic bottles inside tank (2 bottles/m2) (Middle). Nine centimetre irregular wave conditions for reference (C) and test (D) conditions. Test = 20 g/m2 of plastic foam cylinders (20 cm long) inside tank (Bottom). Seventeen centimetre irregular wave conditions for reference (E) and test (F) conditions. Test = 10 g/m2 of plastic lids inside tank (1.5 lids/m2).

Please note how the co-pol channels (HH and VV) were always higher than the cross-pol channels (HV and VH). Additionally, HV and VH were not identical due to

two reasons: the antennas beamwidths in the H and E plane were not identical and the noise levels were different in the two channels.

To create a time series of this intensity data, radiograms were created. These are shown below.

In Figure 3.7, we can see a comparison of the backscatter from the reference acquisitions with no plastic in the water and the test acquisitions with plastic moving through the water. It is difficult to see a distinctive change in the intensity over time in the radargrams when comparing the test acquisitions to their respective reference. However, there is a small difference evident in Figure 3.7 (C) where an increase in intensity can be seen from when the plastic lids were flowing through the tank.

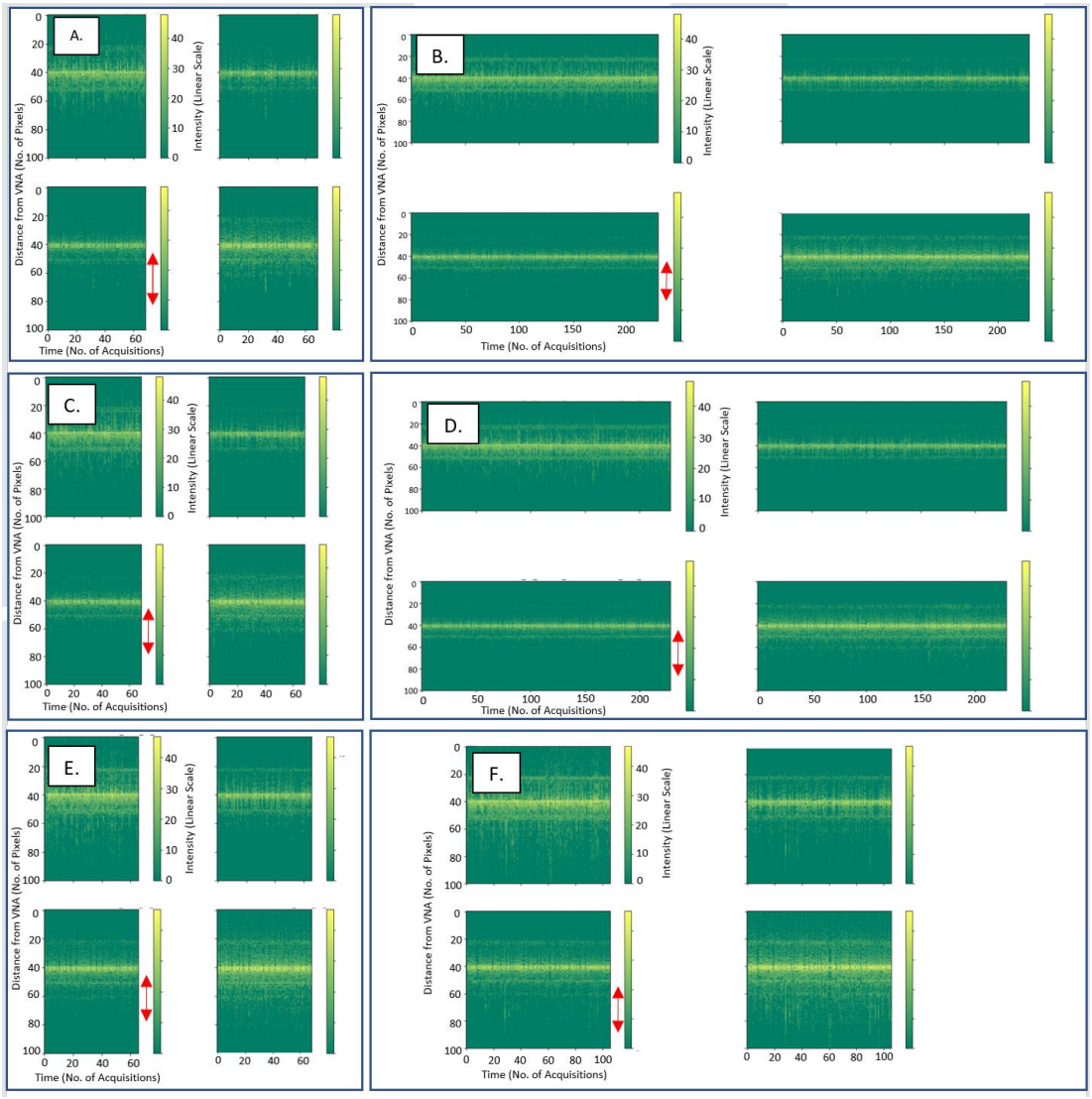

Figure 3.7C-band intensity plots of irregular wave reference acquisitions (Left) and test acquisitions (Right). Nine centimetre irregular wave conditions for reference (A) and test (B) (Top). Test = 40

g/m2 of plastic bottles inside tank (2 bottles/m2) (Middle). Nine centimetre irregular wave conditions for reference (C) and test (D) conditions. Test = 20 g/m2 of plastic foam cylinders (20 cm long) inside tank (Bottom). Seventeen centimetre irregular wave conditions for reference (E) and test (F) conditions. Test = 10 g/m2 of plastic lids inside tank (1.5 lids/m2). On each plot: (Top Left) HH Polarisation, (Top Right) VH Polarisation, (Bottom Left) HV Polarisation, (Bottom Right) VV Polarisation. Peak of intensity from the lip of the bridge by radar set-up can be seen across all figures. Colour—intensity on a linear Scale.

3.3.3 Statistical Analysis

We applied our statistical test for:

- Null Hypothesis H0: No change in the mean backscattering
- Alternative Hypothesis H1: Change in the mean backscattering

The results of the statistical analysis on each test were formatted into tables (as seen below). The results showed here use a confidence interval of 99.7% and a corresponding false alarm rate of around 0.15% as this is a one-trail test. For this testing, our hypotheses are as follows:

- Null Hypothesis H0: No change in the mean backscattering between the test and reference acquisitions.
- Alternative Hypothesis H1: A change in the mean backscattering between the test and reference acquisitions.

This testing was conducted on the data with and without the use of the boxcar filter.

3.3.4 Without Boxcar

The results from Table 3.4 indicate that statistically significant differences were found in only 2/29 cases between the test and reference acquisitions in the C-band data, in HH- polarization for plastic cutlery, and in VV-polarization for plastic sheets, both in 9 cm waves. A significant difference in this case meaning that the change in mean backscattering from the test was > 3 * the standard deviation of the reference acquisition, these are highlighted green in the table. A statistically significant difference was found in 7/29 cases between the test and reference acquisitions in the X-band data. It can be noted that three of the X-band measurements with a statistical difference involved the use of fixed position targets of plastic, making the detection of any differences much easier.

Table 3.4 Results of statistical analysis undertaken on 1st campaign measurements without the use of a boxcar filter. Values filling the table are the results of the difference of the reference measurement and test measurement in a linear format, with the p-value of the test in brackets. Any value in green shows that the alternative hypothesis was fulfilled; any value in orange shows that the null hypothesis was fulfilled.

Without Boxcar Filter								C Band					X-Band
Date	Objective	Wave Pattern	Hs [cm]	Plastics	Concentration [g/m^2]	No. of Acquisitions / Samples		HH	HV	VH	VV		VV
						C-Band	X-Band						
14/10/2021	Plastics at Fixed Position	No	0	Net	11.25	240	160	0.18 (0.44)	0.05 (0.44)	0.07 (0.45)	0.08 (0.44)		4.93 (0.19)
				Net + Bottles	83.3	120	200	0.6 (0.1)	0.33 (0.06)	0.38 (0.05)	0.48 (0.13)		13.3 (0.00)
		Irregular	9	Net	11.25	240	200	0.03 (0.46)	-0.02 (0.52)	0.02 (0.46)	-0.02 (0.52)		-4.71 (0.00)
				Net + Bottles	83.3	240	200	0.09 (0.42)	0.04 (0.44)	0.06 (0.4)	0.08 (0.43)		13.9 (0.00)
15/10/2021	Plastics at Fixed Position	Irregular	17	Net	11.25	240	320	0.02 (57)	0.04 (0.5)	0.05 (0.41)	0.03 (0.47)		-2.32 (0.97)
				Net + Bottles	83.3	240	200	0 (0.62)	0 (0.54)	0.04 (0.43)	0 (0.5)		9.65 (0.00)
18/10/2021	Variations in Free Flowing Plastics	Irregular	9	(New PET Bottles)	4.6	200	200	0.15 (0.35)	0.08 (0.4)	0.06 (0.45)	0.16 (0.4)		0.92 (0.56)
					40	160	200	0.17 (0.42)	0.08 (0.35)	0.08 (0.44)	0.17 (0.42)		6.36 (0.009)
				Organic Plastics (Sheets)	2.3	120	280	1.38 (0.1)	0.85 (0.21)	0.57 (0.3)	1.59 (0.024)		1.85 (0.06)

					4.6	80	200	1.39 (0.15)	0.88 (0.17)	0.8 (0.24)	1.84 (0.009)	4.21 (0.00)
19/10 /2021	Variations in Free Flowing Plastics	No	0	Pellets	20	200	200	1.6 (0.02)	0.88 (0.12)	0.82 (0.03)	1.69 (0.19)	0.87 (0.1)
		Irregular	0	(New) PET Bottles Partly Submerged	4.6	240	200	-0.04 (0.54)	0.01 (0.47)	0.01 (0.47)	0.04 (0.45)	-0.12 (0.96)
					40	240	160	0.04 (0.46)	0.01 (0.47)	0.02 (0.45)	0.03 (0.46)	-0.45 (0.96)
			9	Wrapped Fishing Nets / Ropes with Bottles	8.3	240	320	-0.02 (0.62)	-0.02 (0.66)	-0.02 (0.57)	-0.04 (0.65)	-1.86 (0.19)
				Partly Submerged Bottles	4.6	200	200	-0.15 (0.54)	-0.12 (0.61)	-0.04 (0.53)	-0.23 (0.59)	0.78 (0.1)
20/10 /2021	Variation in Wave Conditions	Irregular	5	Plastic Sheets and Bags	8.3	240	320	0.62 (0.14)	0.42 (0.14)	0.44 (0.07)	0.97 (0.053)	3.93 (0.03)
				Wrapped Fishing Nets / Ropes with Bottles	8.3	240	280	0.68 (0.12)	0.43 (0.06)	0.51 (0.03)	1.06 (0.013)	3.99 (0.023)
			9	Sheet Material	8.3	200	200	0.76 (0.06)	0.36 (0.14)	0.46 (0.07)	0.73 (0.053)	2.77 (0.015)
			17	Sheet Material	8.3	320	440	0.48 (0.26)	0.3 (0.19)	0.42 (0.06)	0.77 (0.1)	0.92 (0.1)
		Irregular and Capillary	17	Wrapped Fishing Nets / Ropes with Bottles	8.3	200	200	0.49 (0.25)	0.29 (0.2)	0.39 (0.08)	0.66 (0.14)	-2.38 (0.32)
				Sheet Material	8.3	160	160	0.27 (0.35)	0.23 (0.25)	0.27 (0.16)	0.58 (0.16)	-2.11 (0.22)
21/10 /2021	Capillary Waves		5	Sheet Material	8.3	160	320	0.64 (0.15)	0.31 (0.07)	0.42 (0.06)	0.77 (0.02)	0.22 (0.53)

		Irregular and Capillary		Nets / Ropes	8.3	160	160	0.68 (0.18)	0.43 (0.08)	0.5 (0.07)	1.06 (0.05)		3.9 (0.22)
			9	Sheet Material	8.3	200	240	-0.02 (0.52)	-0.02 (0.53)	0 (0.5)	-0.05 (0.54)		3.84 (0.15)
				Nets/Ropes with Bottles	8.3	200	240	-0.03 (0.54)	-0.05 (0.45)	-0.07 (0.49)	-1.74 (0.72)		-1.74 (0.87)
	Variations in Free Flowing Plastics	Irregular	9	Styrofoam	10	240	200	0.18 (0.35)	0.03 (0.46)	0.05 (0.41)	0.03 (0.47)		1.11 (0.24)
				Lids / Caps	10	320	200	0 (0.43)	-0.03 (0.55)	0.01 (0.47)	-0.1 (0.57)		0.31 (0.7)
				Cigarette Filters	10	200	200	0.09 (0.42)	-0.02 (0.53)	0 (0.5)	-0.05 (0.53)		-0.26 (0.46)
22/10 /2021	Variations in Free Flowing Plastics	Irregular	9	Cutlery	14	200	200	1.9 (0.007)	0.83 (0.24)	0.7 (0.47)	1.4 (0.06)		1.89 (0.01)

Table 3.5 Results of statistical analysis undertaken on 2nd campaign measurements without the use of a boxcar filter. Values filling the table are the results of the difference of the reference measurement and test measurement in a linear format, with the p-value of the test in brackets. Any value in green shows that the alternative hypothesis was fulfilled; any value in orange shows that the null hypothesis was fulfilled.

Without Boxcar Filter								C-Band					X-Band
Date	Objective	Wave Pattern	Hs [cm]	Plastics	Concentration [g/m2]	No. of Acquisitions / Samples		HH	HV	VH	VV		VV
						C-Band	X-Band						
26/01/ 2022	Free Floating Plastics	Irregular	9	Spheres [2cm] in Lines	6.4	240	280	-0.08 (0.57)	-0.04 (0.57)	-0.04 (0.56)	-0.08 (0.56)		1.14 (0.016)
					40	240	200	-0.09 (0.56)	-0.04 (0.56)	-0.03 (0.55)	-0.1 (0.58)		0.94 (0.07)
					80	240	200	-0.06 (0.65)	-0.02 (0.53)	-0.06 (0.59)	-0.1 (0.57)		1.05 (0.18)
					120	240	200	0.01 (0.48)	-0.01 (0.52)	0.08 (0.33)	0 (0.5)		1.18 (0.16)
					153	240	200	-0.12 (0.61)	0 (0.49)	-0.01 (0.5)	0.04 (0.5)		1.23 (0.25)
27/01/ 2022	Free Floating Plastics	Irregular	9	Spheres [2cm] with holes Taped	2	240	200	-0.02 (0.51)	0 (0.49)	0.04 (0.42)	0.04 (0.47)		0.19 (0.30)
					4	240	200	0.08 (0.43)	0.05 (0.42)	0.01 (0.48)	0.08 (0.44)		-0.09 (0.52)
					6.4	240	200	0.12 (0.38)	0.05 (0.41)	0.03 (0.45)	0.1 (0.41)		0.15 (0.45)
					20	240	200	0.05 (0.46)	0.04 (0.42)	0.04 (0.43)	0.09 (0.41)		0.14 (0.45)
	Full 9cm Reference			No Plastic	0	240	200	0.13 (0.38)	0.03 (0.44)	0.05 (0.41)	0.11 (0.4)		0.37 (0.42)
28/01/ 2022	Free Floating Plastic	Irregular	9	Bottles	20	240	480	0.1 (0.39)	0.04 (0.45)	0.05 (0.43)	0.06 (0.45)		0.95 (0.17)

				Bottles	40	240	200	0.12 (0.39)	0.06 (0.39)	0.04 (0.43)	0.11 (0.4)		0.94 (0.31)
				Straws (24cm)	20	240	400	0.1 (0.38)	0.05 (0.42)	0.05 (0.4)	0.06 (0.44)		4.06 (0.013)
				Cylinder Foam (20cm)	20	240	400	0.12 (0.33)	0.07 (0.28)	0.09 (0.25)	0.14 (0.31)		2.68 (0.04)
				Cylinder Foam (10cm)	20	240	400	0.19 (0.4)	0.1 (0.41)	0.13 (0.36)	0.18 (0.4)		1.94 (0.03)
31/01/ 2022	Free Floating Plastic	Irregular	9	Cylinder Foam (5cm)	20	240	280	0.12 (0.37)	0.02 (0.45)	0.03 (0.44)	0.08 (0.51)		2.17 (0.03)
				Straws (12cm)	20	240	280	-0.01 (0.51))	0.01 (0.48)	0.01 (0.47)	-0.01 (0.51)		0.85 (0.31)
				Straws (6cm)	20	240	200	0.01 (0.48)	-0.01 (0.52)	0 (0.51)	-0.04 (0.53)		0.18 (0.4)
01/02/ 2022	Free Floating Plastic	Irregular	9	Spheres [2cm] with holes Taped	10	240	200	0.2 (0.36)	0.06 (0.45)	0.08 (0.45)	0.1 (0.48)		0.49 (0.22)
			17		10	240	200	0.14 (0.36)	0.05 (0.4)	0.06 (0.41)	0.08 (0.41)		-0.12 (0.55)
					20	240	200	0.11 (0.43)	0.04 (0.46)	0.08 (0.41)	0.14 (0.42)		0.19 (0.42)
					40	240	200	0.2 (0.32)	0.11 (0.33)	0.07 (0.38)	0.17 (0.36)		-0.03 (0.51)
02/02/ 2022	Free Floating Plastic	Irregular	5	Spheres	10	240	200	0.2 (0.51)	0.09 (0.4)	0.05 (0.37)	0.17 (0.35)		0.26 (0.31)
					20	240	200	0.02 (0.33)	0.06 (0.4)	0.1 (0.44)	0.19 (0.4)		0.53 (0.17)
					40	240	200	0.17 (0.38)	0.1 (0.38)	0.06 (0.42)	0.21 (0.36)		0.35 (0.32)
				Plastic Lids	10	240	200	0.38 (0.23)	0.29 (0.13)	0.25 (0.18)	0.53 (0.15)		3.38 (0.00)

			9			240	200	0.02 (0.48)	0.01 (0.48)	0.08 (0.39)	0.06 (0.46)		2.18 (0.06)
			17			240	200	0.27 (0.39)	0.27 (0.26)	0.16 (0.38)	0.45 (0.34)		2.79 (0.13)
03/02/ 2022	Free Floating Plastic	Irregular	5	Bottles	20	240	200	0.17 (0.33)	0.1 (0.28)	0.08 (0.35)	0.21 (0.27)		1.38 (0.2)
						-	200	-	-	-	-		1.38 (0.2)
	Full 5cm Reference			No Plastic	0	240	200	0.1 (0.44)	0.04 (0.5)	0.06 (0.48)	0.09 (0.51)		0.32 (0.48)
	Free Floating Plastic		9	Bottles	20	240	200	0.02 (0.37)	0 (0.4)	0.01 (0.43)	0.07 (0.41)		1.07 (0.35)
			17			240	200	0.02 (0.42)	0.01 (0.37)	-0.01 (0.45)	0 (0.36)		-0.03 (0.55)
	Full 17cm Reference			No Plastic	0	240	200	0.02 (0.43)	-0.03 (0.48)	-0.02 (0.43)	-0.06 (0.46)		-0.5 (0.66)
04/02/ 2022	Free Floating Plastic	Irregular	9	Bubble Wrap	1m Long Strip	-	200	-	-	-	-		1.63 (0.18)
				Plastic Lids (No Edges)	10	240	200	0.05 (0.45)	0.02 (0.46)	0.03 (0.45)	0.05 (0.46)		3.28 (0.07)
			17			240	200	0.06 (0.45)	-0.03 (0.52)	-0.04 (0.53)	-0.01 (0.5)		1.75 (0.14)

The results from Table 3.5 indicate that statistically significant differences were found in only 1/37 cases between the test and reference acquisitions. This was found in the X-band frequency: 5 cm wave height plastic lids (10 g/m2). The C-band acquisitions had no cases where a statistically significant difference was found between the test and reference acquisitions in any of the experiments. The experiments that were

undertaken to eliminate changes in the wave machines' production of waves also showed that there were no significant differences between the wave conditions during reference acquisitions when compared with test acquisitions.

3.3.5 With boxcar

Table 3.6 Results of statistical analysis Undertaken on 1st campaign measurements with the use of a boxcar filter. Values filling the table are the results of the difference of the reference measurement and test measurement in a linear format, with the p-value of the test in brackets. Any value in green shows that the alternative hypothesis was fulfilled; any value in orange shows that the null hypothesis was fulfilled.

With Boxcar Filter								C-Band				Xband
Date	Objective	Wave Pattern	Hs [cm]	Plastics	Concentration	No. of Acquisitions / Samples		HH	HV	VH	VV	VV
						C-Band	X-Band					
14/10 /2021	Plastics at Fixed Position	No	0	Net	11.25	240	160	0.18 (0.01)	0.05 (0.11)	0.07 (0.15)	0.08 (0.12)	4.93 (0.00)
				Net + Bottles	83.3	120	200	0.6 (0.00)	0.33 (0.00)	0.38 (0.00)	0.48 (0.00)	13.3 (0.00)
		Irregular	9	Net	11.25	240	200	0.03 (0.24)	-0.02 (64)	0.02 (0.22)	-0.02 (0.67)	-4.71 (0.00)
				Net + Bottles	83.3	240	200	0.09 (0.03)	0.04 (0.22)	0.06 (0.014)	0.08 (0.08)	13.9 (0.00)
15/10 /2021	Plastics at Fixed Position	Irregular	17	Net	11.25	240	320	0.02 (0.95)	0.04 (0.5)	0.05 (0.28)	0.03 (0.28)	-2.32 (0.88)
				Net + Bottles	83.3	240	200	0 (0.99)	0 (0.86)	0.04 (0.07)	0 (0.51)	9.65 (0.00)

18/10 /2021	Variations in Free Flowing Plastics	Irregular	9	(New PET Bottles)	4.6	200	200	0.15 (0.02)	0.08 (0.12)	0.06 (0.18)	0.16 (0.017)	0.92 (0.00)
					40	160	200	0.17 (0.12)	0.08 (0.13)	0.08 (0.17)	0.17 (0.017)	6.36 (0.00)
				Organic Plastics (Sheets)	2.3	120	280	1.38 (0.00)	0.85 (0.00)	0.57 (0.00)	1.59 (0.00)	1.85 (0.00)
					4.6	80	200	1.39 (0.00)	0.88 (0.00)	0.8 (0.00)	1.84 (0.00)	4.21 (0.00)
19/10 /2021	Variations in Free Flowing Plastics	No	0	Pellets	20	200	200	1.6 (0.00)	0.88 (0.00)	0.82 (0.00)	1.69 (0.00)	0.87 (0.00)
		Irregular	0	(New) PET Bottles Partly Submerged	4.6	240	200	-0.04 (0.82)	0.01 (0.3)	0.01 (0.32)	0.04 (0.2)	-0.12 (0.97)
					40	240	160	0.04 (0.19)	0.01 (0.26)	0.02 (0.17)	0.03 (0.26)	-0.45 (0.96)
			9	Wrapped Fishing Nets / Ropes with Bottles	8.3	240	320	-0.02 (0.99)	-0.02 (0.98)	-0.02 (0.95)	-0.04 (0.99)	-1.86 (0.00)
				Partly Submerged Bottles	4.6	200	200	-0.15 (0.82)	-0.12 (0.93)	-0.04 (0.8)	-0.23 (0.98)	0.78 (0.002)
20/10 /2021	Variation in Wave Conditions	Irregular	5	Plastic Sheets and Bags	8.3	240	320	0.62 (0.00)	0.42 (0.00)	0.44 (0.00)	0.97 (0.00)	3.93 (0.00)
				Wrapped Fishing Nets / Ropes with Bottles	8.3	240	280	0.68 (0.00)	0.43 (0.00)	0.51 (0.00)	1.06 (0.00)	3.99 (0.00)
			9	Sheet Material	8.3	200	200	0.76 (0.00)	0.36 (0.004)	0.46 (0.00)	0.73 (0.00)	2.77 (0.00)
			17	Sheet Material	8.3	320	440	0.48 (0.009)	0.3 (0.002)	0.42 (0.00)	0.77 (0.00)	0.92 (0.00)

		Irregular and Capillary	17	Wrapped Fishing Nets / Ropes with Bottles	8.3	200	200	0.49 (0.003)	0.29 (0.001)	0.39 (0.00)	0.66 (0.00)	-2.38 (0.009)
				Sheet Material	8.3	160	160	0.27 (0.2)	0.23 (0.4)	0.27 (0.12)	0.58 (0.09)	-2.11 (0.008)
21/10 /2021	Capillary Waves	Irregular and Capillary	5	Sheet Material	8.3	160	320	0.64 (0.00)	0.31 (0.00)	0.42 (0.00)	0.77 (0.00)	0.22 (0.01)
				Nets / Ropes	8.3	160	160	0.68 (0.00)	0.43 (0.00)	0.5 (0.00)	1.06 (0.00)	3.9 (0.00)
			9	Sheet Material	8.3	200	240	-0.02 (0.68)	-0.02 (0.67)	0 (0.57)	-0.05 (0.82)	3.84 (0.011)
				Nets/Ropes with Bottles	8.3	200	240	-0.03 (0.57)	-0.05 (0.82)	-0.07 (0.89)	-1.74 (0.99)	-1.74 (0.92)
	Variations in Free Flowing Plastics	Irregular	9	Styrofoam	10	240	200	0.18 (0.00)	0.03 (0.32)	0.05 (0.02)	0.03 (0.3)	1.11 (0.00)
				Lids / Caps	10	320	200	0 (0.7)	-0.03 (0.76)	0.01 (0.28)	-0.1 (0.9)	0.31 (0.45)
				Cigarette Filters	10	200	200	0.09 (0.05)	-0.02 (0.68)	0 (0.51)	-0.05 (0.77)	-0.26 (0.87)
22/10 /2021	Variations in Free Flowing Plastics	Irregular	9	Cutlery	14	200	200	1.9 (0.00)	0.83 (0.00)	0.7 (0.00)	1.4 (0.00)	1.89 (0.00)

The results from Table 3.6 indicate that statistically significant differences were found in 17/31 cases between the test and reference acquisitions in the C-band data with a boxcar filter applied. A statistically significant difference was found in 23/31 case between the test and reference acquisitions in the X-band data with the filter applied. Here, we can see that nearly all test cases using sheet material were found to have significant differences. We can also see that our smaller items, such as lids/caps and cigarette filters, still produced no significant difference in backscattering. Another notable point is that tests using identical materials but with induced capillary waves showed that with induced capillary waves we cannot detect a significant difference in backscattering for the higher wave conditions (9 cm and 17 cm waves). The only test cases

where the statistical difference was detectable with induced capillary waves was the sheet material (8.3 g/m2) and nets/ropes (8.3 g/m2) in 5 cm waves.

Table 3.7 Results of statistical analysis undertaken on 2nd campaign measurements with the use of a boxcar filter. Values filling the table are the results of the difference of the reference measurement and test measurement in a linear format, with the p-value of the test in brackets. Any value in green shows that the alternative hypothesis was fulfilled; any value in orange shows that the null hypothesis was fulfilled.

With Boxcar Filter								C-Band				X-Band
Date	Objective	Wave Pattern	Hs [cm]	Plastics	Concentration [g/m2]	No. of Acquisitions / Samples C-Band	X-Band	HH	HV	VH	VV	VV
26/01/2022	Free Floating Plastics	Irregular	9	Spheres [2cm] in Lines	6.4	240	280	-0.08 (0.95)	-0.04 (0.95)	-0.08 (0.94)	-0.08 (0.94)	1.14 (0.00)
					40	240	200	-0.09 (0.0.9118)	-0.04 (0.94)	-0.03 (0.89)	-0.1 (0.97)	0.94 (0.00)
					80	240	200	-0.06 (0.99)	-0.02 (0.81)	-0.06 (0.98)	-0.1 (0.95)	1.05 (0.00)
					120	240	200	0.01 (0.38)	-0.01 (0.68)	0.08 (0.15)	0 (0.54)	1.18 (0.00)
					153	240	200	-0.12 (0.99)	0 (0.49)	-0.01 (0.57)	0.04 (0.51)	1.23 (0.00)
27/01/2022	Free Floating Plastics	Irregular	9	Spheres [2cm] with holes Taped	2	240	200	-0.02 (0.63)	0 (0.49)	0.04 (0.07)	0.04 (0.27)	0.19 (0.13)
					4	240	200	0.08 (0.06)	0.05 (0.05)	0.01 (0.38)	0.08 (0.11)	-0.09 (0.63)
					6.4	240	200	0.12 (0.01)	0.05 (0.04)	0.03 (0.18)	0.1 (0.05)	0.15 (0.023)
					20	240	200	0.05 (0.19)	0.04 (0.06)	0.04 (0.07)	0.09 (0.05)	0.14 (0.002)
	Full 9cm Reference			No Plastic	0	240	200	0.13 (0.08)	0.03 (0.15)	0.05 (0.06)	0.11 (0.07)	0.37 (0.1)

28/01/2022	Free Floating Plastic	Irregular	9	Bottles	20	240	480	0.1 (0.013)	0.04 (0.14)	0.05 (0.08)	0.06 (0.17)	0.95 (0.00)
				Bottles	40	240	200	0.12 (0.012)	0.06 (0.08)	0.04 (0.06)	0.11 (0.02)	0.94 (0.00)
				Straws (24cm)	20	240	400	0.1 (0.04)	0.05 (0.09)	0.05 (0.018)	0.06 (0.13)	4.06 (0.00)
				Cylinder Foam (20cm)	20	240	400	0.12 (0.02)	0.07 (0.05)	0.09 (0.02)	0.14 (0.017)	2.68 (0.00)
				Cylinder Foam (10cm)	20	240	400	0.19 (0.02)	0.1 (0.02)	0.13 (0.02)	0.18 (0.019)	1.94 (0.00)
31/01/2022	Free Floating Plastic	Irregular	9	Cylinder Foam (5cm)	20	240	280	0.12 (0.05)	0.02 (0.17)	0.03 (0.12)	0.08 (0.04)	2.17 (0.00)
				Straws (12cm)	20	240	280	-0.01 (0.58)	0.01 (0.37)	0.01 (0.26)	-0.01 (0.6)	0.85 (0.00)
				Straws (6cm)	20	240	200	0.01 (0.34)	-0.01 (0.66)	0 (0.59)	-0.04 (0.76)	0.18 (0.03)
01/02/2022	Free Floating Plastic	Irregular	9	Spheres [2cm] with holes Taped	10	240	200	0.2 (0.03)	0.06 (0.16)	0.08 (0.17)	0.1 (0.39)	0.49 (0.03)
			17		10	240	200	0.14 (0.03)	0.05 (0.03)	0.06 (0.04)	0.08 (0.05)	-0.12 (0.83)
					20	240	200	0.11 (0.07)	0.04 (0.18)	0.08 (0.02)	0.14 (0.04)	0.19 (0.11)
					40	240	200	0.2 (0.02)	0.11 (0.06)	0.07 (0.07)	0.17 (0.04)	-0.03 (0.56)
02/02/2022	Free Floating Plastic	Irregular	5	Spheres	10	240	200	0.2 (0.59)	0.09 (0.04)	0.05 (0.06)	0.17 (0.02)	0.26 (0.00)
					20	240	200	0.02 (0.3)	0.06 (0.03)	0.1 (0.13)	0.19 (0.04)	0.53 (0.00)
					40	240	200	0.17 (0.09)	0.1 (0.012)	0.06 (0.07)	0.21 (0.04)	0.35 (0.00)

						240	200	0.38 (0.015)	0.29 (0.00)	0.25 (0.00)	0.53 (0.00)	3.38 (0.00)
			9	Plastic Lids	10	240	200	0.02 (0.4)	0.01 (0.39)	0.08 (0.017)	0.06 (0.24)	2.18 (0.00)
			17			240	200	0.27 (0.00)	0.27 (0.00)	0.16 (0.00)	0.45 (0.00)	2.79 (0.00)
03/02/2022	Free Floating Plastic	Irregular	5	Bottles	20	240	200	0.17 (0.02)	0.1 (0.12)	0.08 (0.06)	0.21 (0.018)	1.38 (0.00)
						X	200	-	-	-	-	1.38 (0.00)
	Full 5cm Reference			No Plastic	0	240	200	0.1 (0.13)	0.04 (0.53)	0.06 (0.35)	0.09 (0.6)	0.32 (0.29)
	Free Floating Plastic		9	Bottles	10	240	200	0.02 (0.058)	0 (0.2)	0.01 (0.07)	0.07 (0.056)	1.07 (0.007)
			17			240	200	0.02 (0.09)	0.01 (0.051)	-0.01 (0.2)	0 (0.44)	-0.03 (0.78)
	Full 17cm Reference			No Plastic	0	240	200	0.02 (0.36)	-0.03 (0.29)	-0.02 (0.66)	-0.06 (0.45)	-0.5 (0.99)
04/02/2022	Free Floating Plastic	Irregular	9	Bubble Wrap	1m Long Strip	X	200	-	-	-	-	1.63 (0.00)
				Plastic Lids (No Edges)	10	240	200	0.05 (0.15)	0.02 (0.16)	0.03 (0.09)	0.05 (0.16)	3.28 (0.00)
			17			240	200	0.06 (0.12)	-0.03 (0.74)	-0.04 (0.83)	-0.01 (0.59)	1.75 (0.00)

The results from Table 3.7 indicate that statistically significant differences were found in 25/37 cases between the test and reference acquisitions when a boxcar filter was applied. These were found nearly exclusively in the X-band frequency, where the only experiments found to not be significant were those that used plastic spheres in =< 10 g/m2 concentrations from the 27th of January and the 1st of February, the smallest

size of plastic straws from the 31st of January and the use of plastic bottles in the 17 cm wave heights from the 3rd of February. With the application of the boxcar filter, the wave conditions were still found to not be statistically different between the test and reference cases, thus eliminating the changes in wave patterns over time within the tank being a cause of changes in backscatter.

Three cases were found in the C-band where a statistically significant difference was found but we are cautious about two of these results. The first case, the 6.4 g/m2 plastic spheres on the 27th of January, we deem to be a possible false alarm as only the HH polarisation was flagged as statistically significant, and we found no other test cases within the C-band to be statistically significant even at higher concentrations. The second case is the 17 cm wave height plastic lids at 10 g/m2. The reference acquisition that we took was from before this test was corrupted, so we used one of the previous days' reference acquisitions from the 17 cm height tests. Therefore, we believe that this has caused the false positive to be found between the cases, as we have not seen a significant difference in C-band at 9 cm wave heights for the same items, where detection should be easier.

3.4 DISCUSSION

Upon inspection of the acquisitions, it was clear that the backscatter within the wave tank was, on average, higher when plastic was on the water.

3.4.1 Frequency Comparison

When plotted in Figure 3.4, this backscattering difference can be as high as 10.9 dB, within the X-band frequency experiments. Nearly all X-band acquisitions showed greater differences in backscattering between the test and reference acquisitions than those found in C-band, which can be seen in Tables 3.4 – 3.7. We believe that this is due to the higher X-band frequency having a smaller wavelength when compared with the lower frequency C-band. From the frequency range swept in X-band (9.5–10.5 GHz), we should have a wavelength of approximately 3 cm, compared with C-band (5–6 GHz), where we have a wavelength of approximately 5.5 cm. Using the proposed scattering mechanisms model, there are a few reasons why this could happen. Firstly, most plastic items used in this experiment have a length and/or width that is smaller than the wavelength of C-band. It is also true that the clutter scattering (from clean water waves) at X-band may be higher, but the target may have a more peculiar frequency response. Additionally, the indentations that plastic produces in water are generally around 1 cm–2 cm (as the floating plastics do not submerge deeply into the water), which is within a good range of values for detection with X-band but is indeed too small for C-band. This may be the reason why we do not detect this indentation scattering mechanism in C-band. Finally, the capillary waves formed by the impact of waves on plastic are generally small (due to the size of plastic, they looked around 1 cm wave height, as can be seen later in Figure 3.9), and, therefore, they produce more backscattering in X-band than in C-band.

This is not to say that C-band cannot produce higher backscattering from the plastic objects introduced in the tank. C-band was capable of detecting significant differences in backscattering from the first measurement campaign, where this can be seen from the thin plastic items that produced high wave-generation scattering, such as the flatter sheets, nets, and lids items.

At reduced concentrations, there will be as little as a couple of items through the ROI at a time. Higher concentrations allow for more material to accumulate together and create a more homogonous surface of plastic.

3.4.2 Minimum Quantities Detected

The second campaign was aimed at finding out the minimum amount of plastic detection from differing items, which we believe is due to the shape and size of the object, but also from how the object floats on the water and how it can accumulate together. One example of accumulation effects can be seen in Figure 3.8, where the experiments undertaken on 26 January 2022 used plastic spheres from the plastic dispenser. These plastic spheres were dropped in clumps over extended periods of time; however, the following experiments on 27 January 2022 had the plastic dispenser modified so that the spheres were dropped at a more gradual constant rate, with fewer spheres dropping at the same time. The changes in how these spheres were dropped, and subsequently how they clumped together, has an effect on their detection capabilities. We believe this is due to the fact that some nonlinearity effects come into play when converting to intensities. That is to say, a uniform concentration will produce a lower overall intensity than a sparse distribution, where few pixels have a higher intensity. This is because the mean of the squares is higher than the square of the means. From a practical point-of-view, this is also understandable since we expect high concentrations to stick out as bright pixels, which will be more easily detected than a slightly higher intensity of overall pixels.

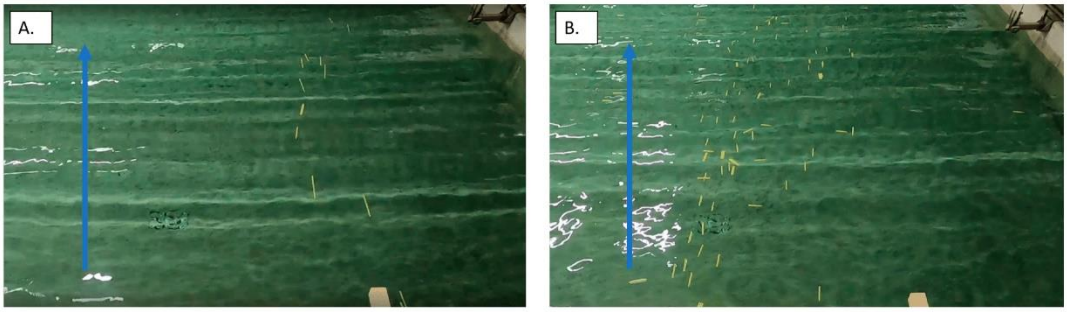

Figure 3.8 A still from footage taken from a GoPro mounted on the Ground Radar frame. (A) Shows the yellow 24 cm straws moving perpendicular to the waves on top of the water. (B) Shows the yellow 6 cm straws moving perpendicular, parallel, and diagonal with the waves. Blue arrow indicates the direction of the moving wave.

Other non-linearity effects could be created from the third proposed scattering mechanism, where higher concentrations could produce more persistent capillary waves, but this idea is harder to prove without focussed hydrodynamic experiments.

3.4.3 Size, Shape and Orientation of Objects

With regard to the size of the object, we can see that the experiments with plastic straws in Figure 3.8 give key information on this. The straws used in each experiment

were the same plastic and concentration, the only changes were the size of the objects and, subsequently, the number of items used to create the concentration (i.e., as the size of straws halved, the number of objects doubled). We can see that for the X-band frequency, a significant difference in backscattering was found when the straws were 24 cm and 12 cm. However, when the straws were 6 cm, we found no significant difference. This can possibly be related to the wavelength of the X-band frequency being similar to the size of the object and causing difficulties, but it may also be due to the orientation of the objects travelling through the water. It should be noted that when the full-length straws were placed into the water, they travelled nearly exclusively perpendicular to the waves. However, when the size was reduced to 6 cm, the orientation of the straws changed as some moved perpendicular with the wave and others moved parallel, while some moved diagonally (as seen in Figure 3.8). We believe that this orientation will have an effect on the backscattering, potentially due to the size of the object front that is facing the radar changing, or with changes in the polarisation. However, due to the lack of quad-polarimetric X-band data, an investigation into these effects was not possible.

An interesting observation from the measurement campaigns was that some of the flat objects, such as the lids, had strong backscattering. The scattering mechanism that may be dominant here is the wave generation scattering from the object, due to the impinging of waves. We noted that capillary wave generation in flatter objects was especially pronounced (as seen in Figure 3.9).

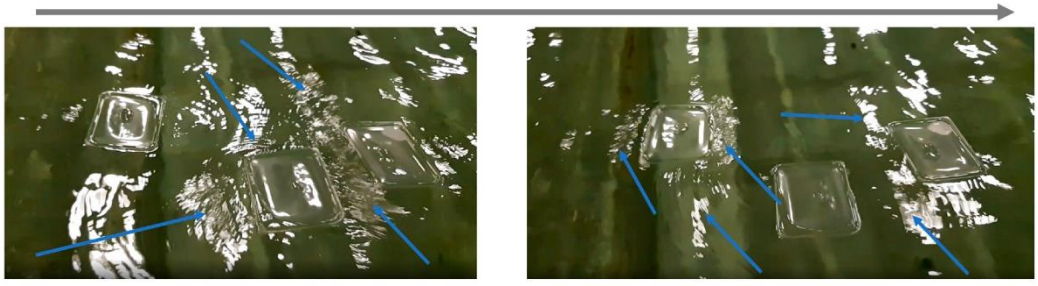

Figure 3.9 Still images from camera footage of the plastic lids moving on the water surface. The blue arrows highlight capillary wave generation from the objects interacting with the waves. The grey at the top of the figure indicates the direction of wave movement.

Another interesting observation in relation to our scattering mechanism concept is that a significant difference in backscatter was found in the X-band measurements of plastic bottles (both 20 g and 40 g/m2). Interestingly, when these bottles were filled with water and became partially submerged, this significant difference in backscatter

could not be found anymore. We believe this helps strengthen the 'indentation' scattering hypothesis, as the water that is filling the space in the bottle is also filling in the indentation that would have been created from the 'empty' space inside the plastic. An example of this hypothesis is shown in Figure 3.10.

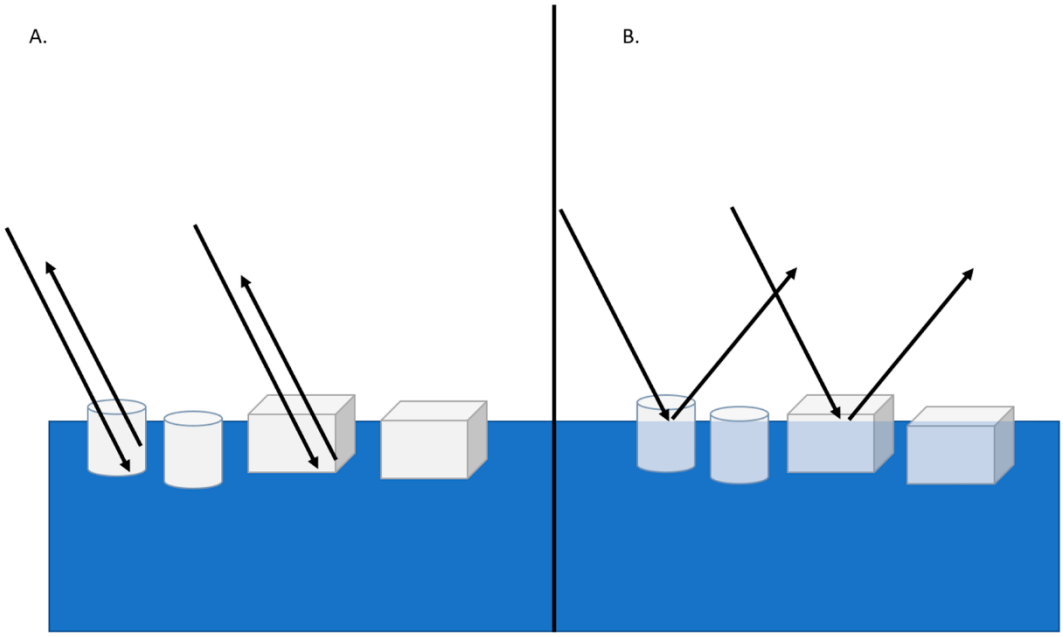

Figure 3.10 Radar backscatter interacting in different scenes. (A) 'Indentation' Scattering is a change in backscatter from 'dry' plastics that are partially submerged with no layer of water on top but are producing indentations in the water. (B) Plastics with water filling with void space where 'indentation' scattering is created, causing an increase in specular scattering.

3.4.4 "Stripe" Features in Radargrams

In several radargrams we could observe "vertical stripes" of bright targets. We hypothesize that these are due to either breaking waves or particularly large waves moving along the tank. When a larger wave moves in the tank, it may produce conditions close to breaking where it generates capillary waves from the crest of the wave. Those waves are quite fast moving and, therefore, they smear their energy over all of the spectrum of the SFCW. This could be seen as, while the radar is doing the sweeping, they appeared in different range locations producing the smearing we observed as an almost vertical feature.

Those features were more visible at higher wave heights. Additionally, the tendency to break (and produce capillary waves) was stimulated by the presence of plastic, which presents discontinuities. Those capillary waves were the ones we identified as the third scattering mechanism, which during this phenomenon (of breaking waves) became the dominant one.

3.4.5 Wave Size

The size of the waves within the wave tank also dictated the radar capabilities for monitoring plastic. In most cases, 17 cm wave heights made the detection of plastic materials more difficult. We believe that this is due to the 17 cm waves breaking more and causing an increased roughness from the harsher waves, which masks any of the backscattering from the plastic materials. The exceptions to this are plastic lids and sheet materials, both of which are flat objects which created strong capillary wave interactions with the surrounding waves when moving through the wave tank. The increased wave height resulted in generating more capillary waves, which, therefore, facilitated detection even in this scenario.

3.4.6 Wind Conditions

In the open ocean, it was common to find changing wave conditions induced by changing wind speeds. Gusts of wind within the open ocean can generate foam and high frequency capillary waves. In some of our testing (marked irregular + capillary in tables above), we induced wind-driven capillary waves through the use of a fan located to the side of the wave tank. The fan was operational during both the reference and test acquisitions. We can see from Table 3.5 and Table 3.7 that plastic sheet materials at 8.3 g/m^2 were detectable in 9 cm irregular waves when the wind-induced capillary waves were not present. However, in our irregular + induced capillary wave testing, we found that the plastic sheet material became undetectable. This could be due to our 'wave generation' scattering mechanism being masked by the winds. These mechanisms need to be taken into account for future testing or missions.

3.4.7 Checking Stability

To ensure that the differences in backscattering were not caused by changes in the wave spectra generated by the wave generator over the measurement periods of each experiment, we tested a full test measurement of only waves (no plastic) against a reference measurement taken beforehand for each wave type used throughout the campaign. As seen in Table 3.6 and Table 3.7, we can observe that the full 5 cm, 9 cm, and 17 cm wave tests found no significant difference between the reference and test measurements from these experiments. This means that we can safely presume that the significant differences in backscattering were created from the addition of plastic into the tank and not from changes in the waves themselves over the measurement periods.

3.4.8 Extrapolation to Satellite Data

The use of C-band radar has previously been utilised in research to try and understand the capabilities of detection from space using Synthetic Aperture Radar (SAR). Topouzelis, et al., (2019) attempted to use Sentinel-1 (5.405 GHz) SAR imagery to monitor and detect plastic litter targets off the coast of Lesvos Island, Greece. They found a difference in backscatter where variations were found between a 10 × 10 m target made from plastic bottles and the surrounding water. However, there were no differences found between two other targets of the same size, made from plastic bags and from fishing nets. These observations were noticeable in the VV polarised Sentinel-1 imagery. Unfortunately, no X-band imagery was obtained during this study to compare the performance of different frequencies. However, we can see that the use of C-band still has the potential to detect plastics in larger concentrations and accumulations.

The use of Sentinel-1 C-band SAR data has also been used to monitor large plastic accumulations by dams. Simpson et al., (2022) found that large accumulations of primarily plastic materials were detectable using Sentinel-1 SAR data. Using change detection algorithms, they found the best detector, the Optimisation of Power Difference detector, could detect plastic accumulations with accuracies varying from 85 to 95%, depending on the false alarm rate within their test cases. This further showcases the use of C-band radar imaging for the remote sensing of plastic accumulations.

We have seen that X-band appears to be the most suitable frequency for detecting plastic pollution, compared with C-band, and that future missions (airborne or satellite) focusing on the detection of plastic pollution should focus on the use of this frequency. We believe that these results should aid future testing/experiments for plastic detection with radar and that the details within Section 3.4.1. – 3.4.6. can be used for future mission planning to tackle marine plastic pollution. Another point of note is that our range resolution from the ground-radar is 15 cm, which is a much finer resolution than most SAR satellites. However, new SAR X-band resolutions are capable of reaching a 25 cm resolution, as shown by the ICEYE constellation, and finer resolutions may be possible in the future.

To conclude, it has been shown that plastic can induce a difference in backscattering in the VV polarisation channel (mostly in X-band). It is, therefore,

expected that a future plastic detector with satellite data will need to be built as an anomaly detector.

3.5 FUTURE WORK

This study has begun to shed light on radars' capabilities in monitoring marine plastic litter from a lab-based setting. However, more wave heights, concentrations, and the use of real mixed targets could be used in future experiments. While this list of different test conditions is not exhaustive, we have started testing a set of conditions that cover calm to mid sea states.

A possible next stop of research would involve scaling this upward, with radar measurements being taken from on-board an airplane. This will allow us to see the scalability of this experiment into the real world and to begin to quantify if these techniques would be possible from space in the future.

3.6 CONCLUSIONS

The practice of remote sensing in the detection of marine litter debris on water is a relatively new field and the potential and capabilities of radar is yet to be fully understood. This study has shown that backscattering differences in C- and X-band between the reference 'clean' water and test water filled with plastic can be detected in some conditions (based on the statistical analysis). Overall, the results indicated that the X-band frequency performed significantly better than the C-band frequency in detecting differences in backscattering when plastic materials were within the water, with X-band detecting significant differences in backscattering in 37/60 cases compared with C-band detecting differences in 10/60 cases. We believe that this is due to the higher X-band frequency having a smaller wavelength when compared with the lower frequency C-band, causing a higher capability to detect indentation scattering from plastic items. We also found that the difference in backscattering was dependent on the size and shape of the plastic object, as well as the wave conditions which the plastic is moving on. This article provides key information on the capabilities of radar for detecting marine plastic litter and provides details which can be used for future planning in regard to tackling the remote sensing of marine plastic pollution.

Chapter 4: Investigating Plastisphere-based Surfactant Wave Dampening, using Ground-Radar Based Measurements

This chapter looks at the effects of plastisphere-based surfactant wave dampening on radar data. Backscatter analysis is undertaken on two measurement campaigns of data. This analysis shows that plastisphere-based surfactants are capable of dampening wind-generated waves in an experiment scenario and the outcomes of this experiment are extrapolated into what this could mean for real-world applications of using surfactants as a proxy for monitoring marine plastic pollution.

4.1 INTRODUCTION

Plastic debris is a global threat to marine environments. Due to its abundance, durability and persistence, there is evidence of plastic litter in even the most remote locations of our planet (Worm, et al., 2017). Plastics also account for between 60 – 95% of global ocean marine litter, making them the most common type of debris (Gall & Thompson, 2015) (Barnes, et al., 2009). Even with this abundance of plastic litter within our oceans, accumulations of plastic pollution are not well mapped (Martinez-Vicente, et al., 2019). This causes great concern due to the risks associated with marine plastic pollution, whether it is impacts on marine species (Gall & Thompson, 2015) or the human health issues associated with plastics (Barboza, et al., 2018) (Yusuf, et al., 2022).

Traditionally, measurements of marine plastics have been performed in-situ. However, budget, spatial and accessibility issues can cause complications within these measurements. Remote sensing has been explored as a means of monitoring plastic pollution, due to its successful history in providing global synoptic coverage of other ocean phenomena and processes (Rani, et al., 2021). Optical systems have been the primary focus of research into the remote sensing of marine plastic pollution, with wavelengths including visible (Biermann, et al., 2020), near-infrared (Hu, 2021), and

shortwave infrared (Garaba, et al., 2018). However, cloud cover can cause limitations for optical observations of oceans (King, et al., 2013), and the current scientific consensus is that complementing different methods of remote sensing technologies with each other will improve the monitoring of marine plastics (Maximenko, et al., 2019).

One sensing system that is being explored is Synthetic Aperture Radar (SAR). SAR is an active microwave fine-spatial resolution imaging method, capable of imaging in nearly all-weather conditions and light conditions (Toth & Jozkow, 2016). SAR has been used to measure many physical properties of the Earth's surface, including the cryosphere, topography, forestry and natural hazards, but it is SARs sensitivity to surface roughness (Mattia, et al., 1997) which makes it particularly valuable in monitoring rivers, oceans and other marine environments (Lyzenga, et al., 2004). SAR also has an extensive history of monitoring oil spills / slicks (Nirchio, et al., 2005) and biogenic films (Gade, et al., 1998). Previous research using SAR for monitoring plastic pollution has shown that surface plastics can be detected due to an increased backscatter from plastic items and their interactions with the water surface (Simpson, et al., 2022) (Simpson, et al., 2023) (Topouzelis, et al., 2019). However, these studies use a combination of larger targets and concentrations of plastic debris, and / or higher resolution pixel sizes than what is available via satellite data presently. Also, direct backscatter measurements of plastic debris are only capable of being observed on surface waters as microwaves cannot penetrate through the water column. This can cause issues for estimating global plastic debris concentrations, as we can only directly measure plastics on the surface with SAR and in larger concentrations. Therefore, other methods of measuring these materials need to be explored.

In this chapter we present radar measurements which utilize a way to monitor marine plastic pollution by using plastisphere-based microbial surfactants as a proxy for detection through a series of measurement campaigns conducted in a lab environment. In this work, we address the following research question:

1. Can plastisphere-based surfactants produce a change in backscattering from lab-based wave measurements.

The novelty of this study resides in the experiments carried out and the findings coming from the statistical analysis of those datasets. We show that radar backscatter differs between control and test conditions in a lab setting (surfactants not present vs

surfactants present) and that wave dampening from plastisphere-based surfactants is detectable in radar measurements.

The overall aim of this research is to find out if SAR data could be used to monitor and detect surfactant slicks associated with marine plastic pollution.

4.2 METHODOLOGY

4.2.1 Marine Debris and the Plastisphere

Marine plastic debris has been shown to form a new habitat, named the 'plastisphere' (Zettler, et al., 2013). The plastisphere occurs when a combination of microbial communities colonizes a plastic substrate. These microbial communities are capable of biofilm formation, where these biofilms are different to their surrounding environment in terms of community structure (Zettler, et al., 2013). The plastisphere can also be related to an increase in microbial biomass (Qian, et al., 2007) due to these biofilm formations.

Many studies have reported the colonization of plastic debris by bacterial phyla which would not normally be common within those waters. Alphaproteobacteria, roseobacteria and gammaproteobacterial groups have all been found residing on plastic debris within the Atlantic Ocean (Osborn & Stojkovic, 2014). Groups of bacteria not native to the North Atlantic Ocean have also been found residing on plastic debris floating through the environment (Lobelle & Cunliffe, 2011), where these organisms are capable of surviving for longer periods than those in the surrounding seawater (Webb, et al., 2009). Microbial abundance has also seen to be more prominent within sites higher marine plastic concentrations (Carson, et al., 2013).

Microbial communities are capable of producing surfactants as part of their metabolism (Pardhi, et al., 2022). Surfactants have been shown to alter the surface tension of the near-surface layer of the ocean (Hühnerfuss, et al., 1987). This alteration of surface tension causes the dampening of short gravity-capillary waves on the sea surface (Hühnerfuss, et al., 1981).

Radar measurements are particularly sensitive to surface roughness (Van der Wal, et al., 2005) (Shi, et al., 1997). Calm water bodies in radar imagery tend to be relatively smooth, with the electromagnetic energy bouncing in a specular direction,

away from the sensor. However, water bodies can have increased surface roughness from wind-stress or water currents, which can result in a high backscattering of our radar signal known as Bragg-scattering (Phillips, 1988). Surface waves are influenced by the capillarity of the water and differences in these waves will affect Bragg-scattering (Phillips, 1988). It has been shown that dampening is detectable in radar imaging, since surfactants dampen the capillary waves on the sea surface, and radar is sensitive to changes in surface roughness. This has been thoroughly documented (Hühnerfuss, et al., 1981) with the use of radar imaging for oil spill detection (Latini, et al., 2016). It has also been found that the damping ratio of surfactants increases with Bragg wavenumber and decreases with higher wind speeds (Latini, et al., 2016). However, at very high wind speeds, the damping effect of surfactants can disappear in the background noise of wind-generated waves, with higher wind speeds causing the surfactant to incorporate with the underlying sea surface due to breaking waves. Due to this, oil films become undetectable at wind speeds higher than $10ms^{-1}$ to $14ms^{-1}$ (Alpers & Espedal, 2004). For instance, bacterium-based surfactant dampening has been seen in TerraSAR-X images in the Gulf of Mexico, where an abundance of Bacillus spp. was producing sea slicks seen within the Synthetic Aperture Radar (SAR) imagery (Howe, et al., 2018).

The aim of this research is to understand if plastisphere-based microbial surfactants can dampen waves and if these are detectable through radar measurements.

4.2.2 Radar System and Experiment Setup:

The measuring equipment consisted of a ground-radar, where the back end is an Anritsu Site Master S820e Vector Network Analyser (VNA). It is connected to broadband antennas, the specification of which can be seen in Table 4.1. The antennas were connected via semi-rigid cables (DC to 18 GHz) to the single input and output ports of the VNA.

Table 4.1 Measuring equipment specifications for ground radar to measure surfactant experiments.

Equipment	Frequency Range	Polarisation	3dB Beamwidth	Dynamic Range
Anritsu Site Master S820e VNA	1 MHz – 14 GHz	-	-	110 dB from 20 MHz to 14 GHz

Broadband Antenna	730 MHz – 11 GHz	Quad-pol	L-band: 45° C-band: 35° X-band: 20°	

The radar equipment was located in the centre of a polytunnel, which acted as a semi-controlled environment. The layout of the polytunnel can be seen in Figure 4.1.

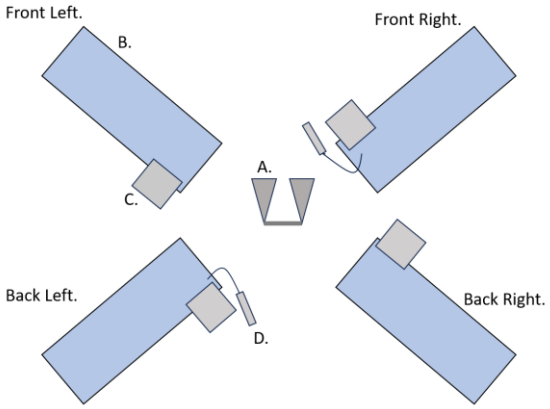

Figure 4.1. Layout of Polytunnel Experiment Setup. A. Centre of image is our radar set-up that can be rotated on a turret. B. The four blue rectangles represent our HDPE plastic tanks used for the experiments, they are equally distanced from the radar when the horns point toward the tank for measuring. All tanks are also measured from the same viewing angle. C. The grey box represents the position of the fan used to generate waves within each tank. The fan was mounted to the side, with air blowing down into the tank and across the water surface, it was positioned in identical positions for each tank. D. represents our water temperature loggers used within two of our tanks. The labels of the tank position are referred to later in the article for associating measurements with each tank.

The tanks used for these experiments were made from high-density polyethylene (HDPE). They are 180 x 120 x 60 cm (LxWxH). This plastic polymer was chosen as it is among the most abundant polymer types found within aquatic environments (Erni-Cassola, et al., 2019; Smith, et al., 2018). Each tank was filled with 30cm depth of water and this level of water was maintained over the course of the experiments as evaporation of the water occurred especially during warmer temperatures. In preliminary testing of our setup, we had two temperature loggers within the polytunnel, which measured water temperature within two of our tanks. However, the readings from these loggers were near identical and so we have only shown the results from one logger within this paper.

To create a control experiment dataset, two tanks had a biocide added into the water. This biocide was maintained over the experiment duration. The biocide was added initially into the front and back right tanks, which stopped any microbial growth from occurring within those tanks. This allowed a comparison of the left-side tanks with the right-side tanks, to see the impact that microbial surfactants could have on the radar measurements.

An external 30cm sphere used as a target was located at the end of each tank. This external sphere was used as a target for calibrating polarimetric behaviour (further details in image formation). The radar was looking at the tanks with an incidence angle ranging between 30° and 40°. The sweeps in frequency considered 1 GHz (for each band), which resulted in a theoretical range resolution of 15cm.

4.2.3 Experiment Protocol

Located on our tanks was an external fan, which was used to generate wind-driven waves. This fan was mounted to the side of the tank and pointed directly down, so that the air blew vertically down the wall of the tank and across the top of the water, generating small capillary waves.

On each date where data was collected, for each tank, an acquisition was taken with no waves generated, followed by an acquisition being taken with the fan switched on and waves generated. The initial acquisitions with no waves were used as a reference where we could compare the backscatter between waves being on and off within each tank.

There were two sets of measurement campaigns conducted during this experiment. The first was to test if any dampening of the waves was seen within our radar measurements with some sparser measurements taken over the duration of the campaign. The second campaign was more regular to understand the speed at which this dampening occurred within our test setup. The position of the control experiments (tanks with biocide) in the first campaign was on the right-hand tanks, this was then changed to the left-hand tanks during the second campaign to collect a dataset where the positions of the tanks had been switched to see if the same experiment outcomes occurred.

4.2.4 Image Formation

The radar architecture is a Step Frequency Continuous Waveform (SFCW), where the transmitting wave was sweeping as a linear frequency modulation in a desired bandwidth. The received signal was then processed using a Hamming window and inverse Fourier transform to focus the range profile. Each VNA sweep, therefore, produced a single range profile. During our experiments, we swept from 1 GHz to 11 GHz, focusing on the full broadband spectrum, 5 – 6 GHz and 9 – 10 GHz bands. These frequencies were chosen to understand the effect of the experiment on the full broadband spectrum itself, and on frequency ranges that are inclusive of bandwidths used by SAR satellites to monitor oil spills.

The calibration was conducted keeping in mind two main goals: (a) backscattering stability and (b) radiometric accuracy. It is known that VNA signal generators may drift in amplitude and phase during a measurement campaign since they may be dependent on temperature and humidity, as well as other factors (Bystrov, et al., 2022). The fact that the no wave references for each acquisition were taken a maximum of up to five minutes before the tests should not lead to large drifts in temperature and humidity, and therefore, not lead to drifts in the VNA. However, calibration was still necessary to more easily compare the results between different acquisitions days, and to create reassurance that any potential drift was mitigated. For this reason, we used the calibration sphere as permanent target inside our radar profile and used this as a reference to clip all of the radar profiles (for a given frequency) together. This sphere was also further used to convert the clipped images into radar cross sections.

4.2.5 Radar Data Analysis:

The analysis we performed focused on the signal intensity (or backscattering), of our measurements. The intensity was taken from all focused and calibrated acquisitions during the run of each experiment (Reference of Test). The reason for focusing on the intensity only is that we wanted to use this as a measure of wave roughness.

The following information is displayed via the following means. Images were created where the two dimensions represent the distance from the radar (no. of pixels) vs. time (no. of acquisitions taken). The image colour represents the intensity on a

linear scale. These images are often referred to as radargrams (e.g. when dealing with ground-penetrating radars). Although radargrams are affected by speckle, they contribute to the qualitative understanding of the experiments from each measurement session.

The visualization itself would normally be considered a good way to qualitatively compare backscattering differences between the test (Fan On) and reference (Fan Off) experiments. However, the differences in backscatter changes are quite small and difficult to assess qualitatively.

Therefore, to create a quantitative insight into the data, a statistical analysis was undertaken. Each test measurement underwent a statistical analysis. Starting from the radar profile, we identified our Region of Interest (ROI) representing the water tanks. The pixels in that area were averaged over time to obtain a single mean value for the ROI. The first value is obtained from the acquisitions taken while waves were generated inside the tanks, the second value is obtained when the fan was off and there were no waves. The difference of these values was then calculated for each tank, to create tables of results that show the difference in waves vs no waves over time, to see if the effects of dampening were present. This technique allows us to remove the effect of the background where different tanks may have a different background clutter.

We took the differences that were obtained previously, and then performed a "difference of the differences" (DotD). The DotD statistical test is a method used to compare changes or differences between two or more groups over time or in different situations. For our statistical analysis, we took our mean difference within each tank, calculated from the ROI as explained above.

This has the equation:

$$\Delta\mathcal{X} = \bar{\mathcal{X}}_A - \bar{\mathcal{X}}_B$$

Where A is waves-generated acquisition and B is no-waves.

We then found the difference between the mean differences, using our biocide control tanks as the reference. For the first campaign, we used the front right tank as the reference.

$$\Delta I_1 = (\bar{\mathcal{X}}_{A1} - \bar{\mathcal{X}}_{B1}) - (\bar{\mathcal{X}}_{A2} - \bar{\mathcal{X}}_{B2})$$
$$\Delta I_2 = (\bar{\mathcal{X}}_{A1} - \bar{\mathcal{X}}_{B1}) - (\bar{\mathcal{X}}_{A3} - \bar{\mathcal{X}}_{B3})$$

$$\Delta I_3 = (\bar{X}_{A1} - \bar{X}_{B1}) - (\bar{X}_{A4} - \bar{X}_{B4})$$

Where A1 and B1 are waves-generated and no waves generated in one of our reference control biocide tanks respectively. The remaining Ax and Bx refer to the waves- generated and no waves generated data in our other tanks within the setup.

We then found the standard deviation of the DotD dataset.

$$StDev = \sqrt{\left(\frac{SD_1{}^2}{n_1} + \frac{SD_2{}^2}{n_2}\right)}$$

Where SD_X is the standard deviation of ΔI_X, and n_x is the number of observations in that group.

After we collated this data, we then applied a statistical test with hypothesis:

Null hypothesis H0: No change in mean backscattering

Alternative Hypothesis H1: Change in mean backscattering

The threshold for H1 (i.e. confidence interval) can be set using a Neyman-Pearson-derived Constant False Alarm Rate (CFAR) methodology. In case of Gaussian statistics (i.e. DotD has a Normal distribution) the CFAR only requires the knowledge of mean and standard deviation. The threshold was set as: DotD > 3 * StdDev (DotD). This threshold leads to a 99.7% confidence interval, with a corresponding false alarm rate of 0.15% as this is a one-trail test. From this testing, we could see when our experiments showed a statistically detectable difference.

4.3 RESULTS

In the first part of this section, we will show the results of plotting the backscatter between the control tanks and the experiment tanks. For the sake of brevity, the graphs here only cover a limited selection of dates from the experiments. The second part of this section includes the statistical analysis which covers every measurement that we performed.

4.3.1 Radargram Backscatter Intensity Plots

The following graphs show a comparison of the backscatter from the experiments. Here, we are showing C- and X-band, with all measurements taken

between the 5 – 6 GHz and 9 – 10 GHz frequency range respectively. We will only show results in VV polarization channel because this provide the best performance and it is normally used for oil spill detection. These plots are shown in the form of radargrams, where the colour gradient is on a linear scale.

In Figure 4.2, we see the radargram for C-band from the reference acquisitions (No Waves) and the test acquisitions (Waves Generated with Fan). We are only showing our area of interest (the water within the tank) here, as this is the data used within our statistical analysis. All data that was acquired from before the tank, or after the tank ends was cut out of the analysis.

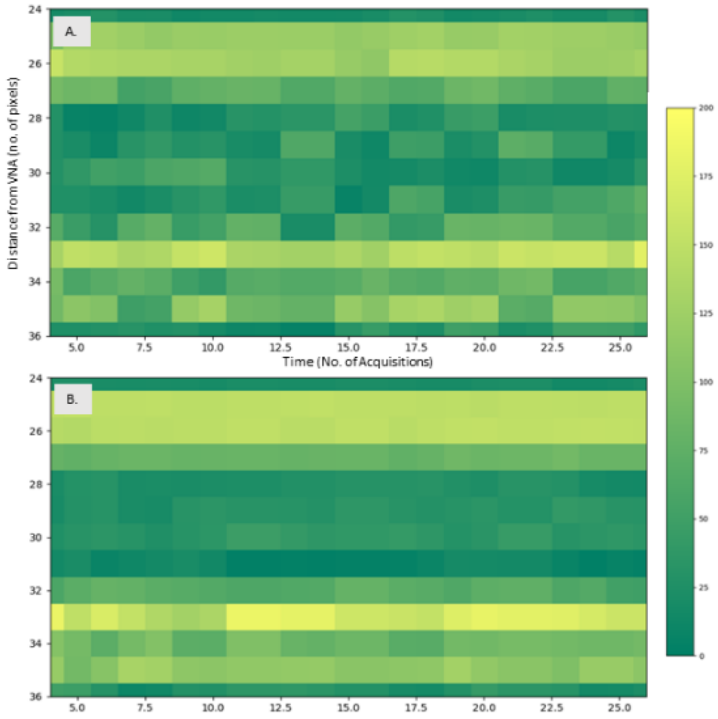

Figure 4.2 C-band intensity plot of reference and test acquisitions from one of the surfactant producing tanks on September 27th 2023. (A) shows an acquisition taken while waves were generated within the tank. (B) shows an acquisition taken while there were no waves within the tank. Colour – intensity on a linear scale.

In Figure 4.3, we can see a radargram showing the X-band frequency backscatter from the same date as above. These bands are shown separately to allow easier comparison between frequencies.

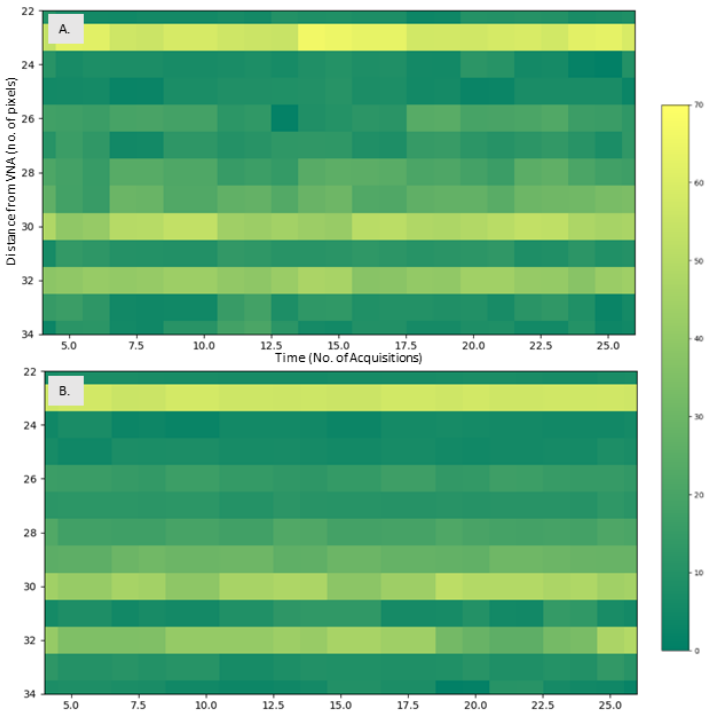

Figure 4.3. X-band intensity plot of reference and test acquisitions from one of the surfactant producing tanks on September 27th 2023. (A) shows an acquisition taken while waves were generated within the tank. (B) shows an acquisition taken while there were no waves within the tank. Colour – intensity on a linear scale.

A change in intensity can be seen within the radargrams, with a uniform layer of increased intensity seen from when the waves are generated within the tank. This showed that our ground radar is sensitive to measure the capillary waves generated within the experiments.

These measurements were taken on a regular basis to collect data that followed the potential production of surfactants within the test tanks and their respective control tanks. This allowed us to have a time series of data from within the different tanks.

4.3.2 Campaign 1: Backscatter Results and Temperature Profile

From these measurements, the differences of mean backscatter between reference and test within our ROI was measured. This was used to analyse if any trends in the differences of backscatter changed over time. Please note that for this measurement campaign, the tanks with the biocide were located on the right-side of the polytunnel, the ‘natural’ tanks were on the left side.

Table 4.2 Differences of mean backscatter between fan and no fan measurements; Biocide tanks (Right), Natural tanks (Left).

		Bands			
Date of Acquisition	Tank Position	L	C	X	Broadband
26-Apr-23	Back Left	2.11	2.35	2.58	2.37
	Back Right	2.27	2.57	2.78	2.66
	Front Left	2.39	2.59	2.82	2.63
	Front Right	2.48	2.68	2.89	2.73
03-May-23	Back Left	2.78	2.91	3.03	2.93
	Back Right	2.58	2.68	2.79	2.73
	Front Left	2.63	2.74	2.75	2.74
	Front Right	2.72	2.89	2.84	2.85
05-Jun-23	Back Left	1.59	1.73	1.74	1.74
	Back Right	2.36	2.43	2.63	2.56
	Front Left	1.12	1.22	1.79	1.56
	Front Right	2.25	2.46	2.52	2.48
15-Jun-23	Back Left	1.38	1.65	1.88	1.68
	Back Right	2.32	2.48	2.82	2.56
	Front Left	1.39	1.5	1.87	1.63
	Front Right	2.69	2.81	3.65	3.21
23-Jun-23	Back Left	1.52	1.67	1.93	1.78
	Back Right	3.2	3.37	3.64	3.45
	Front Left	1.35	1.47	1.96	1.76
	Front Right	3.25	3.4	3.72	3.57
28-Jun-23	Back Left	1.43	1.58	1.63	1.6
	Back Right	3.06	3.12	3.73	3.42
	Front Left	1	1.11	2.02	1.56
	Front Right	3.04	3.22	3.47	3.31
12-Jul-23	Back Left	1.03	1.11	1.25	1.18
	Back Right	3.09	3.33	3.77	3.33
	Front Left	1.2	1.31	2.03	1.62
	Front Right	3.21	3.37	4.25	3.79
26-Jul-23	Back Left	1.23	1.65	1.35	1.48
	Back Right	2.44	2.58	2.76	2.66
	Front Left	1.31	1.42	1.62	1.53
	Front Right	2.15	2.32	3.3	2.69

Table 4.2. shows the differences between the measurements of each tank when there were waves generated and when there were no waves. We can see at the beginning of the measurement campaign that the difference between waves vs no waves was similar between all tanks. This means that there were no changes between our tanks in the wave generation, with or without biocide. Therefore, we can assume that the biocide itself, had no impact on the backscatter from the generated waves. We can also see that the differences in the X-band frequency are higher, which is most likely due to the higher frequency used.

We can also see that as time passes, the difference in backscatter between the waves and no waves experiments in the left-side tanks (without biocide) decreases, meaning that there is wave dampening occurring within these tanks.

This decrease occurs within June after a few weeks of the experiment beginning. Using the temperature loggers within the polytunnel, we collected water temperature readings every 2 hours for the duration of our experiments. This was used to understand how productive natural tanks could be when microbes began to colonise it. Figure 4.4. shows the temperature readings from the beginning of the first measurement campaign, April 26th, through to the end, 26th July.

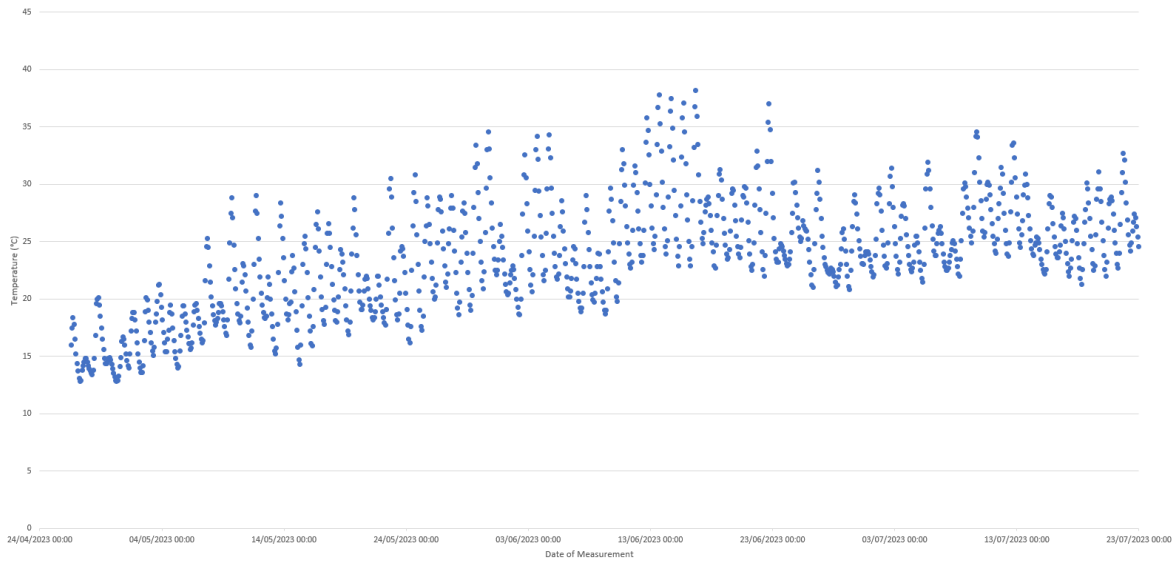

Figure 4.4 Water temperature profile from within the polytunnel experiments. Temperature readings taken from April 26th 2023 – July 26th 2023.

From Figure 4.4. we can see that when the experiment began in late April, we had an average water temperature of approximately 18.5°C. During May, we see an

increase in temperature, with an average of 21.1°C across the month, and this trend continues into June and July, where the water temperature is 25.8°C on average for both months. Microbes are highly sensitive to temperature, with warming generally raising microbial activity. It has been found that the higher the water temperature, the faster microbial biofilm development initiates and grows (Ahmad, et al., 2021).

4.3.3 Campaign 2: Backscatter Results and Temperature Profile

Once it was seen that the natural tanks had backscatter changes over time, we reset the experiment under the same conditions. To gain confidence that the positioning of the tanks was not having an effect on the backscatter values, we decided to position the natural tanks on the right-side of the polytunnel and the biocide tanks on the left-side of the polytunnel during campaign 2. This, however, was the only change made in the experiment setup, as every other detail remained the same.

During campaign 2, we increased our rate of measurements, allowing for a more detailed insight into how quickly waves could be dampened within the natural tanks. The differences between the measurements of each tanks can be seen in Table 4.3.

Table 4.3 Differences of mean backscatter between fan and no fan measurements; biocide tanks (left), natural tanks (right).

		Bands			
Date of Acquisition	Tank Position	L	C	X	Broadband
05-Sep-23	Back Left	2.35	2.57	2.6	2.56
	Back Right	2.45	2.6	2.68	2.57
	Front Left	2.47	2.62	2.65	2.6
	Front Right	2.31	2.5	2.53	2.52
07-Sep-23	Back Left	2.51	2.65	2.72	2.61
	Back Right	2.42	2.73	2.77	2.62
	Front Left	2.45	2.7	2.73	2.61
	Front Right	2.39	2.49	2.54	2.52
11-Sep-23	Back Left	2.25	2.33	2.38	2.37
	Back Right	2.39	2.47	2.5	2.62
	Front Left	2.55	2.61	2.68	2.63
	Front Right	2.42	2.55	2.57	2.58

13-Sep-23	Back Left	2.53	2.7	2.74	2.64
	Back Right	2.67	2.81	2.84	2.75
	Front Left	2.47	2.64	2.69	2.64
	Front Right	2.58	2.81	2.85	2.79
15-Sep-23	Back Left	2.45	2.56	2.55	2.58
	Back Right	2.38	2.66	2.68	2.56
	Front Left	2.37	2.57	2.62	2.59
	Front Right	2.59	2.67	2.7	2.63
18-Sep-23	Back Left	2.51	2.57	2.63	2.61
	Back Right	2.45	2.52	2.53	2.53
	Front Left	2.47	2.52	2.57	2.63
	Front Right	2.38	2.44	2.49	2.56
22-Sep-23	Back Left	2.3	2.56	2.6	2.46
	Back Right	2.32	2.44	2.48	2.45
	Front Left	2.21	2.57	2.59	2.49
	Front Right	2.35	2.53	2.58	2.52
25-Sep-23	Back Left	2.46	2.58	2.61	2.53
	Back Right	2.12	2.32	2.35	2.31
	Front Left	2.37	2.54	2.59	2.51
	Front Right	2.38	2.43	2.47	2.47
27-Sep-23	Back Left	2.29	2.73	2.71	2.51
	Back Right	2.05	2.16	2.29	2.26
	Front Left	2.31	2.62	2.42	2.52
	Front Right	2.27	2.36	2.44	2.41
29-Sep-23	Back Left	2.11	2.75	2.87	2.5
	Back Right	2.01	2.13	2.23	2.18
	Front Left	2.35	2.51	2.46	2.53
	Front Right	2.26	2.33	2.38	2.35
02-Oct-23	Back Left	2.08	2.79	2.85	2.53

	Back Right	2.02	2.08	2.19	2.12
	Front Left	2.36	2.58	2.5	2.49
	Front Right	2.12	2.26	2.33	2.28
10-Oct-23	Back Left	2.43	2.8	2.81	2.61
	Back Right	1.95	2.01	2.07	2.04
	Front Left	2.41	2.56	2.52	2.57
	Front Right	2.01	2.12	2.2	2.16
13-Oct-23	Back Left	2.35	2.74	2.8	2.63
	Back Right	1.96	2	2.07	2.03
	Front Left	2.41	2.53	2.47	2.54
	Front Right	2	2.12	2.18	2.14
23-Oct-23	Back Left	2.22	2.79	2.83	2.65
	Back Right	1.86	1.97	1.99	1.98
	Front Left	2.39	2.57	2.5	2.59
	Front Right	1.94	2.06	2.11	2.09
02-Nov-23	Back Left	2.43	2.75	2.8	2.63
	Back Right	1.83	1.95	1.98	1.98
	Front Left	2.33	2.6	2.47	2.55
	Front Right	1.95	2.04	2.09	2.07
06-Nov-23	Back Left	2.37	2.77	2.81	2.65
	Back Right	1.83	1.94	1.97	1.96
	Front Left	2.39	2.58	2.51	2.54
	Front Right	1.94	2.03	2.08	2.06

Table 4.3. shows the differences between the measurements of each tank when there were waves generated and when there were no waves. We can see at the beginning of the measurement campaign that the difference between waves vs no waves was similar between all tanks, and also similar to that of campaign 1. We can see again that the differences in X-band frequency measurements tend to be higher than our lower frequency C- and L- band measurements.

Due to the more frequent measurements taken during campaign 2, we can begin to see when the changes in backscattering occur within our natural tanks. From Table 4.3. we observe that these appear to begin from the 15th or 18th September. From these dates, we can see that the backscattering difference within the natural tanks (located on the right side of the polytunnel), begins to lower consistently as time passes, reaching the lowest value of 1.94 dB and 1.97 dB on November 6th. Once again, we can see the same end result as measurement campaign 1, the differences in backscatter between the biocide tanks and the natural tanks changes over time, with the natural tanks having a decrease in difference over time. This shows that there is some dampening occurring in both campaigns.

Once again, we can look at the temperature profile during this time to understand what the productivity of microbes could be during these measurements.

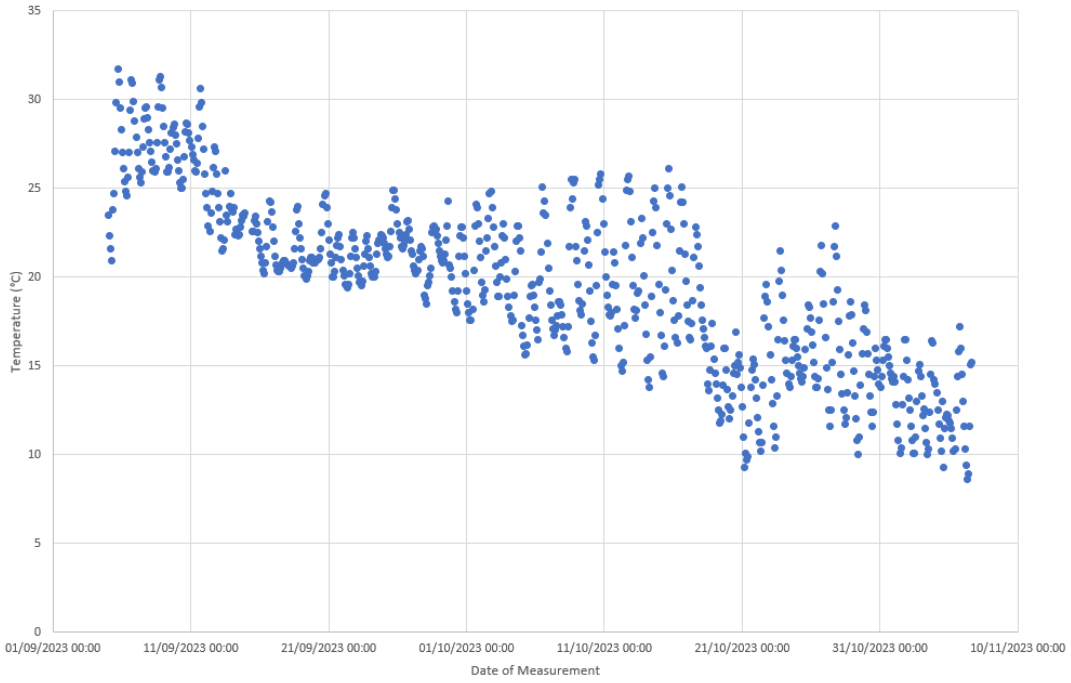

Figure 4.5 Water temperature profile from within the polytunnel experiments. Temperature readings taken from September 5th 2023 – November 6th 2023.

From Figure 4.5. we can see that when the 2nd measurement campaign began in late September, we had an average water temperature during the month of 23.5°C. During October, we see a decline in temperature, with an average of 17.7°C across the month, and this trend continues into the beginning of November, where our mean temperatures were averaging 12.6°C. We can see that as temperatures continued to

decrease, our differences found in our natural tanks also began to plateau in our late October – early November measurements.

4.3.4 Campaign 1: Statistical Analysis

We then applied our rigorous statistical test as described in our methodologies to both our campaign datasets (Table 4.2. and Table 4.3.).

This statistical test was applied to all experiment cases that were undertaken over the test campaigns. From this, tables were then created showing if the statistical differences were or were not found in all the experiments that were undertaken.

The results from Table 4.4. indicate that statistically significant differences were found within our data as the length of the experiment increased. On our first and second acquisitions, we see that there are no significant differences found within our dataset. However, from the June 5th, 2023, measurement onwards, we always find a significant difference within the DotD between our biocide tank reference (Front Right) and our test natural tanks (Front Left and Back Left). We can also see that for our reference vs control test that significant differences are less common.

Table 4.4 Results of statistical analysis undertaken on 1st campaign. Values filling the table are the results of the DotD from Table 4.2. Any value in green shows that the alternative hypothesis was fulfilled; any value in orange shows that the null hypothesis was fulfilled. Front right vs back right measurement is highlighted as our control measurement

Date of Acquisition	Tank Test	L	C	X	Broadband
26-Apr-23	Front Right vs Front Left	0.09	0.09	0.07	0.1
	Front Right vs Back Right	0.21	0.11	0.11	0.07
	Front Right vs Back Left	0.37	0.33	0.31	0.36
03-May-23	Front Right vs Front Left	0.09	0.15	0.09	0.11
	Front Right vs Back Right	0.14	0.21	0.05	0.12
	Front Right vs Back Left	-0.06	-0.02	-0.19	-0.08
05-Jun-23	Front Right vs Front Left	1.13	1.24	0.73	0.92
	Front Right vs Back Right	-0.11	0.03	-0.11	-0.08
	Front Right vs Back Left	0.66	0.73	0.78	0.74
15-Jun-23	Front Right vs Front Left	1.3	1.31	1.78	1.58
	Front Right vs Back Right	0.37	0.33	0.83	0.65
	Front Right vs Back Left	1.31	1.16	1.7	1.53
23-Jun-23	Front Right vs Front Left	1.9	1.93	1.76	1.81

	Front Right vs Back Right	0.05	0.03	0.08	0.12
	Front Right vs Back Left	1.73	1.73	1.79	1.79
28-Jun-23	Front Right vs Front Left	2.04	2.11	1.45	1.75
	Front Right vs Back Right	-0.02	0.1	-0.26	-0.11
	Front Right vs Back Left	1.61	1.64	1.84	1.71
12-Jul-23	Front Right vs Front Left	2.04	2.06	2.22	2.17
	Front Right vs Back Right	0.12	0.04	0.48	0.46
	Front Right vs Back Left	2.18	2.26	3	2.61
26-Jul-23	Front Right vs Front Left	0.84	0.9	1.68	1.16
	Front Right vs Back Right	-0.29	-0.26	0.54	0.03
	Front Right vs Back Left	0.92	0.67	1.95	1.21

4.3.5 Campaign 2: Statistical Analysis

The same statistical testing was conducted over our campaign 2 measurements. From Table 4.5. we can see from our more frequent measurements that it takes approximately 1.5 – 2 weeks before our statistical test begins showing significant differences. Here, we find significant differences between our biocide reference tank (Front Left) and our test natural tanks (Front Right and Back Right) from September 25th 2023 onward, with far less significant differences found within our control test (Front Left vs Back Left). This is due to the biocide tanks having a consistent backscatter measurement, as there is no microbial surfactants available to interact and dampen the waves within these tanks. However, within our test tanks, the dampening will continue to change the difference between Waves and No Waves experiments and will cause the DotD to keep changing.

Table 4.5 Results of statistical analysis undertaken on 2nd campaign. Values filling the table are the results of the DotD from Table 4.3. Any value in green shows that the alternative hypothesis was fulfilled; any value in orange shows that the null hypothesis was fulfilled. Front right vs back right measurement is highlighted as our control measurement.

			Bands		
Date of Acquisition	Tank Test	L	C	X	Broadband
05-Sep-23	Front Left vs Front Right	0.16	0.12	0.12	0.08
	Front Left vs Back Right	0.02	0.02	-0.03	0.03
	Front Left vs Back Left	0.12	0.05	0.05	0.04
07-Sep-23	Front Left vs Front Right	0.06	0.21	0.19	0.09

	Front Left vs Back Right	0.03	-0.03	-0.04	-0.01
	Front Left vs Back Left	-0.06	0.05	0.01	0
11-Sep-23	Front Left vs Front Right	0.13	0.06	0.11	0.05
	Front Left vs Back Right	0.16	0.14	0.18	0.01
	Front Left vs Back Left	0.3	0.28	0.3	0.06
13-Sep-23	Front Left vs Front Right	-0.11	0.17	0.16	-0.04
	Front Left vs Back Right	-0.2	0.17	0.15	-0.03
	Front Left vs Back Left	-0.06	-0.06	-0.05	-0.07
15-Sep-23	Front Left vs Front Right	-0.22	-0.1	-0.08	-0.04
	Front Left vs Back Right	-0.01	-0.09	-0.06	0.03
	Front Left vs Back Left	-0.08	0.01	0.07	0.01
18-Sep-23	Front Left vs Front Right	0.09	0.08	0.08	0.07
	Front Left vs Back Right	0.02	0	0.04	0.1
	Front Left vs Back Left	-0.04	-0.05	-0.06	0.02
22-Sep-23	Front Left vs Front Right	-0.14	0.04	0.01	-0.03
	Front Left vs Back Right	-0.11	0.13	0.11	0.04
	Front Left vs Back Left	-0.09	0.01	-0.01	0.03
25-Sep-23	Front Left vs Front Right	-0.01	0.11	0.12	0.04
	Front Left vs Back Right	0.25	0.22	0.24	0.2
	Front Left vs Back Left	-0.09	-0.04	-0.02	-0.02
27-Sep-23	Front Left vs Front Right	0.04	0.26	-0.02	0.11
	Front Left vs Back Right	0.26	0.46	0.13	0.26
	Front Left vs Back Left	0.02	-0.11	-0.29	0.01
29-Sep-23	Front Left vs Front Right	0.09	0.18	0.08	0.18
	Front Left vs Back Right	0.34	0.38	0.23	0.35
	Front Left vs Back Left	0.24	-0.24	-0.41	0.03
02-Oct-23	Front Left vs Front Right	0.24	0.32	0.17	0.21
	Front Left vs Back Right	0.34	0.5	0.31	0.37
	Front Left vs Back Left	0.24	-0.21	-0.35	-0.04
10-Oct-23	Front Left vs Front Right	0.4	0.44	0.32	0.41
	Front Left vs Back Right	0.46	0.55	0.45	0.53
	Front Left vs Back Left	-0.02	-0.24	-0.29	-0.04
13-Oct-23	Front Left vs Front Right	0.41	0.41	0.29	0.4
	Front Left vs Back Right	0.45	0.53	0.4	0.61

	Front Left vs Back Left	0.06	-0.21	-0.33	-0.06
23-Oct-23	Front Left vs Front Right	0.45	0.51	0.39	0.5
	Front Left vs Back Right	0.53	0.6	0.51	0.61
	Front Left vs Back Left	0.17	-0.22	-0.33	-0.06
02-Nov-23	Front Left vs Front Right	0.38	0.56	0.38	0.48
	Front Left vs Back Right	0.5	0.65	0.49	0.57
	Front Left vs Back Left	-0.1	-0.15	-0.33	-0.08
06-Nov-23	Front Left vs Front Right	0.45	0.55	0.43	0.48
	Front Left vs Back Right	0.56	0.64	0.54	0.58
	Front Left vs Back Left	0.02	-0.19	-0.3	-0.11

4.4 DISCUSSION

4.4.1 Initial Backscatter Analysis:

Upon inspection of our backscattering data, it was clear that the mean backscattering difference between waves generated and no waves within our natural test tanks was decreasing over time.

This can be explained through the microbial production that occurs within the natural tanks. Within both campaigns, water temperatures within the tanks were quite high, providing an environment for increased production within microbes (Ahmad, et al., 2021). Increased microbial production will result in an increase of biological surfactants from these microbes, this subsequently increases the effects of wave dampening from the biological surfactants produced. It has been seen that increased seawater temperatures can enhance the metabolism and influence biofilm parameters so that biofilms are much thicker in warmer waters (de Deckker, 2022). A note to be made is that while dampening was occurring within our experiment tanks, we believe that there would be a minimum dampening that could occur. This is due to the potential limited nutrients available to the microbial community over the duration of the experiment, we expect a limit of production to be reached in time.

Both measurements campaigns (shown in Table 4.2. and Table 4.3.), showed that as time increases, the difference in backscatter between waves generated and no wave acquisitions decreased over time, further showing that a dampening effect was taking place within our tanks. We can see in nearly all test cases that X-band

acquisitions showed greater differences in backscattering between these measurements when compared to those found in L- and C-band. We believe that this is due to the higher X-band frequency having a smaller wavelength when compared with the lower frequency C-band. From the frequency ranges swept in X- (9 – 10 GHz), C- (5 – 6 GHz), and L- band (1 – 2 GHz) we should have wavelengths of approximately 3 cm and 5.5 cm and 20cm respectively. The smallest capillary waves generated on our water surface may only be approximately 1 – 2 cm, which could be detected within X-band and therefore create a higher backscatter of our signal, but they would indeed be small for C- and too small for L-band.

4.4.2 Temperature Profile Comparison to Worlds Oceans

To extrapolate microbial production rates into real world scenarios, we can compare our water temperature measurements to those found throughout world's oceans. It has been shown that parts of the western Pacific Ocean and eastern Indian Ocean can remain at temperatures > 28 °C with high productivity from microbes due to this raised temperature (de Deckker, 2022). Other parts of the Indian Ocean, such as the Gulf of Mannar, have also seen sea surface temperatures reach 29.85 ± 0.44 °C (Mondal & Lee, 2022). The north Atlantic Ocean has seen record temperatures of 24.81 °C (European Commission: Copernicus, 2023) in September 2022 and global average sea surface temperatures have been a record high of 20.98 °C in 2023 (European Commission: Copernicus, 2023).

Our water temperature readings from our experiments showed that the average temperatures in April, May, and June and July were 18.5 °C, 21.1 °C, and 25.8 °C respectively. It should be noted that while our water temperature readings are around the values you can find in warmer oceans, we had peaks of 38 °C, which is just above the world record extreme for sea surface temperature, measured at 37.6 °C in the Arabian / Persian Gulf (Alosairi, et al., 2020).

4.4.3 Statistical Analysis of Both Campaign Data

Our statistical analysis showed in both campaigns that earlier measurements of all 4 tanks were not statistically different from each other. This is due to the first measurement being acquired from the first day of experiment set-up, where no surfactants / microbial activity would be present within our tanks. However, we can

see that as time passes, statistically significant differences are found between our test tanks and control tanks. In the first campaign this is within the first 3 measurements, however, it should be noted that these measurements were spread within > 1 month time span in warm temperatures, as seen in Figure 4.4. From the June 5th 2023 measurement onward, we can see that all measurements between the control Front Right tank and the experiment Front Left and Back Left tanks were significantly different from each other. We hypothesise that this is due to microbial production within our experiment tanks causing a build-up of surfactants, which accumulated, could dampen the short capillary waves generated by our fan (Sun, et al., 2023). In the 2nd measurement campaign, we found that a significant difference was found from the 25th September 2023 – 06th November 2023. This means that a dampening effect was occurring after approximately 20 days. However, we will comment on the applications of this dampening effect below.

4.4.4 Extrapolation to Satellite Data

Radar has been extensively utilized in the monitoring of anthropogenic oil spill detection (Fiscella, et al., 2000) and biogenic oil detection (Gade, et al., 1998). While the use of Synthetic Aperture Radar (SAR) has been utilized in research to try and detect marine plastic pollution from space (Simpson, et al., 2022), lab experiments have shown that difficulties in detection could occur within the open ocean due to more dispersed concentrations of macro-plastics and other contributing factors from the SAR scene that could potentially mask the signal of plastics (Simpson, et al., 2023) (Da Costa, et al., 2023). Due to the large concentrations of plastic found within the water column of the oceans gyres (Eriksen, et al., 2013) (Law, et al., 2010), and microbial communities found on these plastics (Bryant, et al., 2016), we hypothesize that the use of plastisphere-based surfactant dampening could be utilized as a proxy for marine plastic pollution monitoring. Surfactants have already been monitored within the ocean gyres using SAR satellite imaging, with these being potentially related to marine plastic pollution (Simpson, et al., 2021) and we believe our study strengthens that possibility that this could be used in future as a monitoring strategy.

There are some points to raise about the extrapolation of our data to a real-world satellite usage. Firstly, our tanks were filled with 30cm water and are 180 x 120 cm large, making the surface area of plastic in contact with water 39,600cm. This makes

our piece of plastic considerably larger than most items found within the ocean environment (Zeri, et al., 2018). Secondly, a large fraction of buoyant surface plastics are missing, with estimated inputs being vastly larger than what appears to be on the surface of the ocean (Lebreton, et al., 2019) (Cozar, et al., 2014), with theories suggesting that biofouling could cause plastic polymers sink from ocean surface waters, with longevity estimates of the plastics ranging between 17 – 66 days dependent on thickness of the plastic (Fazey & Ryan, 2016). While this could limit direct satellite detection of plastic litter, biofouling and the released surfactants could still be used as an indicator of traces of where plastic has been moving or circulating throughout the ocean. Fourthly, we mentioned earlier that productivity in our experiment tanks would be limited by a lack of nutrients over time. This may not be the case in the open ocean, where plastic marine debris in oligotrophic subtropical gyres could potentially provide a nutritional benefit for hitchhiker microbes on the debris, and could actually stimulate gross production of the attached community (Zhao, et al., 2021).

Chapter 5: General Discussion and Conclusion

Radar remote sensing provides a key tool in monitoring the marine plastic pollution issue. It is considered an important instrument for creating a multi-modal system that can monitor the global marine plastic pollution problem. A multi-modal system in this case, being a system that utilises multiple sensors different imaging techniques and wavelengths. SAR systems abilities to acquire data without disturbance from solar radiation and during nearly all-weather conditions is a key benefit and input into this multi-modal system, as passive sensors in a multi-modal system can be obstructed by cloud cover and lighting conditions. In this context, understanding the capabilities of SAR data for monitoring plastic pollution is essential.

This thesis contributes to the current state of the art knowledge and methods for marine plastic pollution using a mix of radar data, from both SAR and ground radar systems. This section will discuss the contributions from this thesis focussing specifically on two portions:

a) A synthesis of the key findings from this thesis and the connections with existing literature.

b) Future research recommendations.

5.1 SYNTHESIS OF FINDINGS AND RELATION TO LITERATURE

An important finding of this thesis is that marine plastic debris build-ups can be monitored from multitemporal SAR data. Chapter two shows that C-band SAR acquisitions from Sentinel-1 can be used to detect plastic islands within river environments. This is primarily due to the change in backscatter response between clean / clear water and when the material is apparent on the surface. It has been shown that the use of detectors can also be implemented on this SAR data to identify these

islands of marine debris, and subsequently, a temporal analysis can be made to identify hotspots of debris accumulation throughout a set timescale. It was also shown that change detection systems that utilise the coherent data from SLC SAR data performed better compared to those that do not utilise this information. Furthermore, it was found that the cross-pol VH channel provided better detection than the co-pol VV channel.

It is important to mention that before this work began, only a limited number of studies had implemented the use of SAR remote sensing for monitoring marine plastic pollution. However, the increase in backscatter seen from marine plastic debris follows a similar signature from other studies, whether this be explicit target plastics (Serafino & Bianco, 2021; Topouzelis, et al., 2019), single pieces of floating macroplastics (Felicio, et al., 2024) or debris patches in open water (Arii, et al., 2014). In these studies, increases of backscatter are seen from plastic targets or material on the water surface. This coincides with what you would expect from other surface materials, be it floating vegetation (Canisius, et al., 2019), or wood debris (Arii, et al., 2014). However, it should be noted that in Topouzelis et al (2019), a dampening effect from large plastic targets is expected on capillary waves, resulting in a decrease of backscatter in higher wind conditions. Regarding the classification accuracies, again there are limited studies on the detection of marine litter using purely SAR data. As such, this chapter is, to the best of our knowledge, one of the first times that evidence is provided on the capabilities of SAR to monitor and detect a real-world case scenario of marine debris. These classification accuracies are also on similar or greater levels than those conducted on optical data (Biermann, et al., 2020; Garcia-Garin, et al., 2021; Basu, et al., 2021). Thus, an important outcome of this chapter was the understanding that multitemporal SAR images can be used to detect and monitor marine debris accumulations in riverine areas.

It should be noted however, that the work in chapter two is limited in its scope since the marine debris within the SAR imagery cannot be classified further into separate categories. That is, plastic debris within the accumulation cannot be separated from wood or other material debris for classification. This means that this approach cannot be utilised to accurately detect in locations without ground validation confirming the debris class. This separation of marine debris classes has already seen investigation in the optical spectra (Hu, 2022; Ciappa, 2021; Ciappa, 2022). However, mixed pixels can cause issues within optical data and reliable results have been seen

to be obtained from pixels that are filled with more than 25% floating matter (Ciappa, 2022). Also, while the detection was indeed done on a real-world accumulation of marine debris, the debris was held stationary by the dams within the river system. This causes a somewhat unrealistic accumulation for ocean detection cases, as free-floating debris in the ocean will rarely be held stationary, and may be composed of less debris items / concentration. Within the ocean itself, there are much more complicated dynamics and interactions with plastic debris that make direct detection particularly challenging with SAR (Martinez-Vicente, et al., 2019).

Within chapter three, these mechanisms of direct plastic debris detection have been explored. To our understanding, the measurement campaigns undertaken in chapter three are the most extensive to date for understanding the mechanisms of plastic detection in radar and for understanding the item types and concentrations that are detectable within radar data. The theoretical scattering model proposed within this chapter is, to our knowledge, the first time these mechanisms have been fully explored and tested in these means. Chapter three showed that backscatter differences within radar data were detectable between a) reference acquisitions of simulated ocean waves and b) test acquisitions of the same simulated waves with plastic items moving through the water. These differences were found in both C- and X-band frequencies, with X-band performing significantly better than the C-band frequency, based on number of detectable backscatter differences in all test cases measured.

Chapter three agrees well with the findings from chapter two regarding backscatter increases from marine debris, where all cases of a detection within our acquisitions was seen as a backscatter increase from the debris. However, the hypotheses for scattering mechanisms which result in increased backscatter are more explored and tested within chapter three. The mechanisms proposed in chapter three have also been explored in other studies from separate research data collected during these measurement campaigns. Felicio et al. (2024) also found that ‘indentation’ scattering played an important contribution into the scattering mechanisms of plastic debris on water. Whereas Gonga et al. (2023) found marine litter wave dampening and capillary wave effects played the most important role in GNSS-R measurements of plastic debris. Felicio et al (2024) also finds that the X-band frequency significantly improves detection capabilities for marine debris detection.

A limitation of the work done in chapter three is the lack of quad-polarimetric X-band data. In our C-band data from the first campaign, there is no significant effect of polarisation on whether detection is capable with differing plastic materials. C-band performed poorly in the second campaign and with only 2 cases of detection over all experiments, we could not analyse the effect of polarisation on detection of these materials. It has previously been observed that VV polarisation in Sentinel-1 data (C-band) can be used for monitoring and detecting plastic targets (Topouzelis et al, 2019; Simpson et al, 2022). Results in X-band are limited. Felicio et al (2024) found that VV polarisation in X-band resulted in a larger backscatter response than VH and HH polarisations. However, all polarisations presented backscattering values above the threshold for detection.

A key finding from chapter three is that as wave height increases, detection of small plastics targets decreases. This is found throughout the literature, whether this be with satellite data or ground radars (Martinez-Vicente, et al., 2019; Felicio, et al., 2024; Gonga, et al., 2023; Serafino & Bianco, 2021). The experiment conducted in chapter three used irregular deep-water waves to simulate ocean conditions, where it was found that at 17cm wave heights, difficulties in detecting plastic items were consistently found. In the open ocean, where wave dynamics produce higher wave heights and breaking waves are more common, this means that debris detection is particularly challenging. Spatial resolution from freely available SAR satellites also means, at present time, that detection of smaller debris is practically impossible in the open ocean, and that focusses must be on larger debris accumulations. However, very high resolution X-band satellites, such as ICEYE, may prove to be a valid option for debris detection in future.

Chapter four provides insight into the potential usage of a proxy for marine plastic debris monitoring within the ocean. As seen above, if debris detection is particularly challenging within the natural ocean environment, then a proxy may be the best way to monitor the plastic problem at present time. Evans & Ruf, (2022) used CYGNSS GNSS-R data to measure the ocean roughness, characterised by the mean square slope (MSS). They found a significant correlation between modelled microplastic concentrations and the degree of suppression on roughness. The authors were unsure if the roughening suppression was due to the presence of microplastics themselves or surfactants from related to them. Sun, et al., (2023) studied the separate

effects of microplastics and surfactants on wave dampening in a wind-wave tank facility. They found that dampening of capillary waves from microplastic particles themselves would only occur at much higher concentrations and surface area coverage than what is realistically found within the ocean. Whereas surfactants dampened both mechanically generated and wind-driven capillary waves significantly more. This is worth noting for future observations of the marine plastics, where dampening of waves within the ocean, from plastic alone, may only occur when there are extremely large quantities on the surface of the water. Davaasuren, et al., (2018) and Simpson et al., (2021) have investigated slicks within Sentinel-1, TerraSAR-X and COSMO-SkyMed SAR images acquired over the North Atlantic, North Pacific and Indian Ocean gyres, where it was found using wind speed analysis that these slicks are indeed surfactants. Chlorophyll-a analysis was also conducted to understand if these were due to an algal bloom biogenic means, where it was found that there were very low chl-a concentrations and algal blooms were ruled out as a culprit. Both investigations by Davaasuren et al (2018) and Simpson et al (2021) identified plastisphere-based surfactants as a potential culprit, with future studies needed to understand if plastisphere-based surfactants are indeed capable of dampening waves in radar acquisitions. Chapter four has provided evidence that the plastisphere-based surfactants generated from our experiments are indeed capable of a significant dampening in radar backscatter.

A limitation of chapter four is the lack of different plastic concentrations / surface area for understanding differences in surfactant production. As explained in chapter four, the surface area of the plastic tanks used in our experiment are considerably larger than most items found within the ocean. A higher surface area will provide more of a surface for microbial activity, and therefore surfactant production. The use of smaller surface area tanks, or another experiment design utilising multiple smaller plastic items could provide more details on surfactant production and dampening capabilities.

5.2 FUTURE WORK

Some possible future focusses for research can be conceived from the findings of this thesis, and from the findings of current literature within the field. In terms of marine debris detection with SAR, a common point in literature is the impossibility to derive differing marine litter types based purely on their backscatter values. That is, if

there was a large patch of marine debris in the open ocean, or similarly a large build-up of marine debris in river systems, such as in Chapter 2, is there a way to derive separate material classes from each other using purely backscatter values and / or polarimetric information? There is currently a lack of literature regarding this (Waqas, et al., 2023), where at present, most studies that classify marine debris with SAR, can only do so with explicit prior knowledge or by using combined optical and SAR imagery in tandem to cross validate (Savastano, et al., 2021). Therefore, insights into the backscatter and polarimetric characteristics of differing marine debris class types would be of great use. This has been partially explored in Chapter 3 regarding the differing plastic types and objects, however, a similar scale study using different materials (wood, rubber, glass, metal) could help understand if there are ways to distinguish these from one another in SAR imagery. Utilising a ground-radar sensor, similar to the one used in Chapter 3, could help provide this information regarding other floating marine debris. Backscatter and detection thresholding information from this future research could provide the foundations for a SAR marine debris database which provides information on detection capabilities for debris classes and concentrations, in differing ocean conditions. Other future research should involve insights into how differing accumulation densities change the SAR signal. Polarimetric decompositions, such as Cloude-Pottier (Cloude & Pottier, 1996), Yamaguchi (Yamaguchi, et al., 2005) and more, could be implemented and used for density /classification. This work could be implemented on real-world test cases, such as those found in Chapter 2, or could be done using targets similar to those used in the Plastic Litter Project, seen in Topouzelis et al., (2020).

More research into finding the most suitable polarisation for marine litter detection is also needed. While this has been explored in Chapter 2 regarding the analysis of VV and VH channels for detectors, and partially in Chapter 3 for C-band data with plastic pollution, more information is needed on the use of polarimetric data for distinguishing litter types. Polarimetric analysis on plastic litter has also been conducted in Felicio, et al., (2024) where it was found in ultra-wideband (UWB) frequency that VV polarisation has a larger response than VH and HH for plastic litter detection, however, all channels provided values above the threshold for detection on the litter monitored. A polarimetric analysis on some refined frequency ranges could provide extremely useful for future detection of marine debris. It has already been seen

that the X-band frequency (Simpson, et al., 2023) and Ku frequency (Felicio, et al., 2024) appear to be most prominent for detection of plastic debris. Therefore, a full polarimetric analysis on these bands could provide useful information for potential sensor usage in future for marine debris detection. Polarimetric analysis can also be conducted on the other material classes listed above for backscatter analysis. This can be done in a lab setting, using marine debris in still water and including wave conditions, as well as in real world scenarios if access to quad-pol SAR data was available.

In Chapter 4, plastisphere-based surfactants wave dampening was shown to alter backscatter in radar data. Future work should consider similar experiments using different materials, particularly wood, which have been shown to develop biofilms too (Wright, et al., 2020). An analysis on the dampening properties from biofilms from other materials could potentially give insight into the use of surfactants to identify more classes of marine debris, and possibly classify based on these in future. An analysis on the dampening effects could potentially help give an understanding of distinguishing which items / concentrations are capable of being detected in radar data. The use of 'real' (i.e. sampled marine plastics) in a wave-tank experiment similar to chapter 3, with the inclusion of surfactants and biofilms, could also prove valuable in understanding what is capable in more 'real-world' scenarios with moving waves.

5.3 SUMMARY AND CONCLUDING REMARKS

Marine debris, particularly marine plastic debris, is a global problem which threatens ocean and marine species health, as well as human health through food safety and quality concerns. The use of remote sensing to monitor marine plastic debris is still a relatively new field, with investigations into the available technologies ongoing. A multi-modal system of detection has been highlighted as key for overcoming the challenge of marine debris detection. SAR imagery, whether through current freely available data from the Copernicus Programme or future missions, could make an important contribution to this process. The radar and SAR monitoring applications presented within this thesis have shown how radar data can be utilised to detect and monitor marine plastic debris. Whether this is through direct detection in lab-based or real-world scenarios, or through the use of a proxy by utilising the plastisphere. Although more work needs to be carried out, the use of SAR could contribute to global

efforts aimed at managing marine plastic pollution, and offer value insights in future for distribution patters, accumulation zones, and transport pathways.

Bibliography

Abe, T., Yamaguchi, Y. & Sengoku, M., 1990. Experimental study of microwave transmission in snowpack. *IEEE Trans. Geosci. Remote Sens.,* Volume 28, pp. 915-921.

Ahmad, J. I. et al., 2021. Changes in biofilm composition and microbial water quality in drinking water distribution systems by temperature increase induced through thermal energy recovery. *Environmental Research,* Volume 194, p. 110648.

Akbari, V. et al., 2016. Polarimetric SAR Change Detection with the Complex Hotelling-Lawley Trace Statistic. *IEEE Trans. Geosci. Remote Sens.,* Volume 54, pp. 3953-3966.

Akobeng, A., 2007. Understanding diagnostic tests 3: Receiver operating characters curves. *Acta Paediatr,* Volume 96, pp. 644-647.

Almroth, B. C. & Eggert, H., 2019. Marine Plastic Pollution: Sources, Impacts, and Policy Issues. *Review of Environmental Economics and Policy,* 13(2), pp. 317 - 326.

Alosairi, Y., Alsulaiman, N., Rashed, A. & Al-Houti, D., 2020. World record extreme sea surface temperatures in the northwestern Arabian/Persian Gulf verified by in situ measurements. *Mar Pollut Bull.,* 161(Pt B), p. 111766.

Alpers, W. & Espedal, H. A., 2004. Oils and Surfactants. In: *Synthetic Aperture Radar Marine User's Manual.* s.l.:s.n., pp. 263-276.

Alpers, W. R., Ross, D. B. & Rufenach, C. L., 1981. On the detectability of ocean surface waves by real and synthetic aperture radar.. *J. Geophys. Res. Atmos.,* Volume 86, pp. 6481-6498.

Alvarez-Vanhard, E., Corpetti, T. & Houet, T., 2021. UAV & satellite synergies for optical remote sensing applications: A literature review. *Science of Remote Sensing,* Volume 3, p. 100019.

Andrady, A. L., 2011. Microplastics in the marine environment.. *Mar. Pollut. Bull,* Volume 62, pp. 1596-1605.

Andriolo, U. et al., 2023. Drones for litter monitoring on coasts and rivers: suitable flight altitude and image resolution. *Marine Pollution Bulletin,* Volume 195, p. 115521.

Arii, M., Koiwa, M. & Aoki, Y., 2014. Applicability of SAR to Marine Debris Surveillance. *IEEE Journal of Selected Topics in Applied Earth Observations and Remote Sensing,* 7(5), pp. 1729 - 1744.

Bakir, A., Rowland, S. J. & Thompson, R. C., 2014. Enhanced desorption of persistent organic pollutants from microplastics under simulated physiological conditions. *Environ. Pollut.,* Volume 185, pp. 16 - 23.

Bamler, H. & Hartl, P., 1998. Synthetic Aperture Radar Interferometry.. *Inverse Probl,* Volume 14, pp. R1-R54.

Bao, Z. et al., 2018. Monitoring of Beach Litter by Automatic Interpretation of Unmanned Aerial Vehicle Images using the Segmentation Threshold Method. *Marine Pollution Bulletin,* Volume 137, pp. 388 - 398.

Barboza, L. G. A. et al., 2018. Marine Microplastic Debris: An Emerging Issue for Food Security, Food Safety and Human Health. *Mar. Pollut. Bull.,* Volume 133, pp. 336 - 348.

Barnes, D. K. A., Galgani, F., Thompson, R. C. & Barlaz, M., 2009. Accumulation and fragmentation of plastic debris in global environments. *Philos. Trans. R. Soc. Lond. B. Biol. Sci,* 364(1526), pp. 1985 - 1998.

Basto, M. N. et al., 2019. Plastic ingestion in aquatic birds in Portugal. *Marine Pollution Bulletin,* Volume 138, pp. 19 - 24.

Basu, B., Sannigrahi, S., Basu, A. S. & Pilla, F., 2021. Development of Novel Classification Algorithms for Detection of Floating Plastic Debris in Coastal Waterbodies Using Multispectral Sentinel-2 Remote Sensing Imagery.. *Remote Sens,* Volume 13, p. 1598.

Biermann, L., Clewley, D., Martinez-Vicente, V. & Topouzelis, K., 2020. Finding Plastic Patches in Coastal Waters Using Optical Satellite Data.. *Sci. Rep.,* Volume 10, p. 5346.

Borelle, S. B. et al., 2020. Predicted Growth in Plastic Waste Exceeds Efforts to Mitigate Plastic Pollution. *Science,* Volume 369, pp. 1515-1518.

Bouwmeester, H., Hollman, P. C. H. & Peters, R. J. B., 2015. Potential Health Impact of Environmentally Released Micro- and Nanoplastics in the Human Food Production Chain: Experiences from Nanotoxicology. *Environ. Sci. Technol.,* Volume 49, pp. 8932-8947.

Bouwmeester, H., Hollman, P. C. H. & Peters, R. J. B., 2015. Potential Health Impact of Environmentally Released Micro- and Nanoplastics in the Human Food Production Chain: Experiences from Nanotoxicology. *Environ. Sci. Technol,* 49 (15), pp. 8932 - 8947.

Brandon, J. A., Jones, W. & Ohman, M. D., 2019. Multidecadal increase in plastic particles in coastal ocean sediments. *Science Advances,* 5(9), p. eaax0587.

Brennecke, D. et al., 2016. Microplastics as vector for heavy metal contamination from the marine environment. *Estuar. Coast. Shelf. Sci.,* Volume 178, pp. 189 - 195.

Bryant, J. A. et al., 2016. Diversity and Activity of Communities Inhabiting Plastic Debris in the North Pacific Gyre. *mSystems,* 1(3), pp. e00024-16.

Bystrov, A., Wang, Y. & Gardner, P., 2022. Analysis of Vector Network Analyzer Thermal Drift Error. *Metrology,* 2(2), pp. 150-160.

Bystrov, A., Wang, Y. & Gardner, P., 2022. Analysis of Vector Network Analyzer Thermal Drift Error.. *Metrology,* Volume 2, pp. 150-160.

Campbell, J. B. & Wynne, R. H., 2011. *Introduction to Remote Sensing.* 5th ed. New York, USA: The Guilford Press.

Canisius, F. et al., 2019. SAR Backscatter and InSAR Coherence for Monitoring Wetland Extent, Flood Pulse and Vegetation: A Study of the Amazon Lowland. *Remote Sensing,* 11(6), p. 720.

Carson, H. S., Nerheim, M. S., Carroll, K. A. & Eriksen, M., 2013. The plastic-associated microorganisms of the North Pacific Gyre. *Marine Pollution Bulletin,* 75(1-2), pp. 126-132.

Cartraud, A. E., le Corre, M., Turquet, J. & Tourmetz, J., 2019. Plastic Ingestion in Seabirds of the Western Indian Ocean.. *Marine Pollution Bulletin,* Volume 140, pp. 308 - 314.

Cauwenberghe, L. V. et al., 2015. Microplastics in Sediments: A Review of Techniques, Occurrence and Effects. *Marine Environmental Research,* Volume 111, pp. 5 - 17.

Chatziantoniou, A. et al., 2021. Detection of Biogenic Oil Films near Aquaculture Sites Using Sentinel-1 and Sentinel-2 Satellite Images.. *Remote Sens.,* Volume 13, p. 1737.

Ciappa, A. C., 2021. Marine plastic litter detection offshore Hawai'i by Sentinel-2. *Marine Pollution Bulletin,* Volume 168, p. 112457.

Ciappa, A. C., 2022. Marine Litter Detection by Sentinel-2: A Case Study in North Adriatic (Summer 2020). *Remote Sensing,* 14(10), p. 2409.

Claessens, M. et al., 2011. Occurrence and distribution of microplastics in marine sediments along the Belgian coast. *Marine Pollution Bulletin,* 62(10), pp. 2199 - 2204.

Clarizia, M. P. et al., 2009. Analysis of GNSS-R Delay-Doppler Maps from the UK-DMC Satellite over the Ocean. *Geophysical Research Letters,* 36(2).

Cloude, S. R. & Pottier, E., 1996. A review of target decomposition theorems in radar polarimetry. *IEEE Transactions on Geoscience and Remote Sensing,* 34(2), pp. 498 - 518.

Cole, M. et al., 2013. Microplastic Ingestion by Zooplankton. *Environ. Sci. Terminol.* , Volume 47, pp. 6646-6655.

Constantini, M. et al., 2018. *Automatic Coregistration of SAR and optical images exploiting complementary geometry and mutual information.* Valencia, Spain, IGARSS IEEE International Geoscience and Remote Sensing Symposium.

Cozar, A., Echevarria, F., Gonzalez-Gordillo, J. I. & Duarte, C. M., 2014. Plastic debris in the open ocean. *Proc. Natl. Acad. Sci. U.S.A.,* 111(28), pp. 10239 - 10244.

Cracknell, A. P., 2017. UAVs: regulations and law enforcement. *International Journal of Remote Sensing,* 38(8 - 10), pp. 3054-3067.

Cumming , W. A., 1952. The Dielectric Properties of Ice and Snow at 3.2 Centimeters.. *J. Appl. Phys.,* Volume 23, p. 768.

Da Costa, T. S. et al., 2023. *Detection of Low Permittivity Floating Plastic Sheets at Microwave Frequencies.* Florence, s.n.

Davaasuren, N. et al., 2018. *Detecting Microplastics Pollution in World Oceans Using Sar Remote Sensing.* Valencia, IEEE.

de Deckker, P., 2016. The Indo-Pacific Warm Pool: critical to world oceanography and world climate. *Geoscience Letters,* Volume 3, p. 20.

de Deckker, P., 2022. The Indo-Pacific Warm Pool: critical to world oceanography and world climate. *Journal of Marine Science and Engineering,* Volume 3, p. 20.

de Fockert, A. & Baker, W., 2022. *Wave Damping by Marine Litter: Description Test Setup and Measurements Deltares. 11206446-000-HYE-0004. Deltares Internal Technical Note,* Delft, The Netherlands: Deltares.

Debroas, D., Mone, A. & Ter Halle, A., 2017. Plastics in the North Atlantic garbage patch: A boat-microbe for hitchhikers and plastic degraders. *Sci Total Environment,* Volume 599 - 600, pp. 1222 - 1232.

Derraik, J. G. B., 2002. The Pollution of the Marine Environment by Plastic Debris: A Review. *Mar. Pollut. Bull.,* Volume 44, pp. 842 - 852 .

Dris, R. et al., 2015. Beyond the Ocean: Contamination of Freshwater Ecosystems with (micro-)plastic particles.. *Environ. Chem,* Volume 12, pp. 539-550.

Eastman, R., Warren, S. G. & Hahn, C. J., 2011. Variations in Cloud Cover and Cloud Types over the Ocean from Surface Observations, 1954–2008. *Journal of Climate,* 24(22), pp. 5914 - 5934.

Emric, E., 2021. *Trash Fills Bosnia River Faster than Workers can Pull it Out, AP News.* [Online]
Available at: https://apnews.com/article/environment-serbia-hydroelectric-power-95866b7e3af63b9608218e89791df5d0
[Accessed 07 June 2022].

Eriksen, M. et al., 2023. A growing plastic smog, now estimated to be over 170 trillion plastic particles afloat in the world's oceans—Urgent solutions required. *PLoS ONE,* 18(3), p. e0281596.

Eriksen, M. et al., 2014. Plastic Pollution in the World's Oceans: More than 5 Trillion Plastic Pieces Weighing over 250,000 Tons Afloat at Sea. *PLoS ONE,* 9(12), p. e111913.

Eriksen, M. et al., 2013. Plastic pollution in the South Pacific subtropical gyre. *Marine Pollution Bulletin,* 68(1-2), pp. 71-76.

Ermakov, S. A., Kapustin, I., Sergievskava, I. & da Silva, J., 2015. *Spreading of Oil Films on the Sea Surface: Radar / Optical Observations and Physical Mechanisms.* Toulouse, France, SPIE Remote Sensing.

Ermakov, S. A. et al., 2019. *Satellite and In-situ Observations of a River Confluence Zone.* Strasbourg, France, Proceedings Volume 11150, Remote Sensing of the Ocean, Sea Ice, Coastal Waters and Large Water Regions 2015. 963807. SPIE Remote Sensing.

Erni-Cassola, G., Zadjelovic, V., Gibson, M. I. & Christie-Oleza, J. A., 2019. Distribution of plastic polymer types in the marine environment; A meta-analysis. *Journal of Hazardous Materials,* Volume 369, pp. 691-698.

Escobar-Sanchez, G., Haseler, M., Oppelt, N. & Schernewski, G., 2021. Efficiency of Aerial Drones for Macrolitter Monitoring on Baltic Sea Beaches. *Frontiers in Environmental Science,* Volume 8, p. 560237.

European Commission: Copernicus, 2023. *Global sea surface temperature reaches a record high.* [Online]
Available at: https://climate.copernicus.eu/global-sea-surface-temperature-reaches-record-high
[Accessed 22 November 2023].

European Commission: Copernicus, 2023. *Record high global sea surface temperatures continue in August.* [Online]
Available at: https://climate.copernicus.eu/record-high-global-sea-surface-temperatures-continue-august
[Accessed 22 November 2023].

European Space Agency, N/A. *Sentinel-1 SAR: Acquisition Modes: Interferometric Wide Swath.* [Online]
Available at: https://sentinels.copernicus.eu/web/sentinel/user-guides/sentinel-1-sar/acquisition-modes/interferometric-wide-swath
[Accessed 25 August 2022].

Evans, M. C. & Ruf, C. S., 2022. Toward the Detection and Imaging of Ocean Microplastics With a Spaceborne Radar. *IEEE Transactions on Geoscience and Remote Sensing,* Volume 60, pp. 1-9.

Evans, M. C. & Ruf, C. S., 2022. Toward the Detection and Imaging of Ocean Microplastics With a Spaceborne Radar. *IEEE Transactions on Geoscience and Remote Sensing,* Volume 60, pp. 1 - 9.

Fallati, L. et al., 2019. Anthropogenic Marine Debris assessment with Unmanned Aerial Vehicle imagery and deep learning: A case study along the beaches of the Republic of Maldives. *Science of the Total Environment,* Volume 693, p. 133581.

Fazey, F. M. & Ryan, P. G., 2016. Biofouling on buoyant marine plastics: An experimental study into the effect of size on surface longevity. *Environmental Pollution,* Volume 210, pp. 354 - 360.

Felicio, J. M. et al., 2024. Feasibility of Radar-based Detection of Floating Macroplastics at Microwave Frequencies. *IEEE Transactions on Antennas and Propagation ,* p. 1.

Fernandez, C. & Anastasopoulou, A., 2019. Plastic ingestion by blue shark Prionace glauca in the South Pacific Ocean (south of the Peruvian Sea). *Marine Pollution Bulletin,* Volume 149, p. 110501.

Ferrentino, E. et al., 2020. Multi-polarization and multi-temporal Sentinel-1 SAR imagery to analyze the variations in the water-body of reservoirs.. *IEEE J. Sel. Top. Appl. Earth Obs. Remote Sens.,* Volume 13, pp. 840-846.

Fiscella, B. et al., 2000. Oil spill detection using marine SAR images. *International Journal of Remote Sensing,* 21(18), pp. 3561-3566.

Foekama, E. M. et al., 2013. Plastic in North Sea Fish. *Environ. Sci. Technol,* 47(15), pp. 8818 - 8824.

Freitas, S., Silva, H. & Silva, E., 2021. Remote Hyperspectral Imaging Acquisition and Characterization for Marine Litter Detection. *Remote Sensing,* 13(13), p. 2536.

Gade, M. et al., 1998. Imaging of biogenic and anthropogenic ocean surface films by the multifrequency/multipolarization SIR-C/X-SAR. *Journal of Geophysical Research,* 103(C9), pp. 18851-18866.

Gade, M., Huhnerfuss, H. & Korenowski, G., 2006. *Marine Surface Films.* Berlin, Germany: Springer-Verlag.

Gago, J. et al., 2020. Ingestion of Plastic Debris (Macro and Micro) by Longnose Lancetfish (Alepisaurus ferox) in the North Atlantic Ocean.. *Regional Studies in Marine Science,* Volume 33, p. 100977.

Gall, S. C. & Thompson, R. C., 2015. The Impact of Debris on Marine Life. *Mar. Pollut. Bull.,* Volume 92, pp. 170-179.

Garaba, S. P. et al., 2018. Sensing Ocean Plastics with an Air-borne Hyperspectral Shortwave Infrared Imager.. *Environ. Sci. Technol. ,* Volume 52, pp. 11699-11707.

Garcia-Garin, O. et al., 2021. Automatic detection and quantification of floating marine macro-litter in aerial images: Introducing a novel deep learning approach connected to a web application in R.. *Environ. Pollut.,* Volume 273, p. 116490.

García-Regalado, A., Herrera, A. & Almeda, R., 2024. Microplastic and mesoplastic pollution in surface waters and beaches of the Canary Islands: A review. *Marine Pollution Bulletin,* Volume 201, p. 116230.

Geyer, R., Jambeck, J. R. & Law, K. L., 2017. Production, use, and fate of all plastics ever made. *Science Advances,* 3(7), p. e1700782.

Ge, Z. et al., 2016. Semi-automatic Recognition of Marine Debris on Beaches. *Scientific Reports,* Volume 6, p. 25759.

Goddijn-Murphy, L. & Williamson, B., 2019. On Thermal Infrared Remote Sensing of Plastic Pollution in Natural Waters. *Remote Sens,* Volume 11, p. 2159.

Goldstein, M. C., Titmus, A. J. & Ford, M., 2013. Scales of Spatial Heterogeneity of Plastic Marine Debris in the Northeast Pacific Ocean. *PLoS ONE,* 8(11), p. e80020.

Gomez, A. S., Scandolo, L. & Eisemann, E., 2022. A Learning Approach for River Debris Detection.. *Int. J. Appl. Earth Obs. Geoinf.,* Volume 107, p. 102682.

Goncalves, G. et al., 2022. Beach litter survey by drones: Mini-review and discussion of a potential standardization☆. *Environmental Pollution,* Volume 315, p. 120370.

Gonga, A. et al., 2023. GNSS-R Observations of Marine Plastic Litter in a Water Flume: An Experimental Study. *Remote Sensing,* 15(3), p. 637.

Grabowska, B. & Kasperski, J., 2020. The Thermal Conductivity of 3D Printed Plastic Insulation Materials - The Effect of Optimising the Regular Structure of Closures. *Materials,* 13(19), p. 4400.

Gregory, M. R., 2009. Environmental Implications of Plastic Debris in Marine Settings - Entanglement, Ingestion, Smothering, Hanger-ons, Hitch-hiking, and Alien Invasions. *Phil. Trans. R. Soc. B,* 364(1526), pp. 2013 - 2025.

Gundogdu, S., Cevik, C. & Karaca, S., 2017. Fouling Assemblage of Benthic Plastic Debris Collected from Mersin Bay, NE Levantine Coast of Turkey. *Marine Pollution Bulletin,* 124(1), pp. 147 - 154.

Hardesty, B. D. et al., 2016. *Understanding debris sources and transport from the coastal margin to the ocean,* Canberra, Australia: CSIRO: EP165651.

Hijmans, R. J., 2015. *Third Level Administrative Divisions, Bosnia and Herzegovina; Museum of Vertebrate Zoology.*. [Online]
Available at: https://geodata.lib.utexas.edu/catalog/stanford-xt594tq5034
[Accessed 12 August 2022].

Hijmans, R. J., N/A. *DIVA-GIS: Download Data by Country. DIVA-GIS.*. [Online]
Available at: https://www.diva-gis.org/Data
[Accessed 12 August 2022].

Hogg, D. & Vergunst, T., 2017. *Eunomia 2017 Final Report: A Comprehensive Assessment of the Current Waste Management Situation in South East Europe and Future Perspectives for the Sector Including Options for Regional Co-Operation in Recycling of Electric and Electronic Waste,* Luxembourg : European Union.

Howe, K. L. et al., 2018. Relative Abundance of Bacillus spp., Surfactant-associated Bacterium Present in a Natural Sea Slick Observed by Satellite SAR Imagery Over the Gulf of Mexico. *Elem Sci Anth,* Volume 6, pp. 1 - 8 .

Htun, M. T., 2012. Characterisation of High-density Polyethylene Using Laser-induced Fluorescence (LIF). *Journal of Polymer Research,* Volume 19, p. 9823.

Hu, C., 2021. Remote detection of marine debris using satellite observations in the visible and near infrared spectral range: Challenges and potentials. *Remote Sensing of Environment,* Volume 259, p. 112414.

Hu, C., 2021. Remote detection of marine debris using satellite observations in the visible and near infrared spectral range: Challenges and potentials.. *Remote. Sens. Environ. ,* Volume 259, p. 112414.

Hu, C., 2022. Remote detection of marine debris using Sentinel-2 imagery: A cautious note on spectral interpretations. *Marine Pollution Bulletin,* Volume 183, p. 114082.

Huhnerfuss, H. et al., 1981. The Damping of Ocean Surface Waves by a Monomolecular Film Measured by Wave Staffs and Microwave Radars. *Journal of Geophysical Research,* Volume 86, pp. 429 - 438.

Hühnerfuss, H. et al., 1981. The damping of ocean surface waves by a monomolecular film measured by wave staffs and microwave radars. *Journal of Geophysical Research,* 86(C1), pp. 429-438.

Hühnerfuss, H., Walter, W., Lange, P. A. & Alpers, W., 1987. Attenuation of wind waves by monomolecular sea slicks and the Marangoni Effect. *Journal of Geophysical Research: Oceans,* 92(C4), pp. 3961-3963.

Isensee, K. & Valdes, L., 2015. *GSDR 2015 Brief: Marine Litter: Microplastics,* New York, NY, USA: IOC / UNESCO.

Ishikawa, R., Tanigaki, T. & Fukuda, Y., 2023. Resolution does matter. *Microscopy,* 72(2), p. 65.

Jambeck, J. et al., 2018. Challenges and Emerging Solutions to the Land-Based Plastic Waste Issue in Africa. *Marine Policy,* Volume 96, pp. 256 - 263.

Jambeck, J. R. et al., 2015. Plastic Waste Inputs from Land into the Ocean.. *Science,* Volume 347, pp. 768 - 771.

Jantz, L. A., Morishige, C. L., Bruland, G. L. & Lepczyk, C. A., 2013. Ingestion of plastic marine debris by longnose lancetfish (Alepisaurus ferox) in the North Pacific Ocean. *Marine Pollution Bulletin,* 69(1 - 2), pp. 97 - 104.

Juan, B. et al., 2014. Protected areas in the Atlantic facing the hazards of micro-plastic pollution: First diagnosis of three islands in the Canary Current. *Marine Pollution Bulletin,* 80 (1 - 2), pp. 302 - 311.

Kaladharan, P. et al., 2020. Marine plastic litter in certain trawl grounds along the peninsular coasts of India. *Marine Pollution Bulletin,* Volume 157, p. 111299.

Kaplan, G. et al., 2021. Normalizing the Local Incidence Angle in Sentinel-1 Imagery to Improve Leaf Area Index, Vegetation Height, and Crop Coefficient Estimations.. *Land,* Volume 10, p. 680.

Kay, S., 1998. *Fundamentals of Statistical Signal Processing: Detection Theory.* Volume 2 ed. London, UK: Pearson.

Keswani, A., Oliver, D. M., Gutierrez, T. & Quilliam, R. S., 2016. Microbial hitchhikers on marine plastic debris: Human exposure risks at bathing waters and beach environments. *Marine Environmental Research,* Volume 118, pp. 10 - 19.

Kikaki, A., Karantzalo, K., Power, C. A. & Raitsos, D. E., 2020. Remote Sensing the Source and Transport of Marine Plastic Debris in Bay Islands of Honduras (Caribbean Sea).. *Remote Sensing,* 12(11), p. 1727.

King, M. D. et al., 2013. Spatial and temporal distribution of clouds observed by MODIS onboard the Terra and Aqua satellites. *IEEE Transactions on Geoscience and Remote Sensing,* 51(7), pp. 3826 - 3852.

Kondolf, G. M. et al., 2014. Sustainable Sediment Management in Reservoirs and Regulated Rivers: Experiences from Five Countries.. *Earth's Future,* Volume 2, pp. 256-280.

Kremezi, M. et al., 2021. Pansharpening PRISMA Data for Marine Plastic. *IEEE Access,* Volume 9, pp. 61955 - 61971.

Kremezi, M. et al., 2022. Increasing the Sentinel-2 potential for marine plastic litter monitoring through image fusion techniques. *Marine Pollution Bulletin,* Volume 182, p. 113974.

Kujawinski, E. B., Farrington, J. W. & Moffett, J. W., 2002. Evidence for Grazing-mediated Production of Dissolved Surface-active Material by Marine Protists. *Marine Chemistry,* 77(2 - 3), pp. 133 - 142.

Kurata, N. et al., 2016. Surfactant-associated Bacteria in the Near-surface Layer of the Ocean. *Scientific Reports,* Volume 6, p. 19123.

Laist, D. W., 1987. Overview of the Biological Effects of Lost and Discarded Plastic Debris in the Marine Environment. *Marine Pollution Bulletin,* 18(6), pp. 319 - 326.

Laist, D. W., 1997. Impacts of Marine Debris: Entanglement of Marine Life in Marine Debris Including a Comprehensive List of Species with Entanglement and Ingestion Records. In: J. Rogers, ed. *Marine Debris: Sources, Impacts and Solutions.* New York, USA: Springer-Verlag, pp. 99 - 139.

Landis, J. R. & Koch, G. G., 1977. The Measurement of Observer Agreement for Categorical Data. *Biometrics,* 33(1), pp. 159 - 174.

Latini, D., Del Frate, F. & Jones, C. E., 2016. Multi-frequency and polarimetric quantitative analysis of the Gulf of Mexico oil spill event comparing different SAR systems. *Remote Sensing of Environment,* Volume 183, pp. 26 - 42.

Law, K. L. et al., 2014. Distribution of surface plastic debris in the Eastern Pacific Ocean from an 11-year data set. *Environ. Sci. Technol,* Volume 48, pp. 4732-4738.

Law, K. L. et al., 2010. Plastic Accumulation in the North Atlantic Subtropical Gyre. *Science,* 329(5996), pp. 1185 - 1188.

Law, K. L. et al., 2010. Plastic Accumulation in the North Atlantic Subtropical Gyre. *Science,* 329(5996), pp. 1185-1188.

Lebreton, L. & Andrady, A., 2019. Future Scenarios of Global Plastic Waste Generation and Disposal. *Palgrave Communications,* Volume 5, p. Article No.6.

Lebreton, L. C. M. et al., 2017. River Plastic Emissions to the World's Oceans.. *Nat. Commun,* Volume 8, p. 15611.

Lebreton, L., Egger, M. & Slat, B., 2019. A global mass budget for positively buoyant macroplastic debris in the ocean. *Scientific Reports,* Volume 9, p. 12922.

Lebreton, L. et al., 2018. Evidence that the Great Pacific Garbage Patch is rapidly accumulating plastics. *Nat. Sci. Rep,* Volume 8, p. 4666.

Lee, J. et al., 2013. Relationships among the abundances of plastic debris in different size classes on beaches in South Korea. *Marine Pollution Bulletin,* 77(1-2), pp. 349 - 354.

Lenz, R., Enders, K., Stedmon, C. A. & Mackenzie, D. M. A., 2015. A Critical Assessment of Visual Identification of Marine Microplastic Using Raman Spectroscopy for Analysis Improvement.. *Marine Pollution Bulletin,* 100(1), pp. 82 - 91.

Li, S., Cummings, M. L. & Welton, B., 2022. Assessing the impact of autonomy and overconfidence in UAV first-person view training. *Applied Ergonomics,* Volume 98, p. 103580.

Li, Z. & Bethel, J., 2008. Image Coregistration in SAR Interferometry. *Int. Arch. Photogramm. Remote Sens. Spat. Inf. Sci. ,* Volume 37, pp. 433-438.

Lobelle, D. & Cunliffe, M., 2011. Early microbial biofilm formation on marine plastic debris. *Marine Pollution Bulletin,* Volume 62, pp. 197-200.

Lozano, R. L. & Mouat, J., 2009. *Marine Litter in the North-East Atlantic Region,* London, United Kingdom: OSPAR Commission: KIMO International: Regional Consultants.

Lozano, R. L. & Mouat, J., 2009. *Marine Litter in the North-East Atlantic Region: Assessment and Priorities for Response,* London, UK: KIMO International.

Lyons, M. M. et al., 2010. Theory of island biogeography on a microscopic scale: organic aggregates as islands for aquatic pathogens. *Aquat Microb Ecol,* Volume 60, pp. 1 - 13.

Lyzenga, D. R., Marmorino, G. O. & Johannessen, J. A., 2004. Ocean Currents and Current Gradients. In: C. A. J. E. Jackson, ed. *Synthetic Aperture Radar Marine Users Manual.* Washington, DC, USA: U.S Department of Commerce National Oceanic and Atmospheric Administration (NOAA), pp. 263 - 276.

Maharjan, N. et al., 2022. Detection of River Plastic Using UAV Sensor Data and Deep Learning. *Remote Sensing,* 14(13), p. 3049.

Mani, T., Hauk, A., Walter, U. & Burkhardt-Holm, P., 2015. Microplastics profile along the Rhine River.. *Sci. Rep,* Volume 5, p. 17988.

Mao, K. et al., 2019. Changes in Global Cloud Cover Based on Remote Sensing Data from 2003 to 2012. *Chinese Geographical Science,* Volume 29, pp. 306 - 315.

Marino, A., 2017. Trace Coherence: A New Operator for Polarimetric and Interferometric SAR Images.. *IEEE Trans. Geosci. Remote Sens.,* Volume 55, pp. 2326-2339.

Marino, A., Dierking, W. & Wesche, C., 2016. A Depolarisation Ratio Anomaly Detector to Identify Icebergs in Sea Ice Using Dual-Polarisation SAR Images.. *IEEE Trans. Geosci. Remote Sens.,* Volume 54, pp. 5602-5615.

Marino, A. & Hajnsek, I., 2013. A Change Detector Based on an Optimisation with Polarimetric SAR Imagery. *IEEE Trans. Geosci. Remote Sens,* Volume 52, pp. 4781-4798.

Marino, A. & Nannini, M., 2022. Signal Models for Changes in Polarimetric SAR Data.. *IEEE Trans. Geosci. Remote Sens.,* Volume 60, pp. 1-18.

Maritime Engineering Reference Book, 2008. *The Maritime Engineering Reference Book: A Guide to Ship Design.* 1st ed. Oxford, UK: Butterworth-Heinemann.

Markic, A., Gaertner, J., Gaertner-Mazoumi, N. & Koelmans, A. A., 2020. Plastic Ingestion by Marine Fish in the Wild. *Critical Reviews in Environmental Science and Technology,* 50(7), pp. 657 - 697.

Martinez-Vicente, V. et al., 2019. Measuring Marine Plastic Debris from Space: Initial Assessment of Observation Requirements. *Remote Sens.,* Volume 11, p. 2443.

Masó , M., Garces, E., Pages, F. & Camp, J., 2003. Drifting plastic debris as a potential vector for dispersing Harmful Algal Bloom (HAB) species. *Scientia Marina,* 67 (1), pp. 107 - 111.

Mason, D. et al., 2012. Near Real-Time Flood Detection in Urban and Rural Areas Using High-Resolution Synthetic Aperture Radar Images. *IEEE Trans. Geosci. Remote Sens.,* Volume 50, pp. 3041 - 3052.

Matthews, J. P. et al., 2017. Dynamics and Early Post-tsunami Evolution of Floating Marine Debris near Fukushima Daiichi. *Nature Geoscience,* Volume 10, pp. 598 - 603.

Mattia, F. et al., 1997. The Effect of Surface Roughness on Multifrequency Polarimetric SAR Data. *IEEE Transactions on Geoscience and Remote Sensing,* 35(4), pp. 954 - 966.

Mattia, F. et al., 1997. The Effect of Surface Roughness of Multifrequency Polarimetric SAR Data. *IEEE Trans. Geosci. Remote Sens.,* Volume 35, pp. 954-966.

Mauriello, G. et al., 2005. Antimicrobial Activity of a Nisin-activated Plastic Film for Food Packaging. *Letters in Applied Microbiology,* 41(6), pp. 464-469.

Maximenko, N. et al., 2019. Toward the Integrated Marine Debris Observing Platform.. *Front. Mar. Sci,* Volume 6, p. 447.

Meyer, F., 2019. Spaceborne Synthetic Aperture Radar: Principles, Data Access, and Basic Processing Techniques. In: *The SAR Handbook.* s.l.:NASA, pp. 21 - 44.

Miglioranza, K. S. B., de Moreno, J. E. A. & Moreno, V. J., 2004. Land-based Sources of Marine Pollution: Organochlorine Pesticides in Stream Systems. *Environmental Science and Pollution Research,* Volume 11, pp. 227 - 232.

Mitidieri, F., Papa, M. N., Amitrano, D. & Ruello, G., 2016. River Morphology Monitoring Using Multitemporal SAR Data: Preliminary Results.. *Eur. J. Remote Sens. ,* Volume 49, pp. 889-898.

Molkov, A. A., Federov, S. V., Pelevin, V. V. & Korchemkina, E. N., 2019. Regional Models for High-Resolution Retrieval of Chlorophyll a and TSM Concentrations in the Gorky Reservoir by Sentinel-2 Imagery. *Remote Sens,* Volume 11, p. 1215.

Mondal, S. & Lee, M.-A., 2022. Long-Term Observations of Sea Surface Temperature Variability in the Gulf of Mannar. *Journal of Marine Science and Engineering,* 11(1), p. 102.

Moore, C. J., 2008. Synthetic Polymers in the Marine Environment: A Rapidly Increasing, Long-term Threat. *Environmental Research,* 108 (2), pp. 131 - 139.

Moore, C., Lattin, G. & Zellers, A., 2011. Quantity and Type of Plastic Debris Flowing from Two Urban Rivers to Coastal Waters and Beaches of Southern California.. *J. Integr. Coast. Zone. Manag.,* Volume 11, pp. 65-73.

Moshtagi, M. et al., 2021. Spectral Reflectance of Marine Macroplastics in the VNIR and SWIR Measured in a Controlled Environment.. *Scientific Reports,* Volume 11, p. 5436.

Naidoo, T., Smit, A. J. & Glassom, D., 2015. Plastic Ingestion by Estuarine Mullet Mugil cephalus (Mugilidae) in Urban Harbour, KwaZulu-Natal, South Africa. *African Journal of Marine Sciences,* 38(1), pp. 145 - 149.

Naz, S., Iqbal, M. F., Mahmood, I. & Allam, M., 2020. Marine oil spill detection using Synthetic Aperture Radar over Indian Ocean.. *Mar. Pollut. Bull.,* Volume 162, p. 111921.

Neves, D., Sobral, P. & Pereira, T., 2015. Marine litter in bottom trawls off the Portuguese coast. *Marine Pollution Bulletin,* 99 (1 - 2), pp. 301 - 304.

Neves, D., Sobral, P. & Pereira, T., 2015. Marine Litter in Bottom Trawls off the Portuguese Coast. *Marine Pollution Bulletin,* 99(1-2), pp. 301 - 304.

Nirchio, F. et al., 2005. Automatic detection of oil spills from SAR images. *International Journal of Remote Sensing,* 26(6), pp. 1157 - 1174.

Norris, J. R., 1999. On Trends and Possible Artifacts in Global Ocean Cloud Cover between 1952 and 1995. *Journal of Climate,* 12(6), pp. 1864 - 1870.

Novak, L. M., Sechtin, M. B. & Cardullo, M. J., 1989. Studies of Target Detection Algorithms that use Polarimetric Radar Data.. *IEEE Trans. Aerosp. Electron. Syst.,* Volume 25, pp. 150-165.

Osborn, M. A. & Stojkovic, S., 2014. Marine microbes in the Plastic Age. *Microbiology Australia,* 35(4), pp. 207-210.

OSPAR, 2007. *OSPAR Pilot Project on Monitoring Marine Beach Litter,* London, UK: OSPAR Commission.

Pabortsava, K. & Lampitt, R. S., 2020. High Concentrations of Plastic Hidden Beneath the Surface of the Atlantic Ocean.. *Nature Communications,* Volume 11, pp. 1065 - 1074.

Palombi, L. & Raimondi, V., 2022. Experimental Tests for Fluorescence LIDAR Remote Sensing of Submerged Plastic Marine Litter. *Remote Sensing,* 14(23), p. 5914.

Papakonstantinou, A., Batsaris, M., Spondylidis, S. & Topouzelis, K., 2021. A Citizen Science Unmanned Aerial System Data Acquisition Protocol and Deep Learning Techniques for the Automatic Detection and Mapping of Marine Litter Concentrations in the Coastal Zone. *Drones,* 5(1), p. 6.

Pardhi, D. S. et al., 2022. Microbial surfactants: A journey from fundamentals to recent advances. *Frontiers in Microbiology,* Volume 13.

Pereira, R., Schneider-Zapp, K. & Upstill-Goddard, R. C., 2016. Surfactant Control of Gas Transfer Velocity Along an Offshore Coastal Transect: Results from a Laboratory Gas Exchange Tank. *Biogeoscience,* Volume 13, pp. 3981 - 3989.

Phillips, O. M., 1988. Radar Returns from the Sea Surface—Bragg Scattering and Breaking Waves. *Journal of Physical Oceanography,* 18(8), pp. 1065-1074.

Phillips, O. M., 1988. Radar Returns from the Sea Surface–Bragg Scattering and Breaking Waves.. *J. Phys. Oceanogr.* , Volume 18, pp. 1065 - 1074.

Prudente, V. H. R. et al., 2020. Limitations of cloud cover for optical remote sensing of agricultural areas across South America. *Remote Sensing Applications: Society and Environment,* Volume 20, p. 100414.

Qian, P. Y. et al., 2007. Marine Biofilms as Mediators of Colonization by Marine Macroorganisms: Implications for Antifouling and Aquaculture. *Marine Biotechnology,* Volume 9, pp. 399-410.

Qian, X. et al., 2024. Rapid single-particle chemical imaging of nanoplastics by SRS microscopy. *Proc. Nat. Acad. Sci.*, 121(3), p. e2300582121.

Qi, L., Wang, N., Hu, C. & Holt, B., 2022. On the Capacity of Sentienl-1 Synthetic Aperture Radar in Detecting Floating Macroalgae and Other Floating Matters.. *Remote Sens. Environ.,* Volume 280, p. 113188.

Rani, M., Masroor, M. & Kumar, P., 2021. *1 - Remote Sensing of Ocean and Coastal Environment - Overview.* s.l.:Elsevier.

Rao, T. S., 2010. Comparative effect of temperature on biofilm formation in natural and modified marine environment. *Aquatic Ecology,* Volume 44, pp. 463 - 478.

Reyes-Carmona, C. et al., 2020. Sentinel-1 DInSAR for Monitoring Active Landslides in Critical Infrastructures: The Case of the Rules Reservoir (Southern Spain).. *Remote Sens,* Volume 12, p. 809.

Ribic, C. A., Sheavly, S. B., Rugg, D. J. & Erdmann, E. S., 2010. Trends and drivers of marine debris on the Atlantic coast of the United States 1997–2007. *Marine Pollution Bulletin,* 60(8), pp. 1231 - 1242.

Richards, J. A., 2009. *Remote Sensing with Imaging Radar.* Vol. 1. ed. s.l.:Springer.

Rochman, C. M., Kurobe, T., Flores, I. & Teh, S. J., 2014. Early Warning Signs of Endocrine Disruption in Adult Fish from the Ingestion of Polyethylene with and without Sorbed Chemical Pollutants from the Marine Environment.. *Science of the Total Environment,* Volume 493, pp. 656 - 661.

Rochman, C. M. et al., 2015. Anthropogenic debris in seafood: Plastic debris and fibers from textiles in fish and bivalves sold for human consumption. *Scientific Reports,* Volume 5, p. 14340.

Ruwaimana, M. et al., 2018. The advantages of using drones over space-borne imagery in the mapping of mangrove forests. *PLoS ONE,* 13(7), p. e0200288.

Ryan, P. G., Moore, C. J., Van Franeker, J. A. & Moloney, C. L., 2009. Monitoring the abundance of plastic debris in the marine environment.. *Philos. Trans. R. Soc. B. Biol. Sci.,* Volume 364, pp. 1999-2012.

Sabbaghzadeh, B. et al., 2017. The Atlantic Ocean Surface Microlayer from 50°N to 50°S is Ubiquiotously Enriched in Surfactants at Wind Speeds up to 13 ms-1. *Geophysical Research Letters,* 44(6), pp. 2852 - 2858.

Salgado-Hernanz, P. M. et al., 2021. Assessment of Marine Litter Through Remote Sensing: Recent Approaches and Future Goals.. *Mar. Pollut. Bull.,* Volume 168, p. 112347.

Savastano, S., Cester, I., Perpinya, M. & Romero, L., 2021. *A First Approach to the Automatic Detection of Marine Litter in SAR Images Using Artificial Intelligence.* Brussels, Belgium, IEEE International Geoscience and Remote Sensing Symposium IGARSS.

Schmidt, C., Krauth, T. & Wagner, S., 2017. Export of Plastic Debris by Rivers into the Sea. *Environmental Science and Technology,* 51(21), pp. 12246 - 12253.

Schrey, E. & Vauk, G. J. M., 1987. Records of Entangled Gannets (Sula bassana) at Helgoland, German Bight.. *Front. Environ. Sci,* Volume 18, pp. 350 - 352.

Selvam, K. et al., 2021. Abundance, Composition and Sources of Marine Debris Trawled-up in the Fishing Grounds Along the North-east Arabian Coast. *Science of the Total Environment,* Volume 751, p. 141771.

Serafino, F. & Bianco, A., 2021. Use of X-Band Radars to Monitor Small Garbage Islands.. *Remote Sens.,* Volume 13, p. 3558.

Shi, J. et al., 1997. Estimation of Bare Surface Soil Moisture and Surface Roughness Parameter Using L-Band SAR Image Data. *IEEE Transactions on Geoscience and Remote Sensing,* 35 (5), pp. 1254 - 1266.

Simpson, M. D. et al., 2022. Monitoring of Plastic Islands in River Environment Using Sentinel-1 SAR Data. *Remote Sensing,* 14(18), p. 4473.

Simpson, M. D. et al., 2022. Monitoring of Plastic Islands in River Envi-ronment Using Sentinel-1 SAR Data.. *Remote Sens.,* Volume 14, p. 4473.

Simpson, M. D. et al., 2023. Investigating the Backscatter of Marine Plastic Litter Using a C- and X-Band Ground Radar, during a Measurement Campaign in Deltares. *Remote Sensing,* 15(6), p. 1654.

Simpson, M. et al., 2021. *Monitoring Surfactants Pollution Potentially Related to Plastics in the World Gyres Using Radar Remote Sensing.* Brussels, Belgium, IEEE.

Simpson, M. et al., 2021. *Monitoring Surfactants Pollution Potentially Related to Plastics in the World Gyres Using Radar Remote Sensing.* Brussels, s.n.

Siraj, I. & Bharti, P. S., 2020. Process Capability Analysis of a 3D Printing Process. *Journal of Interdisciplinary Mathematics,* 32(1), pp. 175 - 189.

Smith, M., Love, D. C., Rochman, C. M. & Neff, R. A., 2018. Microplastics in Seafood and the Implications for Human Health. *Curr. Environ. Health Rep.,* Volume 5, pp. 375-386.

Smith, M., Love, D. C., Rochman, C. M. & Neff, R. A., 2018. Microplastics in Seafood and the Implications for Human Health. *Current Environmental Health Reports,* Volume 5, pp. 375 - 386.

Spizzichino, V., Caneve, L., Colao, F. & Ruggiero, L., 2016. Characterization and Discrimination of Plastic Materials Using Laser-Induced Fluorescence. *Applied Spectroscopy,* 70(6), pp. 1001 - 1008.

Stenger, K. S., Wikmark, O. G., Bezuidenhout, C. C. & Molale-Tom, L. G., 2021. Microplastics pollution in the ocean: Potential carrier of resistant bacteria and resistance genes. *Environ. Pollut.,* Volume 291, p. 118130.

Stilla, D. et al., 2020. Desert Roughness Retrieval Using CYGNSS GNSS-R Data. *Remote Sensing,* 12(4), p. 743.

Sun, Y., Bakker, T., Ruf, C. & Pan, Y., 2023. Effects of microplastics and surfactants on surface roughness of water waves. *Scientific Reports,* Volume 13, p. 1978.

Sun, Y., Bakker, T., Ruf, C. & Pan, Y., 2023. Effects of microplastics and surfactants on surface roughness of water waves. *Scientific Reports,* Volume 13, p. 1978.

Taddia, Y. et al., 2021. UAV Approach for Detecting Plastic Marine Debris on the Beach: A Case Study in the Po River Delta (Italy). *Drones,* 5(4), p. 140.

Topouzelis, K. N., 2008. Oil Spill Detection by SAR Images: Dark Formation Detection, Feature Extraction and Classification Algorithms. *Sensors,* 8(10), pp. 6642 - 6659.

Topouzelis, K. et al., 2020. Remote Sensing of Sea Surface Artificial Floating Plastic Targets with Sentinel-2 and Unmanned Aerial Systems (Plastic Litter Project 2019).. *Remote Sens,* Volume 12, p. 2013.

Topouzelis, K., Papageorgiou, D., Suaria, G. & Aliani, S., 2021. Floating marine litter detection algorithms and techniques using optical remote sensing data: A review. *Marine Pollution Bulletin,* Volume 170, p. 112675.

Topouzelis, K., Papakonstantinou, A. & Garaba, S. P., 2019. Detection of Floating Plastics from Satellite and Unmanned Aerial Systems (Plastic Litter Project 2018). *Int. J. Appl. Earth Obs. Geoinf.,* Volume 79, pp. 175-183.

Toth, C. & Jozkow, G., 2016. Remote Sensing Platforms and Sensors: A Survey.. *ISPRS J. Photogramm. Remote Sens.,* Volume 115, pp. 22-36.

Van der Wal, D., Herman, P. M. J. & Dool, A. W., 2005. Characterisation of Surface Roughness and Sediment Texture of Intertidal Flats Using ERS SAR Imagery. *Remote Sensing of Environment,* 98(1), pp. 96 - 109.

Van der Wal, D., Herman, P. M. J. & Dool, A. W., 2005. Characterisation of Surface Roughness and Sediment Texture of Intertidal Flats Using ERS SAR Imagery.. *Remote Sens. Environ. ,* Volume 98, pp. 96-109.

Van der Wal, M. et al., 2015. *Identification and Assessment of Riverine Input of (Marine) Litter; Final Report for European Commission DG Environment under Framework Contract No. ENV.D.2/FRA/2012/0025,* Bristol, UK: Eunomia Research & Consulting Ltd.

van Franeker, J. A. et al., 2011. Monitoring Plastic Ingestion by the Northern Fulmar Fulmaris glacialis in the North Sea.. *Environmental Pollution,* 159 (10), pp. 2609 - 2615.

Van Sebille, E. et al., 2015. A global inventory of small floating plas-tic debris.. *Environ. Res. Lett,* Volume 10, p. 124006.

van Zyl, J. & Kim, Y., 2010. Synthetic Aperture Radars (SAR) Imaging Basics. In: J. Yuen, ed. *Synthetic Aperture Radar Polarimetry.* New York: John Wiley and Sons.

Veenstra, T. S. & Churnside, J. H., 2012. Airborne sensors for detecting large marine debris at sea. *Marine Pollution Bulletin,* 65(1 - 3), pp. 63 - 68.

Veettil, B. K. et al., 2022. Coastal and marine plastic litter monitoring using remote sensing: A review. *Estuarine, Coastal and Shelf Science,* Volume 279, p. 108160.

Vermeiren, L. et al., 1999. Developments in the Active Packaging of Foods. *Trends in Food Science and Technology ,* 10(3), pp. 77 - 86.

Vickers, H., Malnes, E. & Hogda, K., 2019. Long-Term Water Surface Area Monitoring and Derived Water Level Using Synthetic Aperture Radar (SAR) at Altevatn, a Medium-Sized Arctic Lake.. *Remote Sens.,* Volume 11, p. 2780.

Waluda, C. M. & Staniland, I. J., 2013. Entanglement of Antarctic Fur Seals at Bird Island, South Georgia. *Marine Pollution Bulletin,* Volume 74, pp. 244 - 252.

Wang, B. H. et al., 2019. An overview of various kinds of wind effects on unmanned aerial vehicle. *Measurement and Control,* 52 (7 - 8), pp. 731 - 739.

Waqas, M. et al., 2023. Marine plastic pollution detection and identification by using remote sensing-meta analysis. *Marine Pollution Bulletin,* Volume 197, p. 115746.

Watkins, L., McGrattan, S., Sullivan, P. & Walter, M. T., 2019. The Effect of Dams on River Transport of Microplastic Pollution.. *Sci. Total Environ.,* Volume 664, pp. 834-840.

Watts, A. J. R. et al., 2015. Ingestion of Plastic Microfibers by the Crab Carcinus maenas and its Effect on Food Consumption and Energy Balance.. *Environ. Sci. Technol,* 49(24), pp. 14597 - 14604.

Webb, H. K., Crawford, R. J., Sawabe, T. & Ivanova, E. P., 2009. Poly(ethylene terephthalate) polymer surfaces as a substrate for bacterial attachment and biofilm formation. *Microbes and Environments,* 24(1), pp. 39-42.

Wilcox, C., Hardesty, B. D. & Law, K. L., 2020. Abundance of Floating Plastic Particles Is Increasing in the Western North Atlantic Ocean. *Environ. Sci. Technol.,* 54(2), pp. 790 - 796.

Wilcox, C., Van Sebille, E. & Hardesty, B. D., 2015. Threat of Plastic Pollutant to Seabirds is Global, Pervasive and Increasing. *Proceedings of the National Academy of Sciences,* 112(38), pp. 11899 - 11904.

Worm, B. et al., 2017. Plastic as a Persistent Marine Pollutant. *Annual Review of Environment and Resources,* Volume 42, pp. 1 - 26.

Wright, R. J. et al., 2020. Marine Plastic Debris: A New Surface for Microbial Colonization. *Environ. Sci. Technol,* 54(19), pp. 11657 - 11672.

Wurl, O. et al., 2011. Formation and Global Distribution of Sea-surface Microlayers. *Biogeosciences,* Volume 8, pp. 121 - 135.

Yamaguchi, Y., Mariyama, T., Ishido, M. & Yamada, H., 2005. Four-component scattering model for polarimetric SAR image decomposition. *IEEE Transactions on Geoscience and Remote Sensing,* 43(8), pp. 1699 - 1706.

Yan, Q., Huang, W. & Foti, G., 2017. Quantification of the Relationship Between Sea Surface Roughness and the Size of the Glistening Zone for GNSS-R.. *IEEE Geoscience and Remote Sensing Letters,* 15(2), pp. 237 - 241.

Yonkos, L. et al., 2014. Microplastics in Four Estuarine Rivers in Chesapeake Bay, USA.. *Environ. Sci. Technol.,* Volume 48, pp. 14195-14202.

Yusuf, A. A. et al., 2022. Effects of hybrid nanoparticle additives in n-butanol/waste plastic oil/diesel blends on combustion, particulate and gaseous emissions from diesel engine evaluated with entropy-weighted PROMETHEE II and TOPSIS: Environmental and health risks of plastic wa. *Energy Convers. Manag. ,* Volume 264, p. 115758.

Zeri, C. et al., 2018. Floating plastics in Adriatic waters (Mediterranean Sea): From the macro- to the micro-scale. *Marine Pollution Bulletin,* Volume 136, pp. 341 - 350.

Zettler, E. R., Mincer, T. J. & Amaral-Zettler, L. A., 2013. Life in the “Plastisphere”: Microbial Communities on Plastic Marine Debris. *Environmental Science and Technology*, 47(13), pp. 7137-7146.

Zhao, S., Zettler, E. R., Amaral-Zettler, L. A. & Mincer, T. J., 2021. Microbial carrying capacity and carbon biomass of plastic marine debris. *The ISME Journal* , Volume 15, pp. 67 - 77.

Zutic, V. et al., 1981. Surfactant Production by Marine Phytoplankton. *Marine Chemistry*, 10(6), pp. 505 - 520.

Appendices

Appendix A

Table A1. Plastics used during the Deltares Test campaigns. Items were classified using the Lebreton et al, (2018) identification of items. When the plastic type is marked with an *, this means the polymer could not be verified.

ID	Plastic	Class	Type (Lebreton et al., 2018)	Plastic Type	Shape	Size (mm)	A_front (cm^2)	Weight (g)
1	Bottles	Hard Plastics	H	PET	Cylinder	155 × 55 (L × D)	85.3	20
2	Fixed Nets	Nets	N	NYLON (PA)	Array of Ropes	Width of Wires 1.5; Mesh Size 15; Net Size 4 × 5 m	2000	135
3	Bottles + Fixed Nets	Hard Plastics	H	PET	Cylinder	220 × 60 (L × D)	132	25
4	Straws	Hard Plastics	H	PP*	Cylinder	240 x 13 (LxD)	31.2	2
5	Food Wraps and Bags (Marine Litter)	Sheets	H	LDPE	Rectangular	200 × 200	400	4
6	Nets (Marine Litter)	Ropes	N	Other	Array of Ropes	Width of ropes: 5; L: 200	10	10
7	Nets + Bottles (Marine Litter)	Ropes	N	Other	Array of Ropes, Wrapped around a Bottle	155 × 70 (L × D)	108.5	35
8	Bottles without Caps/Filled with Water	Hard Plastics	H	PET	Cylinder	155 × 55 (L × D)	85.3	20
9	Pellets	Pellets	P	PP/PE	Sphere	4	0.1	0
10	Styrofoam	Foam	F	PS	Rectangular	300 × 300	900	40
11	Caps and Lids (Mix of Marine Litter and Clean)	Hard Plastics	H	PP	Cylinder with Cap	11 × 40 (L × D)	12.6	2.4
12	Cigarette Filters (Marine Litter)	Hard Plastics	H	PET	Cylinder-like	30 × 8 (L × D)	2.4	2
13	Cutlery	Hard Plastics	H	PP	Blade-like	180 × 12 (L × W)	21.6	6
14	Plastic Spheres	Hard Plastics	H	PP	Sphere	20	3.1	3.5

15	EVA Cylindrical Foam	Foam	F	EVA	Cylinder	D: 30; Wa: 8; L 200	60	2.5
16	EVA Cylindrical Foam	Foam	F	EVA	Cylinder	D: 30; Wa: 8; L 100	30	1.3
17	EVA Cylindrical Foam	Foam	F	EVA	Cylinder	D: 30; Wa: 8; L 50	15	0.6
18	Transparent Plastic Lids	Hard Plastics	H	PP	Sheet	190 × 138	262.2	7.1
19	Straws	Hard Plastics	H	PP *	Cylinder	120 × 13	15.6	1
20	Straws	Hard Plastics	H	PP *	Cylinder	60 × 13	7.8	0.5
21	Transparent Plastic Lids Without Edges	Hard Plastics	H	PP	Cylinder	160 × 110	176	4.3